Evaluation and application of Finite Element Sea Ice-Ocean Model (FESOM) for the Arctic–North Atlantic region in variable resolution global simulations

Von der Fakultät für Physik und Elektrotechnik
der Universität Bremen
zur Erlangung des akademischen Grades
einer **Doktorin der Naturwissenschaften (Dr. rer. nat.)**
genehmigte Dissertation

von

Xuezhu Wang

Gutachter: Prof. Dr. Thomas Jung
Zweitgutachter: Prof. Dr. Torsten Kanzow
Eingereicht am: 25.02.2016

Declaration of Authorship

I certify that the work presented here is, to the best of my knowledge and belief, original and the result of my own investigations, except as acknowledged, and has not been submitted, either in part or whole, for a degree at this or any other University.

Bremerhaven, Feb 2016

Abstract

The changes and variability of the Arctic – North Atlantic Oceans and the inter-exchange of water mass and heat is of crucial relevance for the global ocean and climate. In this work the Finite Element Sea-ice Ocean Model (FESOM) is used to simulate the global ocean with focus on the Arctic – North Atlantic region. FESOM is formulated on unstructured meshes and offers variable-resolution functionality which is difficult to achieve in traditional structured-mesh models. With this powerful tool we are able to resolve the key areas with locally refined resolutions in global simulations.

The performance of FESOM in the Arctic Ocean and North Atlantic on large time scales is first evaluated in a 240-yr hindcast experiment. The model can reproduce realistic Atlantic Meridional Overturning Circulation (AMOC) and realistic Arctic freshwater content variability and sea ice extent. A water-hosing experiment is conducted to study the model sensitivity to increased freshwater input from Greenland Ice Sheet (GrIS) melting in a 0.1 Sv discharge rate scenario. The released freshwater from Greenland can penetrate into the Arctic Ocean, especially in the Eurasian Basin. The anomalous freshwater also leads to a reduction in the AMOC strength and changes in freshwater exchange between the two oceans.

Simulations with different local resolutions of 24 km and 9 km in the Arctic Ocean and surrounding regions are carried out to study the influence of resolution on the simulated Arctic Ocean and Arctic-Subarctic fluxes. Both simulations can reasonablly simulate the mean state and variability of sea ice condition, freshwater content in the Arctic Ocean, and the fluxes through the Arctic gateways when compared to observations and previous model studies. Although the high resolution (9 km) run tends to improve the representation

of fluxes through the Arctic gateways and the salinity structure in the Arctic basin, higher meso-scale eddy resolving resolution is required to further improve the simulation.

The driving mechanism of the interannual variability of Barents Sea sea ice is studied. We found that sea ice import into the Barents Sea drives the sea ice interannual variability. The amount of sea ice flux determines the thermodynamic growth rate in the Barents Sea. The increasing trend of Atlantic Water heat flux through the Barents Sea Opening leads to the decline of Barents Sea ice volume.

Contents

1 Introduction **1**

2 Model description and atmospherical forcing **7**
2.1 The Finite-Element Sea-Ice Ocean Model (FESOM) 7
2.1.1 Governing equations for the ocean component 8
2.1.2 Governing equations for the sea ice component 10
2.1.3 Discretization of FESOM 13
2.2 Atmospheric Forcing 15

3 Long-term ocean simulations in FESOM **17**
3.1 Introduction 17
3.2 Model setup 20
3.3 Simulated state in the control run 22
3.3.1 The North Atlantic 22
3.3.2 The Arctic Ocean 25
3.4 The GrIS melting scenario 27
3.4.1 Global dynamical sea level change 27
3.4.2 Freshwater distribution and ocean salinity change . . . 31
3.4.3 The influence on the Arctic Ocean 33
3.4.4 The impact on AMOC 37
3.5 Discussion and conclusions 39

4 Influence of resolution on Arctic-North Atlantic simulation **45**
4.1 Introduction 45
4.2 Model setup 48

4.3 Results 49
4.3.1 Sea ice extent 50
4.3.2 Freshwater budget 55
4.3.3 Fluxes through Arctic gateways 60
4.3.4 Atlantic Water inflow 62
4.4 Summary 72

5 Sea ice interannual variability in Barents Sea 75
5.1 Introduction 75
5.1.1 Sea ice variability in the Barents Sea 76
5.2 Model setups 81
5.3 Simulated variability 81
5.4 What drives the interannual variability 85
5.5 Conclusion 89

6 Summary and Outlook 91

A Supplementary 95

B Abbreviations 101

Bibliography 122

Acknowledgment 124

Chapter 1

Introduction

Ocean General Circulation Models (OGCMs) have been developed into a useful tool since last decades for the description of dynamical and thermodynamical processes in the oceans, the interpretation of oceanographic data, testing theoretical hypothesis of oceanic physical processes and providing guidance for new observational programs. Numerical ocean models provide the capability to overcome the spatial and temporal limitations of observational data and to simulate the general ocean circulation based on a set of simplied equations and parametrizations to substitute processes that can not be resolved by the model discretisation. With computational development and practical experience accumulated over model histories, a wide range of ocean models have reached a high level of sophistication and offer users a wide selection of algorithms and parameterizations to generate ocean simulations by implementing actual geometry, bathmetry and realistic boundary fluxes and forcing. Many scientific questions related to ocean and climate dynamics can be explored with these powerful and advanced tools.

Most of OGCMs widely used today are formulated on regular, structured meshes. With progress in computational science, the ocean modelling community has been increasing the ability to simulate the ocean at high resolution. However, global high resolution ocean modelling on a conventional regular Finite-Difference discretisation need to overcome challenges either due to high computational costs or applying complicated traditional grid

nesting methods. In recent years a new generation of ocean models that employ unstructured-mesh methods has emerged. There are certain advantages in favour of models capable to work on unstructured meshes in a global configuration: First, it allows the use of high spatial resolution in dynamically active regions, such as the equatorial belt, the western boundaries, while keeping a relatively coarse resolution otherwise; second, it can resolve the narrow straits in the ocean where the local dynamics play an important role; third, it can help to create setups with the resolution varying in proportion to the ocean Rossby radius.

The Finite Element Sea Ice-Ocean Model(FESOM) developed at Alfred Wegener Institute for Polar and Marine Research(AWI) is the first global ocean general circulation model with such functionality above-mentioned, based on unstructured-mesh methods, that has been developed for the purpose of climate research (*Danilov et al.*, 2004, 2005; *Wang et al.*, 2008, 2014; *Timmermann et al.*, 2009; *Sidorenko et al.*, 2015).

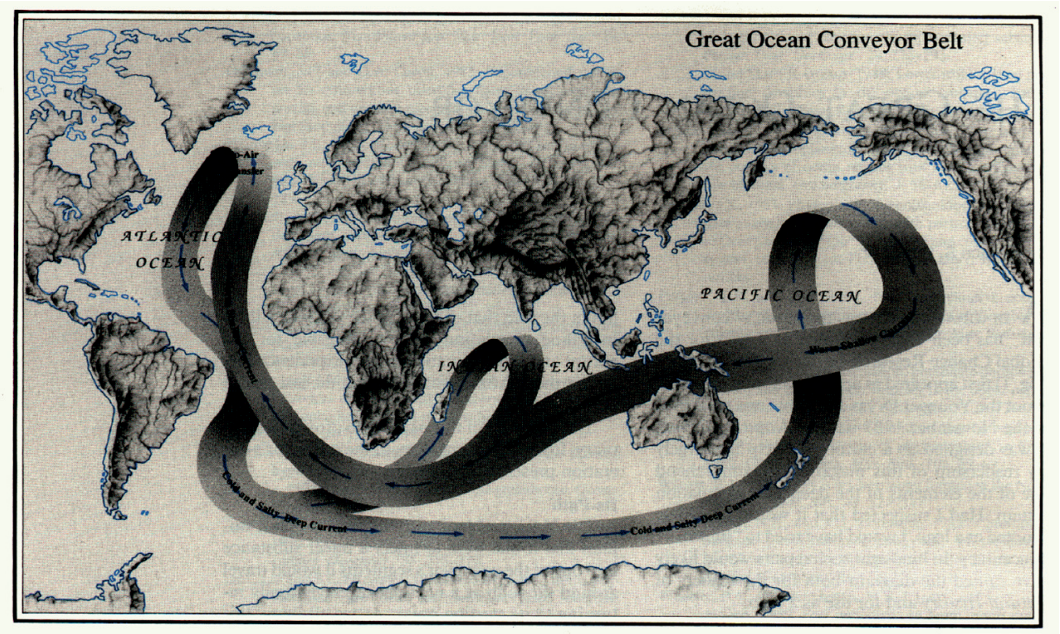

Figure 1.1: The great ocean conveyor logo (*Broecker*, 1987). (Illustration by Joe Le Monnier, Natural History Magazine.)

The world ocean is an essential regulator of climate through its ability to

transport a large amount of heat, freshwater(FW) and nutrients (*Macdonald et al.*, 1996; *Houghton et al.*, 1996). The pathways and exchanges of this transport are critical issues in understanding the present state of climate and the possibilities of future changes. Oceanic surface waters are heated in low latitudes and transported by ocean currents towards the higher latitudes. At certain deep water formation sites in high latitudes, the surface waters lose their buoyancy due to intensified cooling and ventilate downward by deep water formation. These dense and cold water masses are then advected by deep ocean currents towards lower latitudes which closes the loop of great ocean conveyor belt (*Broecker et al.*, 1991; *Kuhlbrodt et al.*, 2007)–Meridional Overturning Circulation(MOC). As shown in Figure 1.1, the great ocean conveyor belt connects the basin wide large-scale oceanic circulation of the Atlantic, Indian, Pacific and Southern Oceans to each other.

The deep water formation sites in the Northern Hemisphere are only located in the North Atlantic Ocean. Exchanges between the North Atlantic and the Arctic Ocean result in the most dramatic water mass conservations and play an important role in the ocean conveyor belt. The Arctic Ocean, as a large FW reservoir, shown in Figure 1.2, exports FW to the subpolar North Atlantic via Fram Strait and Canadian Arctic Archipelago (CAA), which can influence the upper subpolar ocean stratification, further impacting the intensity of deep water formation in Greenland, Iceland and labrador Seas and the strength of Atlantic Meridional Overturning Circulation (AMOC) (*Aagaard et al.*, 1985; *Goosse et al.*, 1997; *Häkkinen*, 1999; *Wadley and Bigg*, 2002; *Jungclaus et al.*, 2005). Meanwhile, the Atlantic Water(AW) supplies the main inflow of volume, salt and heat to the Arctic Ocean. After passing the Norwegian Sea, the warm AW follows its way toward the Arctic through two passages: one branch enters the Arctic Ocean through the deep Fram Strait, and the other branch crosses the broad shelf of the Barents Sea and passes through the Barents Sea, then continues into the Arctic Ocean via the St. Anna Trough, as shown in Figure 1.2. The warming of AW layer in the Arctic Ocean could contribute to drastic reduction of the Arctic sea ice in the future (*Polyakov et al.*, 2010; *Lique*, 2015).

In addition, the Arctic Ocean itself is also an important component of

the climate system because of the expectation of an amplified climate signal in the Arctic due to the ice-albedo and snow-albedo feedback effects, which have impacts on the air-sea heat, momentum, mass and gas exchange and even the large scale Earth System (*Hansen et al.*, 1997).

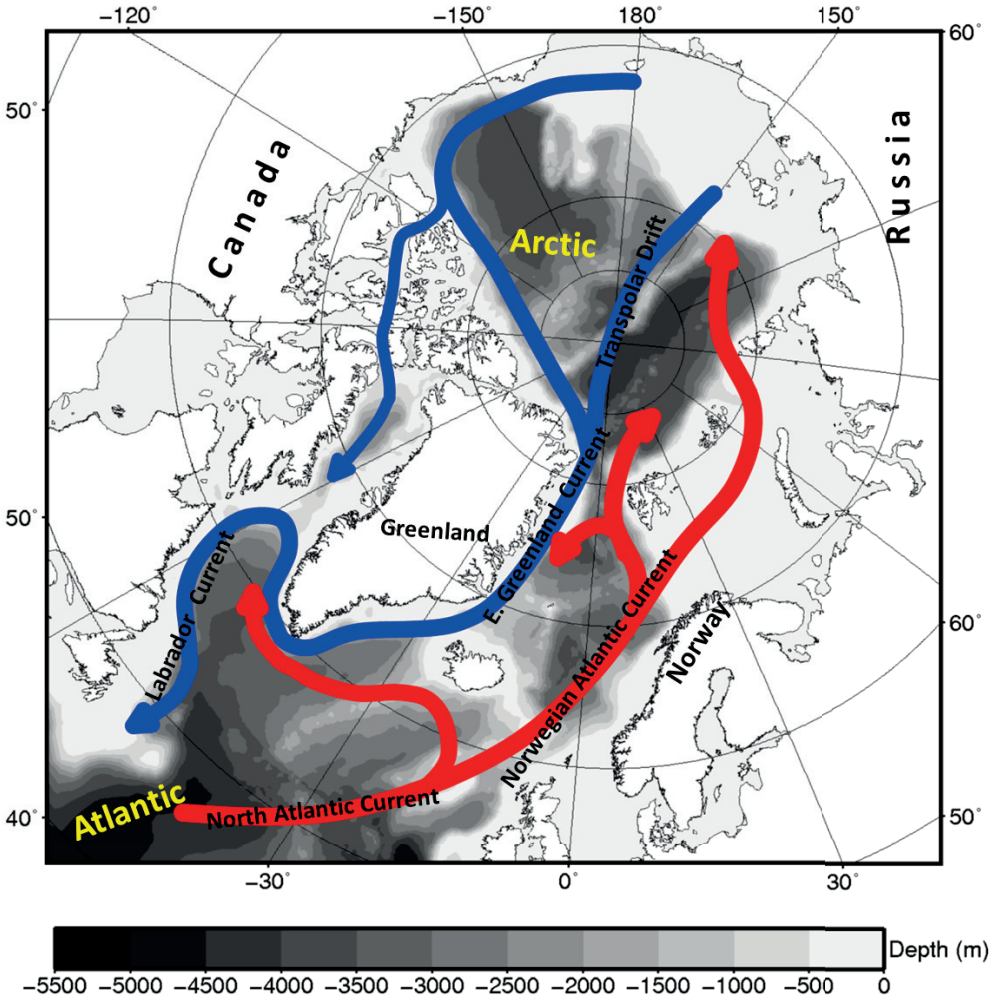

Figure 1.2: The circulation scheme between the North Atlantic and the Arctic Ocean. Red indicates the warm inflow of the Atlantic Water and blue indicates the cold outflow water from the Arctic Ocean.

In spite of the importance of the Arctic-North Atlantic region in the climate system, their representation in ocean climate models still has large uncertainties (*Danabasoglu et al.*, 2014, 2016; *Wang et al.*, 2016a,b). FESOM

is a new generation ocean model, with numerics very different from traditional models, so we will assess it with respect to its simulated Arctic-North Atlantic region in this work. Locally high resolution will be used to study the sensitivity of the model to diffrent horizontal resolutions. This thesis is aimed at the implementation of FESOM with focus on the simulations of the Arctic-North Atlantic region to address the following questions: What's the long-term behaviour of FESOM in simulating the ocean and ice variability? What's the influence of local resolution on the Arctic Ocean simulations? What's the variability of sea ice in the Barents Sea and the dominant mechanism for sea ice interannual variability in the Barents Sea?

Content of the thesis The thesis has 3 main chapters (3 – 5), besides the general introduction (chapter 1), methodology (chapters 2), and summary and outlook (chapter 6) chapters.

Chapter 2: Chapter 2 introduces the governing equations of the ocean and sea ice components in FESOM and the basic information of the model discretization. The atmospheric forcing used in this study is also briefly introduced in this chapter.

Chapter 3: Chapter 3 evaluates the long-term performance of FESOM in a 240-yr hindcast experiment with CORE interannual atmospheric forcing. The focus is on the AMOC and the Arctic Ocean. A case study with described 0.1Sv anomalous freshwater input into the ocean from Greenland Ice Sheet (GrIS) melting is conducted to study the direct ocean response.

Chapter 4: The Arctic Ocean simulated in two FESOM setups with different resolutions (24km and 9km) is discussed in chapter 4, with comparison to available observations and other model simulations in the Coordinated Ocean-Ice Reference Experiment (CORE)-II project. The focus is mainly on the influence of resolution on simulated sea ice and freshwater in the Arctic Ocean, fluxes through the Arctic gateways, and the Atlantic Water inflow in Fram Strait and Barents Sea Opening.

Chapter 5: Chapter 5 assesses the simulated Barents Sea sea ice variability in the 9km resolution run. Sensitivity experiments are carried out to reveal the mechanism determining the sea ice interannual variability in the Barents Sea.

Chapter 2

Model description and atmospherical forcing

2.1 The Finite-Element Sea-Ice Ocean Model (FESOM)

The Finite-Element Sea-Ice Ocean Model (FESOM), developed at Alfred Wegener Institute, Helmholtz Centre for Polar and Marine Research (AWI) is applied in this work (*Danilov et al.*, 2004, 2005; *Wang et al.*, 2008; *Timmermann et al.*, 2009; *Wang et al.*, 2014). It's a global ocean general circulation model based on unstructured triangle meshes, which solves the hydrostatic primitive equations with the finite element method. FESOM is the first matured global ocean general circulation model based on unstructured-mesh methods that has been developed for the purpose of climate research (*Sidorenko et al.*, 2014; *Rackow*, 2015). It consists of a 3D general ocean circulation model and a 2D dynamic-thermodynamic sea-ice model. In contrast to more traditional ocean models, FESOM is a new approach to simulate the global ocean circulation with variable mesh resolution and allows to resolve key regions, coastlines or narrow straits without involving additional nesting techniques.

2.1.1 Governing equations for the ocean component

The ocean component solves the standard set of hydrostatic primitive equations with Boussinesq and traditional approximations. The evolution of four main variables, as following, is modeled by discretizing the governing equations:

- $\vec{\mathbf{u}} = \vec{\mathbf{u}}(x, y, z, t) = (u(x, y, z, t), v(x, y, z, t), w(x, y, z, t))$ the three dimensional ocean velocity vector, unit: m s^{-1}
- $\eta = \eta(x, y, t)$ the sea surface height of the ocean, unit: m
- $S = S(x, y, z, t)$ the salinity of sea water, unit: g kg^{-1}
- $T = T(x, y, z, t)$ the potential temperature of sea water, unit: K

The variables vary with time $t >= 0$(unit:s) and spatial coordinates x, y and z. The horizontal coordinates x and y are given in m, but also be given as geographic coordinates longitude x_{lon} and latitude y_{lat} in degrees or radians East/West and North/South, respectively. The vertical coordinate z is given in m. The system of governing equations is split into two subproblems, the dynamical part and the thermodynamical part, which are solved separately. The dynamical part includes: the momentum equations 2.1 and 2.2, which describe temporal changes in horizontal velocities; the continuity equation 2.3, a result of the law of volume conservation; the assumption of hydrostatic balance for pressure as given in equation 2.4 which arises from the equation of vertical momentum balance; and the prognostic equation 2.5 for the sea surface height, which describes changes in sea surface elevation by influx or

efflux of mass.

$$\partial_t u + (\vec{\mathbf{u}} \cdot \nabla_3 u) - fv + \frac{1}{\rho_0}\partial_x p + g\partial_x \eta = \nabla \cdot A_h \nabla u + \partial_z A_v \partial_z u, \tag{2.1}$$

$$\partial_t v + (\vec{\mathbf{u}} \cdot \nabla_3 v) + fu + \frac{1}{\rho_0}\partial_y p + g\partial_y \eta = \nabla \cdot A_h \nabla v + \partial_z A_v \partial_z v, \tag{2.2}$$

$$\partial_x u + \partial_y v + \partial_z w = 0, \tag{2.3}$$

$$\partial_z p = -g\rho, \tag{2.4}$$

$$\partial_t \eta + \nabla \cdot \int_{z=-H}^{z=\eta} \begin{pmatrix} u \\ v \end{pmatrix} dz = P - E + R. \tag{2.5}$$

In this context $\partial_t u = \frac{\partial u}{\partial t}$, ∇ and ∇_3 stand for the 2-dimensional and 3-dimensional gradient and divergence operators, respectively. $f = \frac{4\pi}{86400}\sin(\theta)$ s^{-1}, is the Coriolis parameter dependent on the latitude θ and g is the gravitational acceleration $g = 9.81$ m s^{-2}. In the above equations, ρ_0 is the reference density $\rho_0 = 1000$ kg m^{-3}. For the density ρ, in kg m^{-3}, the equation of state $\rho = \rho(T, S, z)$ is applied, which relates density ρ to the potential temperature T and salinity S of sea water at a given depth z. Additionlly, lateral and vertical viscosities are given by A_h and A_v in $\mathrm{m}^2\mathrm{s}^{-1}$. In equation 2.5, $H = H(x, y)$ is total ocean depth (with respect to $z = 0$ m) in m, P-E is precipitation minus evaporation at the surface in m s^{-1} and R is the transport of freshwater by river runoff in m s^{-1}. In the thermodynamical part of the ocean model we solve the tracer equations for potential temperature T and salinity S:

$$\partial_t T + \vec{\mathbf{u}} \cdot \nabla_3 T = \nabla \cdot K_h \nabla T + \partial_z K_v \partial_z T, \tag{2.6}$$

$$\partial_t S + \vec{\mathbf{u}} \cdot \nabla_3 S = \nabla \cdot K_h \nabla S + \partial_z K_v \partial_z S, \tag{2.7}$$

In equations 2.6 and 2.7 K_h and K_v are the lateral and vertical diffusivity in $\mathrm{m}^2\mathrm{s}^{-1}$. Comparable to equations 2.1 and 2.2, equations 2.6 and 2.7 describe changes in T and S due to imbalance between the advection and diffusion terms.

2.1.2 Governing equations for the sea ice component

As the boundary between the ocean and atmosphere in the polar regions of earth, sea ice plays an important role in the climate system, especially as the central component and most sensitive indicator for the polar regions. First, one of the most important characteristics of sea ice is high albedo, causing sea ice to reflect more incoming solar radiation back to the atmosphere than the darker ocean water. Because of the large difference in albedo between sea ice and open water, sea ice can strongly affect the surface energy budget. Second, sea ice, acting as an insulating layer between atmosphere and ocean, modulates water mass, heat and momentum exchange between the two components. Third, the vertical structure of water mass and stability in high-latitude ocean can be influenced by brine and freshwater releases due to the sea ice formation and melting, further affecting the convection activities in deep and bottom water formation areas. Therefore, faithfully modelling sea ice with numerical models is of high importance to imporve the climate system simulation, as well as to help us better understand the physical mechanisms and interactions between different components of the climate system.

The sea ice component used in FESOM is a dynamic-theromdynamic sea ice model. The ice dynamics apply the approach by *Hunke and Dukowicz* (2002) and the ice thermodynamics mainly follow the work by *Parkinson and Washington* (1979) and *Semtner Jr* (1976). The model includes a snow layer, the presence of which affects sea ice growth and melting considerably (*Owens and Lemke*, 1990). The transformation of snow to ice by flooding with sea water is accounted for (*Matti*, 1983; *Fischer*, 1995). Heat storage within ice or snow is not considered. Instead, linear temperature profiles are assumed in both layers applying the zero-layer approach of *Semtner Jr* (1976). The detailed description of the sea ice model of FESOM can be found in *Timmermann et al.* (2009); *Danilov et al.* (2015).

For the sea ice model, on every grid nodes the equations for the quantities ice thickness, snow thickness, ice concentration and ice velocity are described. Ice thickness and ice concentration can change due to freezing

and melting (thermodynamic processes) and due to deformation, while the ice drift is affected by wind and ocean drag, the Coriolis force, the sea surface height gradient and internal forces within the ice (dynamic processes). Sea ice consists of individual ice floats which drift freely in regions of low ice concentration or is packed closely in regions of high ice concentration. The relevant prognostic variables for the sea ice are:

- $h = h(x, y, t)$ the effective ice thickness in m, defined as the ice volume per area averaged over the ice covered and ice-free part of the element
- $h_s = h_s(x, y, t)$ the effective snow thickness in m, defined in the same way as h
- $A = A(x, y, t)$ the sea ice concentration, a dimensionless quantity ranging from zero to one specifying the fraction of the ice-covered area of an element
- $\vec{\mathbf{u}}_i = \vec{\mathbf{u}}_i(x, y, t) = (u_i(x, y, t), v_i(x, y, t))$ the lateral sea ice (and snow on sea ice) drift velocity in m s^{-1}

Sea ice is assumed to be a two dimensional, quasi continuous fluid, therefore, vertical velocities are neglected. The evolution in time of the quantities h, h_s and A is described by the following continuity equations.

$$\partial_t h + \nabla \cdot (\vec{\mathbf{u}}_i h) = S_h, \tag{2.8}$$

$$\partial_t h_s + \nabla \cdot (\vec{\mathbf{u}}_i h_s) = S_s, \tag{2.9}$$

$$\partial_t A + \nabla \cdot (\vec{\mathbf{u}}_i A) = S_A, \tag{2.10}$$

The equations above describe the derivative in time of sea ice thickness h, snow thickness h_s and sea ice concentration A (the first terms on the left hand side) due to sea ice advection (dynamic processes, second terms on the left hand side) and sea ice thermodynamic changes terms S_h (m s^{-1}), S_s (m s^{-1}) and S_A (s^{-1}) on the right hand side. The sea ice thermodynamic changes include freezing and melting, snow fall and snow to ice transformation. The sea ice drift velocity $\vec{\mathbf{u}}_i = (u_i, v_i)$ is computed by the 2-dimensional momentum balance (*Hibler III*, 1979):

$$m(\frac{\partial \vec{\mathbf{u}}_i}{\partial t} + \vec{\mathbf{u}}_i \cdot \nabla \vec{\mathbf{u}}_i) = \vec{\boldsymbol{\tau}}_{air} + \vec{\boldsymbol{\tau}}_{ocean} - mf\vec{\mathbf{k}} \times \vec{\mathbf{u}}_i - mg\nabla\eta + \vec{\mathbf{F}}_{int}, \tag{2.11}$$

where $m = \rho_i h + \rho_s h_s$ is the mass per area in kg m^{-2}, and ρ_i, ρ_s denote the densities of sea ice and snow in kg m^{-3}, respectively. The advection term $\vec{\mathbf{u}_i} \cdot \nabla \vec{\mathbf{u}_i}$ is neglected in the discretization of the equation as it is of relatively small magnitude compared to the other terms. The effects of stress due to wind ($\vec{\boldsymbol{\tau}}_{air}$) and due to ocean velocity ($\vec{\boldsymbol{\tau}}_{ocean}$) are also included as shown on the right hand side. Coriolis force and the force due to the sea surface elevation are similar to those within the momentum balance for the ocean in 2.1 and 2.2. The last term on the right hand side, $\vec{\mathbf{F}}_{int}$ in N m^{-2}, represents the internal forces of the sea ice (per area) which counteract convergent or shear drift. The internal forces $\vec{\mathbf{F}}$ within the sea ice are expressed as the divergence of the stress tensor $\boldsymbol{\sigma}$: $\vec{\mathbf{F}} = \nabla \cdot \boldsymbol{\sigma}$. The internal stress tensor $\boldsymbol{\sigma}$ is construed according to the chosen rheology (*Hunke and Dukowicz*, 1997, 2002), which considers the sea ice as a nonlinear elastic viscous compressible fluid. The relation between stress $\boldsymbol{\sigma}$ and strain $\boldsymbol{\epsilon}$ is described by the following equations for the divergence D_D, the horizontal tension and shearing strain rates D_T and D_S, respectively:

$$D_D = \dot{\epsilon}_{11} + \dot{\epsilon}_{22} = \frac{1}{E}\frac{\partial \sigma_1}{\partial t} + \frac{\sigma_1}{2\zeta} + \frac{P}{2\zeta}, \tag{2.12}$$

$$D_T = \dot{\epsilon}_{11} - \dot{\epsilon}_{22} = \frac{1}{E}\frac{\partial \sigma_2}{\partial t} + \frac{\sigma_2}{2\eta}, \tag{2.13}$$

$$\frac{1}{2}D_S = \dot{\epsilon}_{12} = \frac{1}{E}\frac{\partial \sigma_{12}}{\partial t} + \frac{\sigma_{12}}{2\eta}. \tag{2.14}$$

where E is Young's modulus, $\sigma_1 = \sigma_{11} + \sigma_{22}$, $\sigma_2 = \sigma_{11} - \sigma_{22}$, here σ_{ij} represents the internal stress tensor of the ice, the ice strength P depends on the sea ice concentration A and the sea ice thickness h

$$P = P^* h \, \exp(-C(1 - A)), \tag{2.15}$$

Where P^* and C are empirical parameters set to 27500 Nm^{-2} and 20, respectively, the strain rate components

$$\dot{\epsilon}_{ij} = \frac{1}{2}\left(\frac{\partial u_i}{\partial x_j} + \frac{\partial u_j}{\partial x_i}\right) \tag{2.16}$$

the shear viscosity η, the bulk viscosity ζ and Δ are calculated from the formulas

$$\eta = \frac{P}{2\Delta}, \tag{2.17}$$

$$\zeta = \frac{P}{2e^2\Delta}, \tag{2.18}$$

$$\Delta = [D_D^2 + \frac{1}{e^2}(D_T^2 + D_S^2)]^{\frac{1}{2}}, \tag{2.19}$$

where e is an empirical parameter set to 2. The atmosphere/ice stress is given by

$$\vec{\boldsymbol{\tau}}_{air} = C_{d,ai}\,\rho_a\,(\vec{u_a} - \vec{u_i})|\vec{u_a} - \vec{u_i}|, \tag{2.20}$$

with the atmosphere-ice drag coefficient $C_{d,ai}$, the air density ρ_a and the wind velocity $\vec{u_a}$ and the ice/ocean stress is calculated by

$$\vec{\boldsymbol{\tau}}_{ocean} = C_{d,io}\,\rho_o\,(\vec{u_i} - \vec{u_o})|\vec{u_i} - \vec{u_o}|, \tag{2.21}$$

with ice-ocean drag coefficient $C_{d,io}$, the ocean density ρ_o and the ocean surface velocity $\vec{u_o}$. The heat conductivity of sea ice follows the scheme described by *Semtner Jr* (1976). The heat fluxes at the boundary between atmosphere and ocean, and in the ice-covered grid cell between atmosphere and sea ice, are:

$$Q_{ai,ao} = Q_{SW}^{\downarrow} + Q_{LW}^{\downarrow} + Q_{LW}^{\uparrow} + Q_s + Q_l, \tag{2.22}$$

where Q_{SW} and Q_{LW} stand for the short wave and long wave radiative fluxes, respectively. The symbols $\downarrow$ and $\uparrow$ stand for downwelling and upwelling radiative fluxes, respectively. Q_s and Q_l denote the turbulent fluxes of sensible and latent heat, respectively.

2.1.3 Discretization of FESOM

In FESOM, time derivatives are approximated using finite differences, while spatial derivatives are approximated by the finite element method. Instead of solving the equations for the variables u,v,w,η,S,T,A,h,h_s,u_i,and v_i con-

tinuously in time t and space (x, y, z), solutions are approximated at discrete times and locations. This makes it possible to approximate the temporal evolution of variables. The numerical schemes applied by FESOM are explained in details by *Wang et al.* (2014); *Danilov et al.* (2015). FESOM employs the unstructured meshes and the Finite Element(FE) method is implemented for solving the equations for the spatial domain. In two dimensions FESOM uses triangular surface meshes. Figure 2.1 shows the schematic of 2D basis functions on a triangular mesh. The value of basis function M_i is equal to one at grid node i and goes linearly to zero at its neighbour nodes; it equals zero outside the stencil formed by the neighbour nodes. The 3D mesh is generated by dropping vertical lines starting from the surface 2D nodes, forming prisms which are then cut into tetrahedral elements (shown in Fig. 2.2.) Except for layers adjacent to sloping ocean bottom each prism is cut into three tetrahedra; over a sloping bottom not all three tetrahedra are sued in order to employ shaved cells, in analogy to the shaved cells used by *Adcroft et al.* (1997). Keeping the 3D grid nodes vertically aligned is necessitated by the dominance of the hydrostatic balance in the ocean.

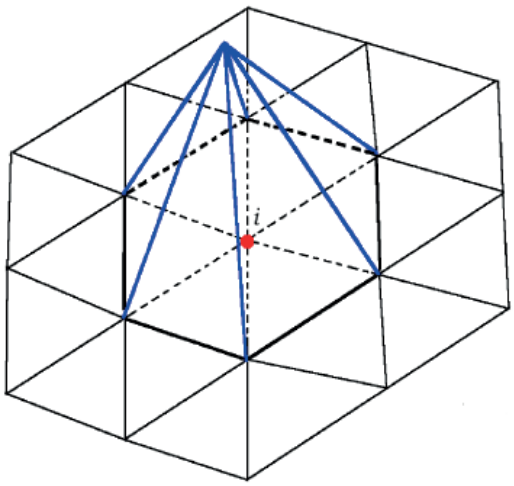

Figure 2.1: Schematic of horizontal discretization with illustration of basis functions used in FESOM. The stencil mentioned in the text consists of seven nodes for node i in the example shown in this figure

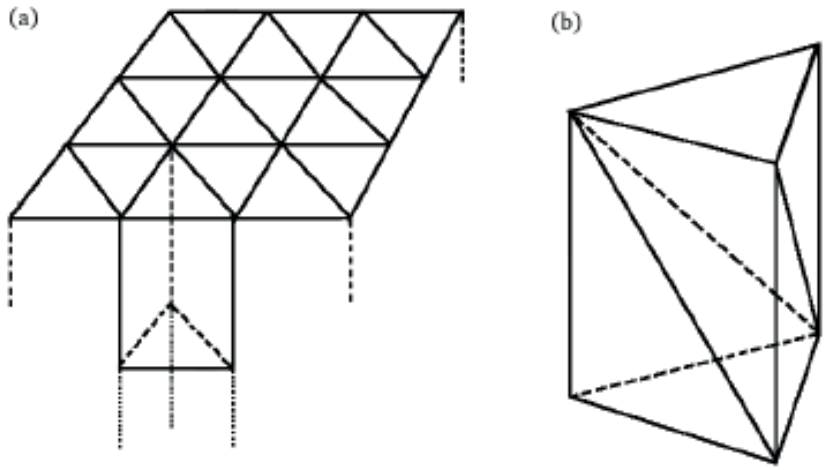

Figure 2.2: Schematic of spatial discretization. The column under each surface triangle is cut into prisms (a), which can be divided into tetradedra (b).

2.2 Atmospheric Forcing

In this study, the atmospheric forcing from the CORE (Coordinated Ocean-Ice Reference Experiment) project is used. The CORE framework defines protocols for performing global ocean-sea ice coupled simulations forced with a common atmospheric data set and using the same bulk formulas. The CORE data sets are collaboratively supported by the National Center for Atmospheric Research (NCAR) and the Geophysical Fluid Dynamics Laboratory (GFDL) under the umbrella of the Climate Variability and Predictability (CLIVAR) Working Group on Ocean Model Development (WGOMD). All data sets, codes for the bulk formulas, technical report, and other support codes along with the release notes are freely available at `http://data1.gfdl.noaa.gov/nomads/forms/core.html`. Two phases of forcing in this project are included. The first phase, namely CORE-I, uses a synthetically constructured, one-year repeating cycle of forcing, referred to as normal year forcing (*Large and Yeager*, 2004; *Griffies et al.*, 2009). The second phase of COREs, CORE-II, which is used in this thesis, uses the inter-annually

varing atmospheric forcing over the 60-year period from 1948 to 2007 (*Large and Yeager*, 2009). In the oceanographic community, the CORE-II simulations are usually referred to as hindcast experiments, which can be used to evaluate ocean and sea-ice model performance and study mechanisms of time-dependent ocean phenomena and their variability from seasonal to decadal time scales.

The CORE-II forcing data is provided on the T62 Gaussian grid with a zonal resolution of approximately 1.875 degree. The forcing fields used in this study are listed in Table 2.1. River runoff is based on the dataset by *Dai et al.*

Table 2.1: CORE-II atmospheric forcing fields used in this work.

variable	unit	resolution in time
10m zonal wind	m/s	6-hourly
10m meridional wind	m/s	6-hourly
10m air temperature	K	6-hourly
10m specific humidity	kg/kg	6-hourly
precipitation	mm/s	monthly
downward shortwave radiation	W/m^2	daily
downward longwave radiation	W/m^2	daily

(2009), which contains the monthly streamflow at the farthest downstream stations of the world's 925 largest ocean-reaching rivers. The simulations were initialized with the mean temperature and salinity fields from the Polar Hydrography Center global ocean climatology version 3 (PHC 3.0, *Steele et al.*, 2001). The initial sea ice concentration and thickness were taken from the long term mean of a previous simulation.

Chapter 3

Long-term ocean simulations in FESOM: evaluation and application in studying the impact of Greenland Ice Sheet melting

3.1 Introduction

Models formulated on unstructured meshes offer geometrical flexibility which is difficult to achieve on traditional structured grids. The resolution refinement on unstructured meshes can be considered as an effective nesting algorithm, which is valuable for many practical tasks. The Finite Element Sea-ice Ocean Model (FESOM) was designed with this idea in mind. It uses triangular surface meshes and generalized vertical discretization, and offers necessary parameterization commonly used in large-scale ocean modeling. There are, however, numerous implementation details that differ from structured-mesh models, which may influence the model performance over long integration time. Therefore, a careful examination of model behavior on long time scales is required. This was partly the focus of the intercom-

parison of FESOM (*Sidorenko et al.*, 2011) to other models participating in the project of Coordinated Ocean-ice Reference Experiments (COREs) under normal year forcing (*Griffies et al.*, 2009). The current paper is a following step in this direction and deals with long-term FESOM simulations under CORE interannual forcing with and without freshwater contribution from the Greenland Ice Sheet (GrIS) melting.

The accelerated melting of the GrIS, associated to global warming, may significantly impact the entire climate system and the ocean in particular (*Fichefet et al.*, 2003; *Stouffer et al.*, 2006; *Gerdes et al.*, 2006; *Jungclaus et al.*, 2006; *Swingedouw et al.*, 2006, 2007; *Stammer*, 2008; *Stammer et al.*, 2011; *Hu et al.*, 2009, 2011; *Kopp et al.*, 2010). The increasing freshwater input can affect the ocean in several ways. First, it leads to the global sea level (GSL) rise due to added mass. The local sea level (LSL) change differs from the GSL change because of contributions linked to ocean dynamics (dynamical sea level (DSL) change due to steric height response and change in circulation) and change in static equilibrium (SE) caused by the gravitational, elastic and rotational effects of mass redistribution. Although the GSL rise can easily be estimated for a given discharge rate from Greenland, LSL change remains a topic of ongoing research. Climate models are required to estimate the DSL response, while glacial rebound modeling is required to assess the SE effects. Second, the added freshwater influences the ocean circulation by stabilizing the water column in the deep convection sites, thus suppressing the Atlantic Meridional Overturning Circulation (AMOC) and meridional heat transport. Understanding such effects is crucial for understanding the climate change and requires climate model-assisted studies. This is a key topic of many recent climate studies as in the literature mentioned above.

Despite numerous studies of the AMOC response to increased GrIS melting, the predicted response is still a matter of debate. *Fichefet et al.* (2003) and *Swingedouw et al.* (2006, 2007) found a substantial suppressing effect of GrIS melting on AMOC, while *Jungclaus et al.* (2006) suggested that the backbone of the AMOC can be maintained in the scenario of warming climate and increased GrIS melting, even though the deep convection is significantly reduced in the Irminger and Labrador Seas. *Stouffer et al.* (2006) analyzed

a suit of climate model simulations to assess the influence of GrIS freshwater input on the AMOC. All models in their study simulated weakening of the AMOC due to freshwater from GrIS, but the spread of AMOC reduction among these models was approximately 1.5–9 Sv. Thus, a quantitative prediction remains a tough problem at the current stage, and the goal of numerous model studies lies in exploring possible mechanisms through which the added freshwater influences the sea level and meridional overturning circulation. The uncertainties in the simulations can be further increased by the uncertainties in model predictions for future radiative forcing scenarios as addressed in the past IPCC reports. Notwithstanding the spread of model results in aforementioned studies, in our work they provide the possibility to evaluate the FESOM simulation through intercomparison.

Ocean models driven by prescribed atmospheric forcing neglect the feedbacks between the ocean and atmosphere (see, e.g., discussions by *Griffies et al.*, 2009). Another drawback is their use of sea surface salinity (SSS) restoring as the practical remedy for mixed boundary conditions (see, e.g., discussions by *Gerdes et al.*, 2006). However, due to the complexity of coupled climate models and even larger uncertainties in coupled model simulations, hindcast simulations remain the primary way to evaluate ocean models in the ocean modeling community (*Griffies et al.*, 2009).

In this work, we use hindcast experiments with CORE interannual atmospheric forcing (*Large and Yeager*, 2009) to study FESOM's long-term behavior. The freshwater input from the GrIS melting is added in a water-hosing experiment to study the associated ocean response. The focus is on the direct effects of increased freshwater input on the ocean circulation, including the changes in DSL, Atlantic circulation and the Arctic Ocean. Long-term model integration using two different scenarios allows to assess the model skills in both reproducing the past ocean state and simulating one particular impact of future climate change. *Marsh et al.* (2010) used an eddy-permitting global ocean model to study the short-term (on a few years time scale) ocean response to sudden GrIS freshwater discharge. For our purpose, we used a coarse mesh to study the model long-term behavior, as done in most aforementioned studies. The paper is organized as follows. Section 2

describes the model configuration. The model state without GrIS melt water input is analyzed in Section 3. The focus is on the main ocean indices and characteristics in the North Atlantic and Arctic Ocean, which are the two regions mainly discussed when studying the influence of GrIS freshwater in the following section. Section 4 compares the experiments with and without the GrIS freshwater input. Conclusion and discussions are given in the last section.

3.2 Model setup

We use nominal 1.3 ° horizontal resolution in the bulk of the open ocean, and take the advantage of FESOM geometric flexibility to refine the resolution to 20 km along the coastlines and 40 km in the equatorial belt. This allows us to better resolve the ocean geometry and the equatorial transient processes. As the North Pole is displaced onto the Greenland, the resolution is also about 20 km in its vicinity. The minimal horizontal resolution of 20 km still allows us to use a large time step (45 min) to carry out long-term integrations. For our current purpose, we did not apply further mesh refinement in other particular regions. We use 39 vertical z levels, with 10-m thickness in the top ten layers.

The Redi diffusion (*Redi*, 1982) and the Gent and McWilliams parameterization (*Gent and Mcwilliams*, 1990) are applied with the critical neutral slope of 0.004. The skew diffusivity is the same as the isopycnal diffusivity, which is parameterized as $V\Delta$, where $V = 0.006$ m s^{-1}, and Δ is the square root of surface triangle area. The horizontal biharmonic viscosity is $B\Delta^3$, where $B = 0.027$ m s^{-1}. Vertical mixing is provided by the Pacanowski and Philander scheme (*Pacanowski and Philander*, 1981) with the background vertical diffusion of 10^{-4} m^{2}s^{-1} for momentum and 10^{-5} m^{2}s^{-1} for tracers, and the maximum value is set to 0.01 m^{2}s^{-1}. The mixing scheme by *Timmermann et al.* (2002) is introduced (the diffusivity of 0.01 m^{2}s^{-1} is applied over a depth defined by the Monin–Obukhov length when it is positive) in order to avoid unrealistically shallow mixed layers in summer. The performance of FESOM with a similar configuration forced by the climatology forcing

(CORE normal year forcing, *Large and Yeager*, 2004) has been discussed by *Sidorenko et al.* (2011).

The ocean is initialized with steady velocity and the annual mean potential temperature and salinity climatology of the World Ocean Atlas by *Conkright et al.* (2002). The sea ice is initialized with results from previous simulations. The model is forced by the CORE interannual forcing from 1948 to 2007 (*Large and Yeager*, 2009). The drag and heat exchange coefficients used in the bulk formula are computed following the suggestion of *Large and Yeager* (2004). The SSS is relaxed toward the monthly climatology with a piston velocity of 50 m/300 day. The total surface restoring flux is normalized to 0 at every time step.

The model is first spun up for 120 years (two cycles of 1948–2007 forcing) and then integrated further in two setups: One is the control run which just continues from the spin-up results, and the other is the water-hosing experiment in which the freshwater forcing due to GrIS melting is added around Greenland. Both of them are integrated for two cycles of 60 years. In the water-hosing experiment, the extra freshwater released from the GrIS is uniformly distributed along the Greenland coast south of 76 °N. The total added freshwater flux is 0.1 Sv, the same as in previous studies by *Stouffer et al.* (2006); *Stammer* (2008); *Stammer et al.* (2011); *Lorbacher et al.* (2012). The melting water is applied from May to October. The freshwater flux used here is larger than in the current climate situation, but it is chosen to represent a possible future climate scenario as done in previous studies.

In the water-hosing experiment, a passive tracer is introduced to trace the pathway of freshwater from Greenland as suggested by *Gerdes et al.* (2006). It is set to 0 everywhere at the beginning of the experiment. A virtual salt flux (the product of runoff from GrIS melting and local sea surface salinity) leaving the ocean is applied as the surface boundary condition for the passive tracer equation. It is solved using the same equation as for the active tracers.

3.3 Simulated state in the control run

The model performance in the control run is analyzed in this section with focus on the North Atlantic and the Arctic Ocean. We will focus on these areas in the comparison between the control and the water-hosing runs in Section 4.

3.3.1 The North Atlantic

The AMOC is the major component of the global ocean thermohaline circulation, which plays a crucial role in the climate system. Its transport and structure are important for maintaining a realistic ocean state (*Griffies et al.*, 2009). The time series of the annual mean AMOC index, defined as the maximum of the AMOC streamfunction at 45 °N beneath the wind driven Ekman layer, is shown in Figure 3.1a. The first two cycles of integration with repeated CORE interannual forcing (120 years) are the spin-up phase needed to reach a quasi-equilibrium state in the upper and intermediate ocean. The mean strength of the simulated AMOC during the last two cycles is about 14 Sv, with the standard deviation of 1.7 Sv. The simulated AMOC transport compares well with the estimated mean values based on observations, 13 ± 2 Sv at 42 °N (*Lumpkin and Speer*, 2003) and 16 ± 2 Sv at 48 °N (*Lumpkin et al.*, 2008). Although it is near the lower bound of the observed range, the model result is comparable to previous model simulations (e.g., *Griffies et al.*, 2009).

The AMOC streamfunction averaged over the last 10 years of the control run is shown in Figure 3.1b. The AMOC system consists of two main overturning cells, an intermediate with southward-flowing North Atlantic Deep Water (NADW) and an abyssal one with Antarctic Bottom Water (AABW), both of which are well captured in our control integration. The intermediate cell spans the whole Atlantic in both hemispheres with the maximum located at about 1000 m, while the abyssal one with a strength of 2–3 Sv is centered around the 3500–4000 m depth.

The NADW, which feeds the intermediate cell of the AMOC, is largely

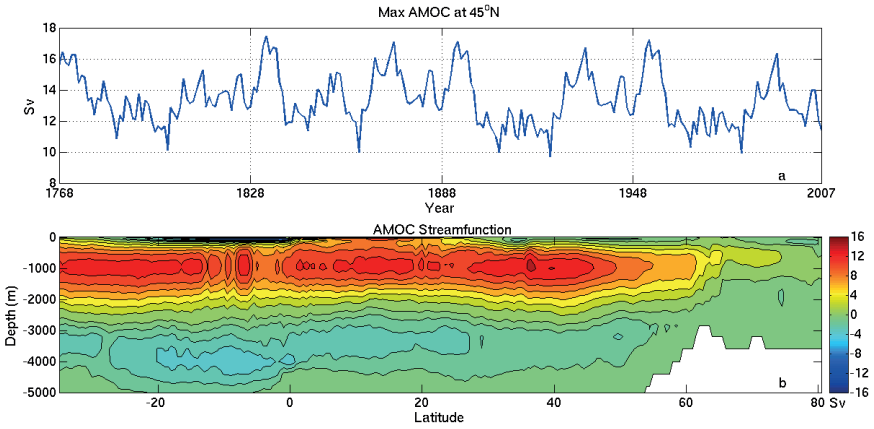

Figure 3.1: a) Time series of the AMOC index for the four cycles in the control run (time axis is made continuous). The index is defined as the maximum of the annual mean AMOC streamfunction at 45 °N. b) AMOC streamfunction averaged over the last 10 years in the control run.

sustained by the deep convection and water-mass ventilation in the Labrador and GIN (Greenland–Iceland–Norwegian) Seas. The analysis by *Latif et al.* (2006) indicates that the outflow from GIN seas plays a secondary role in determining the AMOC variability during the past decades. The Labrador Sea is a region where intense air–sea interaction occurs and strong convective processes create dense Labrador Sea Water (LSW), the upper constituent of the NADW. The mixed layer depth (MLD) in the Labrador Sea can be used as a simple measure of convection and LSW formation intensity. The decadal variability of the deep western boundary current (DWBC) transport at 53 °N in the southwestern Labrador Sea follows that of the Labrador Sea MLD with a lag of 1–2 years, which indicates that the DWBC represents a signal of primarily thermohaline origin (*Böning et al.*, 2006).

The anomalies of the DWBC transport at 53 °N and the Labrador Sea MLD during the last control run cycle are plotted in Figure 3.2a. The DWBC is defined using the criterion that the potential density (σ_θ) is larger than 27.74 kg m^{-3}. The MLD index is calculated as the March mean MLD averaged over a chosen box ($55 - 53\,°\mathrm{W}, 56.5 - 58.5\,°\mathrm{N}$) in the Labrador Sea. Here, The MLD is defined as the depth where the buoyancy anomaly becomes

greater than 0.0003 m s^{-2} relative to the surface. The DWBC transport well corresponds to the variability in the convection intensity in the Labrador Sea, with a correlation coefficient of 0.6 for a lag of 1 year. The stronger southward DWBC transport episodes are apparently associated with deeper Labrador Sea MLD in the mid-1970s, mid-1980s and most prominently, early 1990s, consistent to the finding by *Böning et al.* (2006).

The DWBC plays an important role in exporting the deeper water masses formed in the subpolar gyre southward to feed on the meridional overturning circulation, as well as in setting the variability of the exported water mass and AMOC (*Böning et al.*, 2006; *Palter et al.*, 2008; *Bower et al.*, 2009; *Cunningham et al.*, 2010). It can well explain the variability of the AMOC further to the south (*Eden and Greatbatch*, 2003; *Böning et al.*, 2006). Figure 3.2b illustrates the variability of DWBC transport at 53 °N and the AMOC transport at 45 °N. The former leads the latter with a correlation coefficient of 0.81 for a lag of 1 year. This relationship indicates that the signal of AMOC is linked to the variability of upstream deep water transport, especially on the decadal time scale. The MLD in the Labrador Sea leads the AMOC at 53 °N by about 2 years in our simulation, as also shown by *Eden and Greatbatch* (2003).

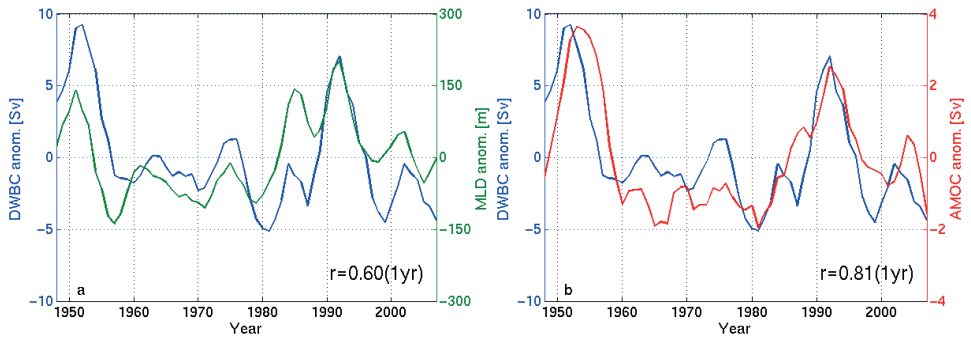

Figure 3.2: a) Anomalies of the Deep Western Boundary Current (DWBC) transport at 53 °N and the mixed layer depth (MLD) in the Labrador Sea in the fourth cycle of the control run. b) The same as (a) but for the DWBC transport and the Atlantic Meridional Overturning Circulation (AMOC) index at 45 °N.

3.3.2 The Arctic Ocean

The Arctic Ocean stores a large amount of freshwater in both solid (sea ice) and liquid form. The variability in freshwater storage and freshwater exchange through critical gateways influence the global large-scale ocean circulation. Simulating reasonable sea ice coverage pattern and freshwater balance is the prerequisite for an adequate representation of the large-scale ocean circulation and global climate.

Figure 3.3 shows the simulated Arctic mean sea ice concentration in March (Figure 3.3a) and September (Figure 3.3c), compared with the observed sea ice concentration from NSIDC, shown in Figure 3.3b and Figure 3.3d (*Cavalieri et al.*, 1996)[updated yearly]. March and September have the maximum and minimum Arctic sea ice extent, respectively. Generally, the model reproduces the realistic sea ice coverage in the Arctic Ocean. In winter, the most part of the Arctic is covered with high concentration sea ice due to the ice formation in cold conditions. The model well represents the ice edge around the Arctic periphery. The pronounced Arctic sea ice retreat in September is also well captured, although the sea ice area is slightly overestimated in some marginal seas, including Baffin Bay, Barents and Kara Seas.

The total liquid freshwater content in the Arctic Ocean is diagnosed via $\iint_A \int_H^0 \frac{S_{ref}-S}{S_{ref}} dzdA$, where S is salinity, $S_{ref} = 34.8$ is the reference salinity, z is water depth, H is the ocean depth where S reaches S_{ref}, and A is the surface area (over the Arctic region). It increases significantly during the first model cycle, as in the spin-up phase of other global models (e.g., *Köberle and Gerdes*, 2007), while it is very similar during the last two model cycles (with very close magnitude and variability, not shown). Figure 3.4a shows the anomaly of the total Arctic liquid freshwater content for the last model cycle. This time series is qualitatively similar to those of *Häkkinen and Proshutinsky* (2004); *Köberle and Gerdes* (2007); *Lique et al.* (2009), with maxima in late 1960s, at the beginning and end of 1980s, and end of 1990s, and minima in 1976, 1987, and 1996. The standard deviation of the liquid freshwater content is 2.07×10^3 km^3, about 2% of the long-term mean.

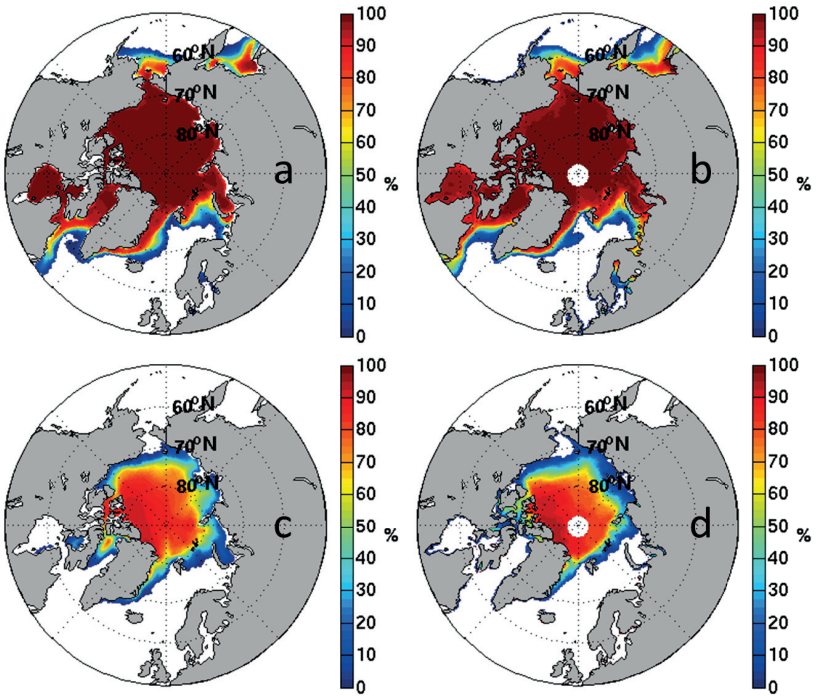

Figure 3.3: Simulated mean sea ice concentration in a March and c September, compared to NSIDC datasets in b March and d September. The average period is between 1989 and 2007.

The liquid freshwater content variation is due to both the surface freshwater fluxes (precipitation - evaporation + river runoff and ice melting and freezing) and lateral freshwater exchange through the main gateways. The Arctic Ocean receives freshwater contribution from the Pacific through Bering Strait, and releases freshwater to the North Atlantic through Fram Strait and the Canadian Arctic Archipelago (CAA) channels. The relationship between the total lateral freshwater transport and the derivative of the Arctic Ocean freshwater content is shown in Figure 3.4b. The variability of the freshwater content in the Arctic Ocean can be largely explained by that of the total freshwater transport through the gateways. The correlation coefficient between the two terms is 0.79. As shown in previous model studies (*Häkkinen and Proshutinsky*, 2004; *Köberle and Gerdes*, 2007; *Lique et al.*, 2009), the lateral advective flux has a leading role in the freshwater content variability. Fram Strait is the gate not only for fresh water export, but also for the in-

flow of warm saline water of Atlantic origin. The change in the property of the Fram Strait inflow in the GrIS melting scenario can modify the Arctic freshwater content significantly (see Section 3.4.3).

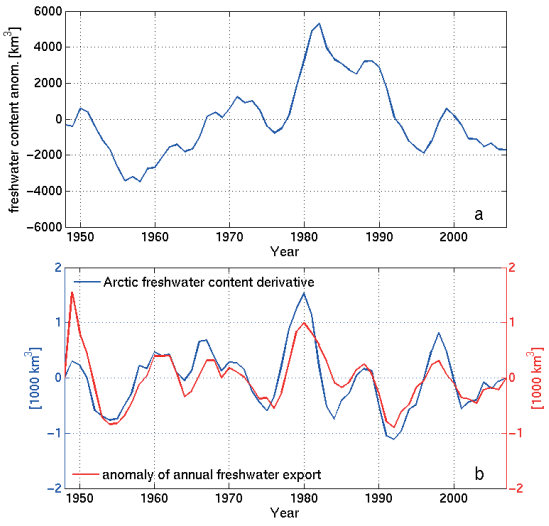

Figure 3.4: a) The anomaly of the total Arctic liquid freshwater content (cubic meter) in the last model cycle of the control run, b) Arctic freshwater content derivative and the anomaly of the total freshwater flux though all gates of the Arctic Ocean.

3.4 The GrIS melting scenario

3.4.1 Global dynamical sea level change

The GSL change directly induced by the added water mass is equilibrated through fast barotropic processes. The global barotropic adjustment just takes several days to redistribute the sea level rise globally over the entire ocean. As argued by *Gower* (2010); *Lorbacher et al.* (2012), the actual addition of freshwater leads to a much larger magnitude in the GLS rise than the local DSL rise at most sites. A melting rate of 0.1 Sv gives a GSL rise

rate of approximately 8.8 mm/year. However, the DSL response is still important locally on this background. Pronounced DSL rise northeast of the North America has been observed in most water-hosing simulations (*Stammer*, 2008; *Hu et al.*, 2009; *Yin et al.*, 2009; *Kopp et al.*, 2010). Note that the static equilibrium (SE) contribution should be accounted for to get the full sea level rise signal. With a GrIS melting rate of 0.1 Sv, the magnitude of sea level depression due to SE can outweigh the DSL rise in the North Atlantic, even in the region where DSL rise is the largest (*Kopp et al.*, 2010). As the ocean circulation and its representation in FESOM is the main topic of this work, we will only focus on the DSL change here, although assessing the future risk of sea level rise requires taking all contributions into account (*Slangen et al.*, 2012).

The modeled sea surface height is corrected as suggested by *Greatbatch* (1994); *Griffies and Greatbatch* (2012), since the model uses the Boussinesq approximation. The DSL response to the freshwater input induced by GrIS melting is illustrated in Figure 3.5. The time evolution of annual mean DSL difference between the water-hosing and control runs is shown (for years 2, 4, 6, 10, 15 and 20). The DSL adjustment is dominated by baroclinic wave and advective processes and is much slower than the barotropic GSL adjustment process. As the GrIS freshwater is added along the Greenland coast south of 76 °N, the immediate DSL change largely occurs near the Greenland coast especially in Baffin Bay and Greenland Sea. In the Baffin Bay, the signals of positive DSL anomaly are mainly confined within the local currents at the beginning of the experiment, including the northward West Greenland Current and the southward Baffin Island Current. The signals of DSL anomaly in the Greenland Sea propagate along the boundary and penetrate into the Arctic Ocean. After 4 years, the DSL anomaly spreads into the North Atlantic along the subpolar gyre. Then the signals are carried by the North Atlantic Current and spread poleward. Meanwhile, the DSL anomaly also propagates southward from the Labrador Sea toward the equator, where it continues along the equator in form of equatorial Kelvin waves and then propagates poleward along the eastern coast, carrying the signals to the whole Atlantic basin in both hemispheres in form of Kelvin and Rossby waves.

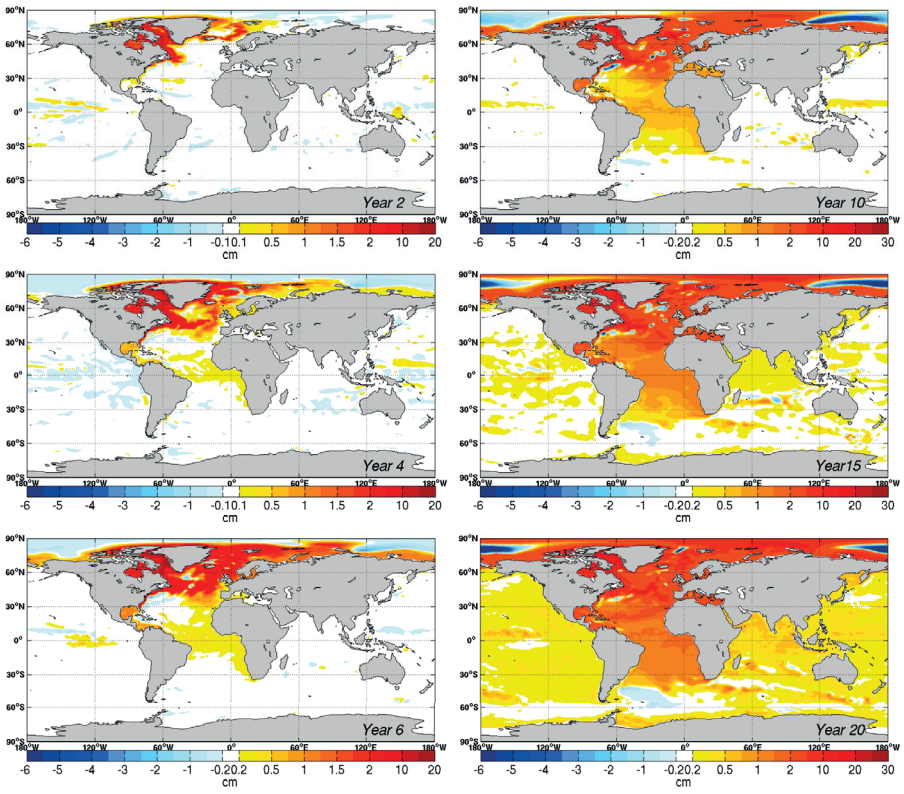

Figure 3.5: Annual mean dynamic sea level anomaly for model year 2, 4, 6, 10, 15, 20. The anomaly is calculated by subtracting the control run result from water-hosing run result. Note the non-uniform color scale.

The "fingerprints" of the wave propagation become more obvious with time as their amplitude increase. After 10 years, the DSL anomaly covers the whole Atlantic basin. The sea level change signal is carried to the Indian basins across the southern tip of Africa and after about 15 years it covers the Indian Ocean. It takes about 20 years for the DSL signal to cover the whole Pacific Ocean. However, the magnitude of the DSL change is much larger in the Atlantic and Arctic Oceans.

As indicated in Figure 3.5, the propagation pathways of the DSL anomaly, one to the subpolar and Arctic regions and one to the Indian and Pacific basins, are dominated by different processes. Advective processes govern the adjustment of DSL change in subpolar and Arctic regions, while the southward propagation is dominated by Kelvin and Rossby waves. The latter

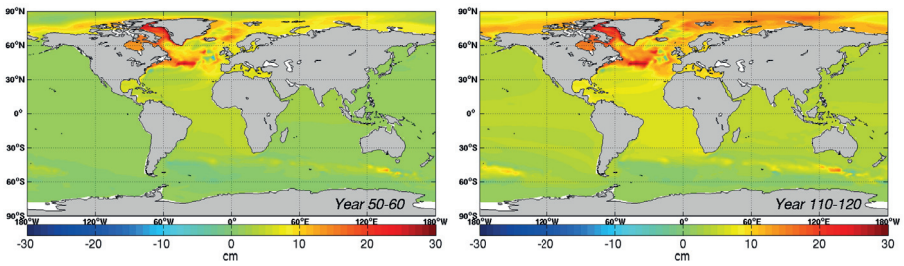

Figure 3.6: Mean dynamic sea level change for model year (left) 50-60 and (right) 110-120. The change is calculated by subtracting the control run result from the water-hosing run result.

pathway was also discussed in previous studies (e.g., *Stammer* (2008)). The southward propagation in form of Kelvin and Rossby waves in our experiment is similar to that in the study of *Stammer* (2008), although it is less visible on the background of stronger advective propagation: the positive DSL anomaly first fills the South Atlantic and then penetrates into Indian Ocean around the Good Hope, and finally reaches the Pacific Ocean. However, there is noticeable difference for the North Atlantic and Arctic regions compared to the work of *Stammer* (2008), in which the Arctic Ocean was absent. Our study shows that the most significant DSL change occurs in the northern North Atlantic and Arctic Ocean through advection. The impact of GrIS melting on the Arctic Ocean will be further discussed in Section 3.4.3.

Figure 3.6 shows the mean DSL change for year 50-60 (left) and 110-120 (right). The magnitude of DSL change continues to increase with time, but its spatial distribution is far from being uniform. The sea level anomaly is obviously the largest in the North Atlantic and the Arctic Ocean. By the end of our experiments, the largest DSL rise is observed in Baffin Bay, Labrador Sea, and northeast of the North America. The DSL anomaly northeast of the North America, reaching about 30 cm, is rather significant even compared to the mean GSL rise of about 1 m (from 0.1 Sv melting rate for 120 years). This result is consistent to previous studies (*Hu et al.*, 2009; *Kopp et al.*, 2010). *Yin et al.* (2009) suggested that the DSL rise in west North Atlantic can be linked to the weakening of the AMOC, which we will address in Section 3.4.4.

3.4.2 Freshwater distribution and ocean salinity change

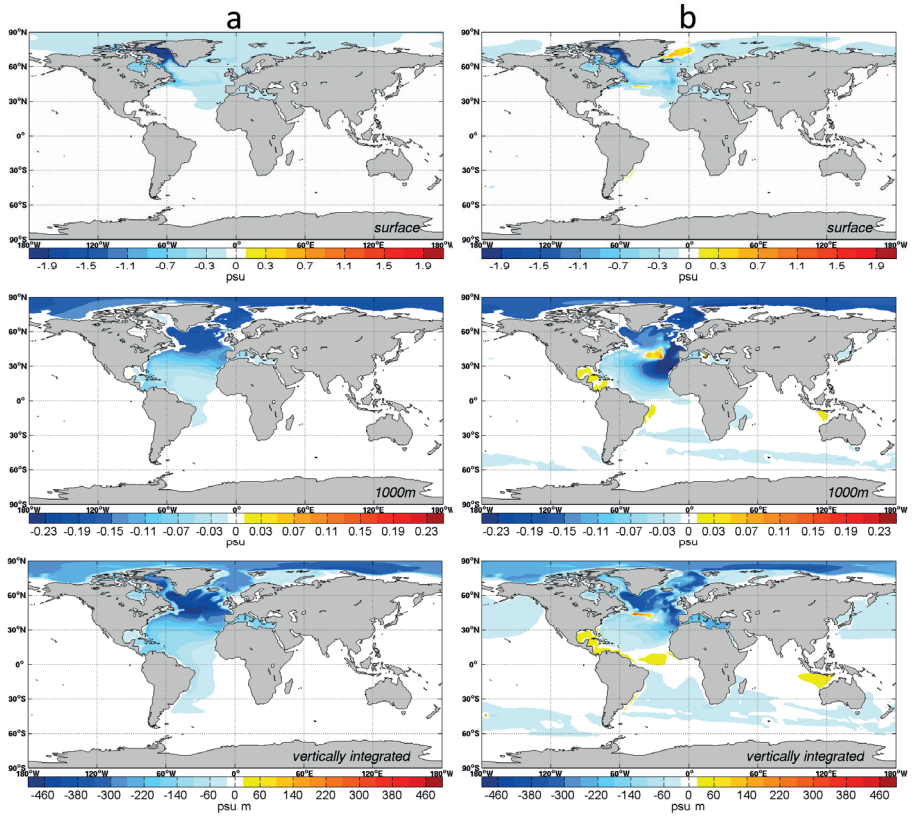

Figure 3.7: a) GrIS melt water passive tracer and b) salinity difference between the water-hosing and control runs. From top to bottom are for the surface, 1000m depth (practical salinity unit) and the vertically integrated value (practical salinity unit per meter). The mean fields over the last ten model years are plotted.

Figure 3.7a presents the passive tracer at two depths and its vertically integrated value averaged over the last 10 years. It shows the direct freshening effect of GrIS melt water, because the passive tracer is an indicator of the melt water distribution in the ocean. At the sea surface, a large amount of GrIS water is accumulated in Baffin Bay. A significant amount is also distributed over the northern North Atlantic and the Arctic Ocean. At depth, the northern North Atlantic and Arctic Ocean are still the major residence locations of the GrIS melt water, although it is obviously present in the whole

North Atlantic and the western South Atlantic. The pattern of the vertically integrated signal is similar to that from Gerdes et al. (2006), with highest value in the North Atlantic subpolar gyre. The Arctic Ocean receives GrIS melt water at different depth through the North Atlantic current, while the South Atlantic receives melt water through the deep limb of the (weakened but not collapsed) meridional overturning cell.

The salinity anomaly (difference between the water-hosing and control runs) at different depth and its vertically integrated value are shown in Figure 3.7b. Significant freshening mainly occurs in the northern North Atlantic and Arctic Ocean, similar to the changes implied by the GrIS water distribution (Figure 3.7a). However, there is a pronounced difference between the salinity anomaly and the passive tracer at intermediate depth in the eastern North Atlantic, where fresher intermediate water is formed. Clearly, this water is not GrIS melt water origin, but due to the ocean circulation adjustment. A very similar result was obtained by *Gerdes et al.* (2006), who conducted the water-hosing experiment with an intermediate complexity climate model. They showed that the minimum salinity in the western boundary current will increase at the beginning of the simulation as the supply of the relatively fresh LSW is reduced due to suppressed deep convection, while the westward spreading of this freshwater pool can finally lead to a decrease in the salinity at the western boundary. Similar to their result, the salinity anomaly in our North Atlantic is negative by large, including the western boundary region. The vertically integrated salinity anomaly is positive along the coast starting from Gulf of Mexico and Caribbean Sea to the south. This is also similar to the finding of *Gerdes et al.* (2006), but the anomaly magnitude in our model is much smaller. The salinity anomaly pattern (largely negative) in the South Atlantic is different to their results (largely positive). The difference can be due to different ocean adjustment in the South Atlantic or missing atmospheric feedbacks in our experiment, which need to be explored in future work. The northern North Pacific becomes fresher because less freshwater is transported into the Arctic Ocean in the water-hosing run (see Section 3.4.3).

A zonal band of positive salinity anomaly is present near the Gulf Stream

Extension both at the intermediate depth and in the vertically integrated field (Figure 3.7b), which can be simply due to the shift of the mean Gulf Stream path. Figure 3.8 shows the mean kinetic energy at surface averaged over the last ten model years for both runs. In the water-hosing run, the axis of the Gulf Stream Extension shifts by about 1 ° northward to 44 °N, where we see the zonal salinity anomaly. The reduction of the Gulf Stream kinetic energy in the water-hosing experiment is consistent to the reduction of the AMOC strength (see Section 3.4.4).

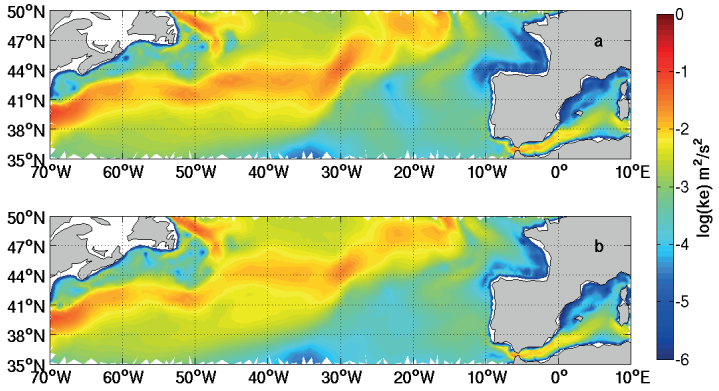

Figure 3.8: Mean kinetic energy at surface averaged over the last ten model years in a control and b water-hosing runs on logarithmic scale.

3.4.3 The influence on the Arctic Ocean

The Atlantic Water (AW) enters the Arctic Ocean via both Fram Strait and Barents Sea. The two branches meet near the St. Anna Trough. Surface cooling in the Barents Sea increases the AW density, which helps the AW in the Barents Sea branch to penetrate deeper into the Eurasian Basin. Figure 3.9a shows the vertically integrated passive tracer in the Arctic Ocean. A large amount of GrIS water accumulates in the Arctic basins, while the Eurasian Basin has the largest concentration due to the direct access to the AW inflow. The Arctic boundary currents are steered by the bottom topography, in particular the Lomonosov Ridge separating the Eurasian and Amerasian Basins, therefore a large amount of passive tracer is located in

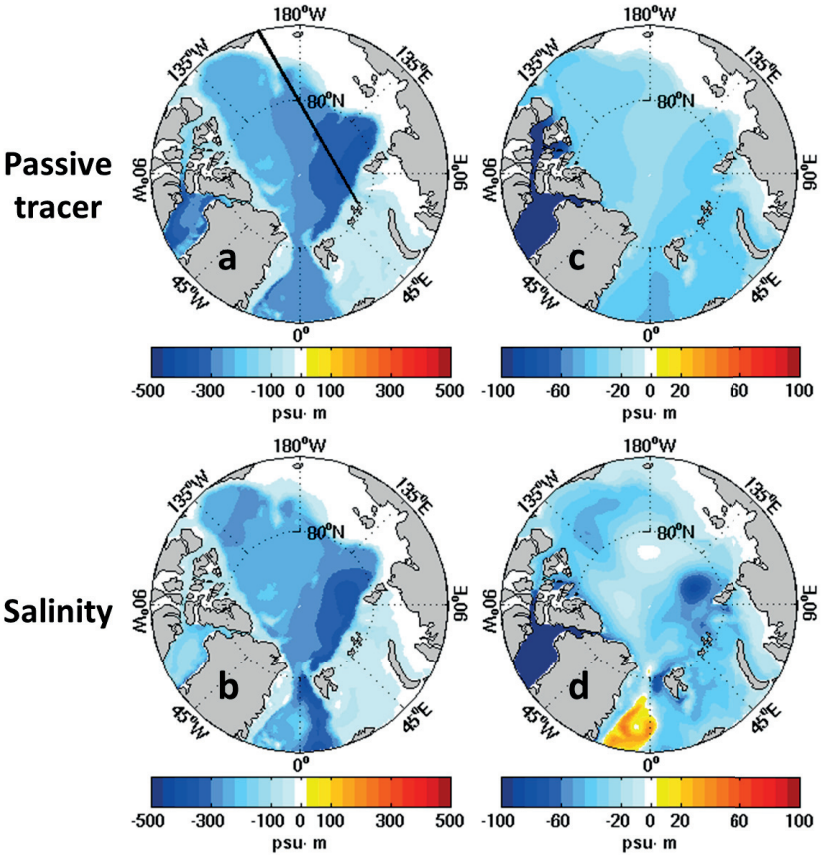

Figure 3.9: Vertically integrated a) passive tracer (practical salinity unit meter) and b) salinity anomaly (practical salinity unit meter) averaged over the last ten model years. The integration is from ocean surface to bottom. c) and d) are the same as a) and b), but for the integration over the upper 200m depth.

the Eurasian Basin. Accordingly, the largest negative salinity anomaly is also there (Figure 3.9b). The patterns of salinity change and passive tracer are different in their details due to the ocean dynamical adjustment, as for the case in the North Atlantic (Figure 3.7). The vertically integrated passive tracer and salinity anomaly for the upper 200m depth are shown in Figure 3.9c, d, respectively, comparing which with Figure 3.9a, b indicates that the salinity anomaly reaches deeper depth. The passive tracer has high concentration in both basins. The salinity anomaly has a similar pattern, but with clearly intensified magnitude in the Eurasian and south Canadian Basins.

Figure 3.10 compares the vertical structure of the passive tracer and salinity anomaly in a transect from the Franz Josef Land to the Canadian Basin (location marked in Figure 3.9a with a solid black line). The passive tracer penetrates mainly over the upper 2000m depth, including the surface layers and the AW layer, and the ocean freshening is also mainly within this depth range. The most pronounced difference between the passive tracer and salinity anomaly is in the upper 200m depth. As also indicated in Figure 3.9d, the salinity reduction in the upper central Arctic is much less than in the south Canadian Basin. In the deep AW layer, the salinity reduction is slightly less than the freshening indicated by the passive tracer.

Figure 3.11a shows the DSL change averaged over the last 10 years. In the Arctic Ocean, the most pronounced DSL rise is in the Eurasian Basin and along the shelf regions. Similar to the surface circulation change implied by the sea level gradient, the barotropic streamfunction shows a positive anomaly in the Eurasian Basin and a negative anomaly centered over the Mendeleev Ridge (Figure 3.11b). A very fresh surface water layer resides above the halocline in the Canadian Basin and the changes in circulation can lead to changes in the distribution of the freshwater. The typical clockwise surface circulation brings the freshwater in the Canadian Basin close to the Transpolar Drift current, which then brings part of the fresh water to the Fram Strait. The negative streamfunction anomaly implies more freshwater remains in the south and central Canadian Basin and less discharge to the region over the Mendeleev Ridge (Figures 3.9d and 3.10b). The positive barotropic streamfunction anomaly in the Eurasian Basin indicates that the AW inflow is weakened (Figure 3.11b). The relatively saltier AW meets the freshwater from the Transpolar Drift west of Severnaya Zemlya. The salinity at this point is influenced not only by the AW salinity, also by the strength of the AW inflow. Weaker AW current results in lower salinity at this place, where the most pronounced negative salinity anomaly is observed (Figures 3.9d and 3.10b).

The Arctic receives net volume inflow through Barents Sea opening and Bering Strait, and loses net volume through Fram Strait and Davis Strait. The change in sea surface height can also influence the water mass exchange

between the Arctic Ocean and the sub-Arctic seas. The sea level difference between the Arctic Ocean and the sub-Arctic seas has significant impact on the transport variability through the Arctic gateways (e.g., *Houssais and Herbaut*, 2011). As the sea level increases significantly in Baffin Bay more than in the Arctic Ocean, the export transport through CAA and Davis Strait is significantly reduced (Table 3.1). The direction of the currents through CAA can even reverse depending on seasons and years (not shown), which brings the passive tracer into the Arctic Ocean. As shown in Figure 3.9c, a notable amount of passive tracer enters the Arctic Ocean via CAA and accumulates in the upper Canadian Basin. Reduced freshwater release through the CAA can also contribute to the freshening in the Canadian Basin (Figure 3.9d), besides the impact of changing circulation inside the Arctic Ocean discussed above. Due to the coarse resolution used in the model, the simulated transport through the Davis Strait in the control run is lower than the canonical value. Considering the role of the along strait sea level gradient in determining the CAA transport (*Houssais and Herbaut*, 2011), we believe that the reduction in the CAA export transport in the water-hosing experiment is a robust feature, although the amplitude of reduction might be even larger if the simulated transport is stronger in the control run. A global simulation with locally refined CAA region shows that the CAA transport can be much better represented.

Table 3.1: Total volume transport (Sv) through the Arctic gateways

	Fram Strait	Barents Sea	Bering Strait	Davis Strait
Control	$-3.7(in\,2.5, out\,6.2)$	3.3	1.0	-0.6
Water-hosing	$-3.7(in\,2.2, out\,5.9)$	3.0	0.8	-0.1

The increase in sea level in the Arctic Ocean also leads to reduction in both the Barents Sea and Bering Sea inflow (Table 3.1). The net transport through Fram Strait does not change significantly, but both the inflow and outflow decreases by 0.3 Sv. The reduced AW inflow explains the strong negative salinity anomaly in the Eurasian Basin as discussed above. The

reduction in Pacific freshwater inflow explains the freshening of the northern North Pacific (Figure 3.7b). Although the AW becomes fresher due to added GrIS melt water, thus increasing the total freshwater content in the Arctic Ocean, the increasing rate declines with time due to the weakening of the AW inflow (Figure 3.12).

3.4.4 The impact on AMOC

The simulated temporal evolution of AMOC index at 45 °N for both the control run and the water-hosing experiment is shown in Figure 3.13. The strength of the simulated AMOC in the GrIS melting scenario drops significantly in comparison with the control run. The mean AMOC index in the last cycle is about 10 Sv in the water-hosing run, 4 Sv lower than in the control run. Correspondingly, the Gulf Stream becomes weaker (Figure 3.8) and a local DSL rise is formed northeast the North America (Figure 3.6). Previous water-hosing experiments using the 0.1 Sv melting scenario with coupled climate models (*Stouffer et al.*, 2006) generally show AMOC weakening, but with a large spread in the reduction amplitude (1.5-9Sv). The spread could be due to the uncertainties in simulating different feedbacks from the atmosphere in climate models. In our ocean, alone simulation the applied SSS restoring will certainly weaken the effect of added freshwater from GrIS and prevent us from quantifying the precise response of AMOC strength, although the simulated response is inside the uncertainty spread of climate models.

Here, more attention is paid to the impact of GrIS freshwater on the variability of AMOC. The spectral analysis is applied to the time series of AMOC and shown in Figure 3.14. The spectral analysis reveals a decadal time scale of about 20-year period significant at 95% level in the control run, which was also suggested by other studies (*Bentsen et al.*, 2004; *Hu et al.*, 2004). The nature variability of AMOC on decadal time scale is dominated by a basin-scale adjustment to changes in the deep water convection sites in North Atlantic (*Delworth et al.*, 1993; *Bentsen et al.*, 2004; *Mignot and Frankignoul*, 2005). The significance of the 20-year period is clearly reduced

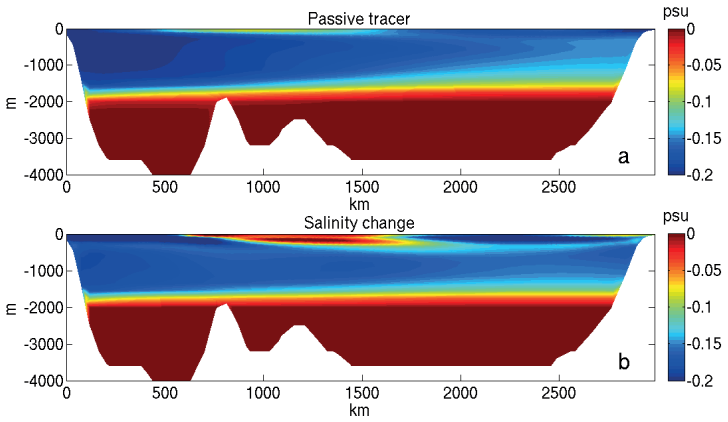

Figure 3.10: Vertical transect of a) passive tracer (practical salinity unit) and b) salinity anomaly (practical salinity unit) averaged over the last ten model years. The location of the transect is shown in Figure 3.9a.

in the water-hosing run. This implies that the added freshwater from GrIS melting has potential impact not only on the strength of AMOC but also on the strength of its variability. The high-frequency variability (on interannual scale) does not change significantly, as its controlling factor, wind forcing, remains the same in our simulations (*Jayne and Marotzke*, 2001; *Shaffrey and Sutton*, 2004; *Dong et al.*, 2009).

As discussed in Section 3.3, the variability of AMOC, especially on decadal time scales, is linked to that of DWBC transport and deep convection (Figure 3.2). Figures 3.15a, b show the spectra of DWBC transport at 53 °N in the control and water-hosing runs, respectively. In the control run, the most pronounced period is 20-year, consistent with that of the AMOC. This variability on decadal time scales almost collapses in the water-hosing run, which can explain the loss of significance in AMOC decadal variability.

In the calculation of DWBC transport we used the same definition ($\sigma_\theta >$ 27.74 kg m $^{-3}$) for both experiments. With this definition, both the DWBC transport magnitude and the strength of its variability are significantly reduced in the water-hosing experiment. We also calculated the volume transport below a fixed depth (1000 m), and the significance of the variability turns out to be much higher than in Figure 3.15b, which can better explain the

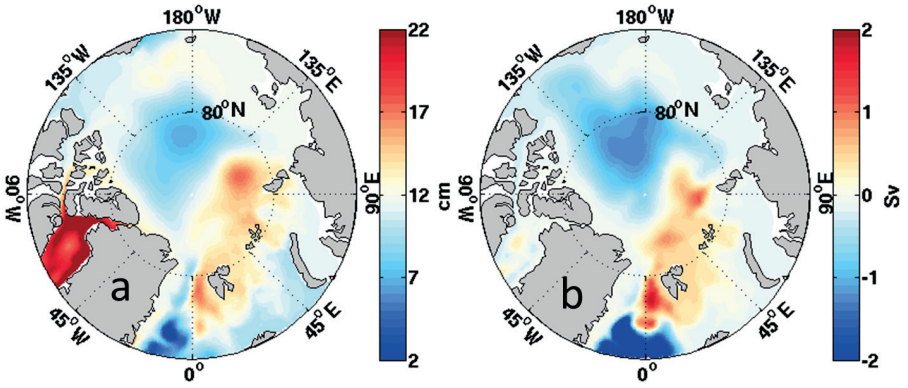

Figure 3.11: a) Dynamic sea level anomaly (centimeter) and b) barotropic streamfunction anomaly (sverdrup) averaged over the last ten model years.

(weakened but not fully collapsed) 20-years variability in AMOC as shown in Figure 3.14b. This suggests that the definition of DWBC should be chosen according to the simulated scenario to study the variability of the Atlantic circulation and its predictability.

3.5 Discussion and conclusions

In this chapter, we evaluated FESOM on large time scales in a global configuration using the CORE interannual forcing. The focus is on the AMOC and the Arctic Ocean. The simulated AMOC strength and streamfunction structure agree with observational estimates and previous model simulations. The good correlation between the MLD in Labrador Sea, the DWBC transport at 53 °N and the AMOC index at 45 °N indicates that the DWBC represents a signal of primarily thermohaline origin and it sets the variability of the AMOC downstream (e.g., *Böning et al.*, 2006). The MLD in the Labrador Sea leads the AMOC at 45 °N by about 2 years in our simulation, consistent to previous studies (e.g., *Eden and Greatbatch*, 2003).

The model successfully reproduces the summer and winter sea ice concentration in the Arctic Ocean. The most pronounced bias from observation is in the marginal seas in summertime, with overestimated sea ice concentration. The simulated liquid freshwater content in the Arctic Ocean has an

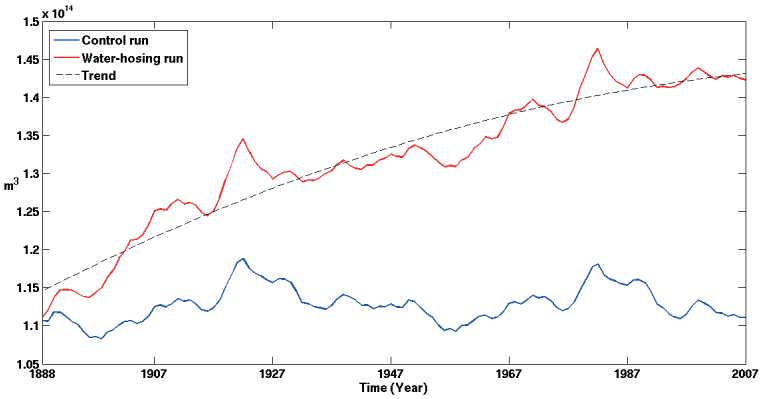

Figure 3.12: Time series of total liquid freshwater content (cubic meter) in the Arctic Ocean for the control (blue) and water-hosing (red) runs. The dashed line represents a second order polynomial fitting the red line.

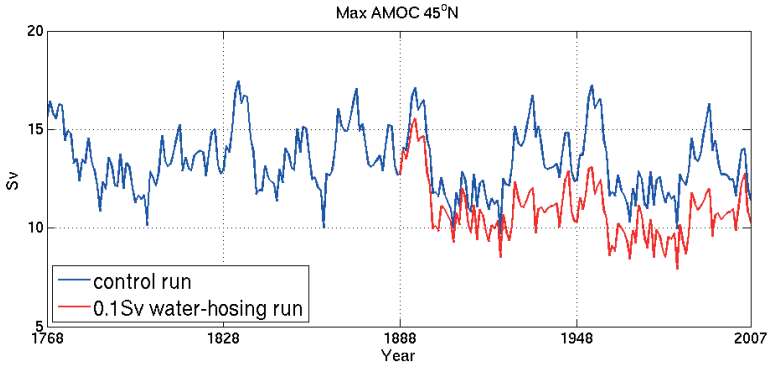

Figure 3.13: AMOC index at 45 °N in the control run (blue) and water-hosing run (red).

increasing trend during the spin-up phase as reported in other models, while its variability (after the model spin-up), controlled mainly by freshwater exchange through the Arctic gateways, is similar to that shown in previous studies (*Häkkinen and Proshutinsky*, 2004; *Köberle and Gerdes*, 2007; *Lique et al.*, 2009).

A water-hosing experiment with 0.1 Sv anomalous freshwater from GrIS melting is conducted to study the direct ocean response. The added freshwater mainly resides in the North Atlantic, Arctic Ocean, and the west South Atlantic after 120 model years simulation. The highest concentration is in

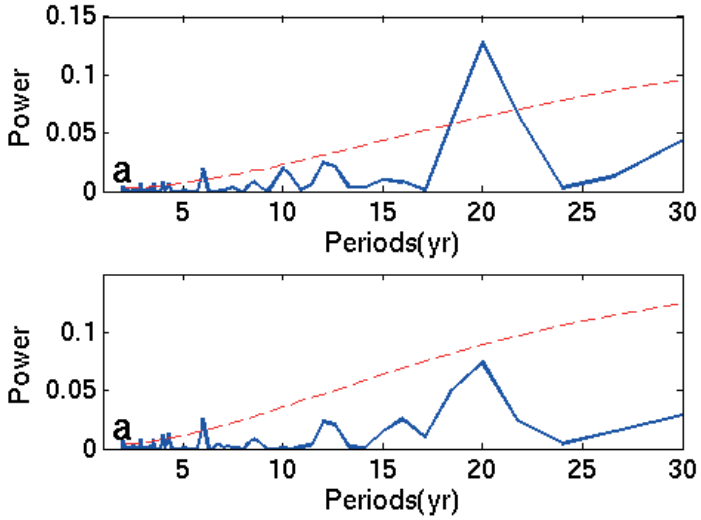

Figure 3.14: Power spectra of AMOC (blue line) in the a control run and b water-hosing run. The red dashed line represents the 95% confidence level.

the North Atlantic subpolar gyre. The ocean salinity decreases accordingly, with a pattern similar to that of the GrIS freshwater distribution. The ocean dynamical adjustment also leads to significant negative salinity anomaly in the eastern North Atlantic, similar to the result from an intermediate complexity climate model (*Gerdes et al.*, 2006).

The DSL anomaly can be carried to the global ocean from the North Atlantic by both wave and advection processes (*Stammer*, 2008). After about 20 years, DSL changes can be observed in all basins. However, the DSL rise is the most significant in the North Atlantic and Arctic Ocean. The largest DSL rise is in the northwest North Atlantic, reaching more than 30 cm after 120 model years, consistent with previous model studies (*Stammer*, 2008; *Yin et al.*, 2009; *Hu et al.*, 2009; *Kopp et al.*, 2010). As in most previous studies, the barotropic signal (e.g., discussed by *Lorbacher et al.*, 2012), which spreads the melt water signal within days around the globe, is ignored in this work by excluding the direct contribution to sea level from the anomalous water mass.

The liquid freshwater content in the Arctic Ocean increases considerably

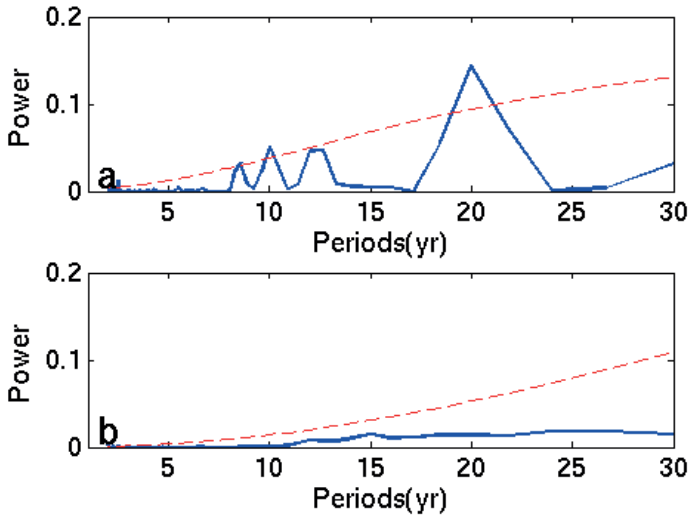

Figure 3.15: Power spectra of DWBC transport (blue line) in the a) control run and b) water-hosing run. The red dashed line represents the 95% confidence level.

with time in the water-hosing experiment. The freshening is obvious in all Arctic basins, with the Eurasian Basin having the largest salinity anomaly. The adjusted ocean circulation leads to changes in surface freshwater distribution. Due to changes in the sea level gradient between the Arctic Ocean and the sub-Arctic seas, the exchange fluxes through all Arctic gates are reduced. On one side, the linkage between the North Pacific and North Atlantic through the Bering Strait and Arctic Ocean is weakened; on another side, the North Atlantic receives much less freshwater from the Arctic Ocean and the North Atlantic water mass can even enter the Canadian Basin through the CAA straits. These changes imply changes in the role of the Arctic Ocean for the global climate, which need to be further explored in the future. The simulated sea ice state does not change noticeably in the water-hosing experiment (not shown), because of missing atmospheric feedbacks.

The anomalous freshwater leads to reduction in both the AMOC strength (*Stouffer et al.*, 2006; *Swingedouw et al.*, 2006; *Gerdes et al.*, 2006; *Hu et al.*, 2009) and the strength of its decadal variability. The decadal variability of the DWBC becomes much weaker in the water-hosing experiment, leading to

significant reduction in the 20-year period oscillation indicated by AMOC. In our experiment, the GrIS freshwater is only added in warm seasons, with the assumption that the ice sheet does not melt in winter even in the global warming scenario. If the same amount of melt water is evenly distributed over the year, the AMOC and its variability is found to be even lower (in a sensitivity experiment, not shown), which is not surprising as the deep convection happens mainly in winter.

Our analysis suggests that care should be taken for using some (commonly used) indices, like DWBC and MLD, in the scenario of increased freshwater forcing. Otherwise, the information can be incomplete. For example, we often define the MLD as the depth where the potential density anomaly referenced to the surface density reaches some chosen value. In this case, the MLD in the Labrador Sea becomes lower at the beginning of the water-hosing experiment compared to the control run and then starts to recover with time. The reason is that the ocean surface becomes fresher at the beginning, reducing the MLD, while the deep ocean also becomes fresher later, recovering the MLD. However, the AMOC in the water-hosing experiment is permanently lower (Figure 3.12), so the change of MLD due to the anomalous freshwater input cannot be used alone as an indicator of AMOC change, although in the control run we can use MLD to explain the variability of AMOC (Figure 3.2).

This work shows that FESOM can reproduce the past ocean variability and well simulate the impact of possible GrIS melting under global warming, despite its unique numerical approach. However, missing atmospheric feedbacks and applying SSS restoring in ocean hindcast simulations can certainly affect the robustness in the representation of variability (*Gerdes et al.*, 2006; *Griffies et al.*, 2009). The large range of responses to identical surface freshwater flux anomalies under different forms of sea surface boundary conditions leads *Gerdes et al.* (2006) to suggest the development of simple atmospheric models to be used in ocean experiments in order to understand the behavior of ocean models. The idea to find solutions for evaluating ocean models with adequate forms of surface boundary conditions but without the full complexity of couple climate models is also proposed by the international

ocean modeling community (e.g., in the COREs project), and we expect that the progress in this direction through international cooperation can help improve and develop ocean models in the future, thus contributing to reduce uncertainties in climate models in the end.

Chapter 4

Influence of resolution on Arctic Ocean and North Atlantic Water inflow simulation

4.1 Introduction

The Arctic Ocean is a semi-closed marginal sea that is connected to large scale oceans through several shallow and/or narrow passages (see Figure 4.1). It is connected to Nordic Seas through Fram Strait, which is relatively narrow and deep (2600 m), and the shallower Barents Sea (200–300 m); to the North Pacific Ocean through the very narrow and shallow Bering Strait (30-50m); to the Baffin Bay by the Canadian Arctic Archipelago (CAA).The Arctic Ocean plays an important role in the global climate system through a number of different physical processes. The air-sea heat, momentum and gas exchange in the Arctic Ocean is largely determined by the sea ice condition. The presence of sea ice strongly influences the absorption and reflection of solar radiation by modifying the planetary albedo. The Arctic Ocean has experienced significant sea ice decline since last decades. The changes in surface albedo associated with melting snow and ice enhanced the warming

in the Arctic (*Holland and Bitz*, 2003; *Serreze and Francis*, 2006; *Serreze et al.*, 2009), and the Arctic amplified warming further impacts on the Earth System (*Bhatt et al.*, 2014). Freshwater storage in the Arctic Ocean also plays an important role in the regional and global ocean circulation and climate. There is a large freshwater input into the Arctic Ocean through river runoff, precipitation and freshwater import from the Pacific (*Serreze and Francis*, 2006; *Dickson et al.*, 2007), so the Arctic Ocean is a large freshwater reservoir. Meanwhile, the excess freshwater is exported to the subpolar North Atlantic via Fram Strait and CAA, which can influence the upper subpolar ocean stratification, further impact the intensity of deep water formation in Greenland, Iceland and labrador Seas and the strength of Atlantic Meridional Overturning Circulation (AMOC) (*Aagaard et al.*, 1985; *Goosse et al.*, 1997; *Häkkinen*, 1999; *Wadley and Bigg*, 2002; *Jungclaus et al.*, 2005).

The warm and saline North Atlantic inflow to the Arctic Ocean is a major component of high northern latitude circulation, which supplies the main inflow of volume, salt and heat to the Arctic Ocean. The processes of how the Atlantic Water(AW) interacts with atmosphere and surrounding water on its way to the Arctic Ocean and how the oceanic heat carried by AW influences the formation and diminish of the Arctic sea ice (*Polyakov et al.*, 2010; *Ivanov et al.*, 2012) still need further studies and discussions in the Arctic climate research community. The AW enters the Arctic Ocean through two passages: the deep Fram Strait and the broad shelf of the Barents Sea. In the latter pathway it enters the Barents Sea through the Bear Island Channel and passes through the Barents Sea into the Kara Sea, and then most of it continues into the Arctic Ocean via the St. Anna Trough. The pathway of AW and its distribution between the two branches will determine the short term fate of its heat (*Lien et al.*, 2013). While the AW through Fram Strait flows along the Arctic continental slope and retains a large part of its heat, the branch flowing through the shallow Barents Sea releases a substantial amount of heat to the atmosphere. Inside the Arctic Ocean the largest changes in AW characteristics occur when it penetrates from one basin into another basin and mixes with the water column present there.

Improved understanding of the Arctic Ocean has been achieved by using

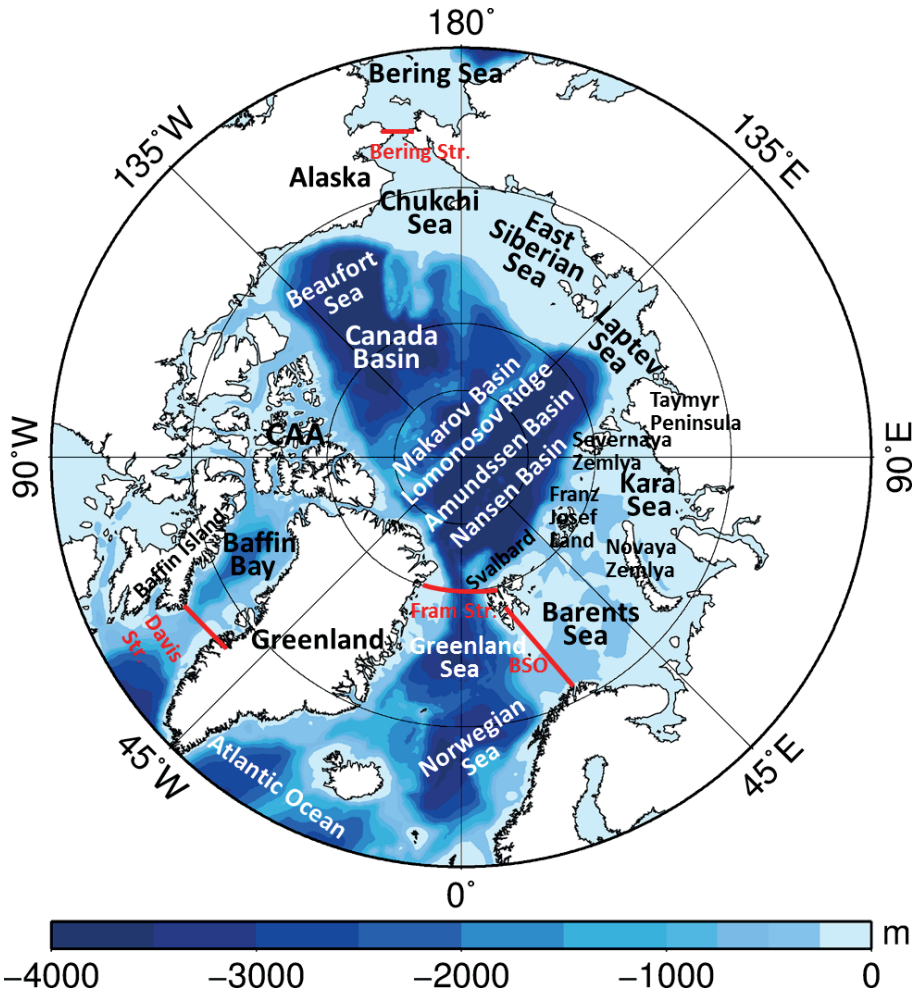

Figure 4.1: Arctic Ocean bottom topography[m]. CAA stands for Canadian Arctic Archipelago and BSO for Barents Opening.

both observations and numerical simulations (see e.g. *Proshutinsky et al.* (2011); *Haine et al.* (2015)).The observing system of the Arctic Ocean has grown quickly in recent years, including satellites, long-term mooring arrays and research vessel expeditions, however, the coverage of available observational data still has large limitation and critical gaps in the Arctic region. Numerical models are essential and efficient tools to represent and understand past conditions, explain observed recent changes, test physical hypothesis and even predict the potential change in the future. As the first baroclinic Rossby radius of deformation in the high-latitude Arctic and sub-

Arctic region is small, ocean models need very high horizontal resolutions to resolve mesoscale eddies and well represent the local dynamics. *Nurser and Bacon* (2014) studied the Rossby radius in the Arctic Ocean and pointed out that the typical annual mean first Rossby radius is about 7-15 km in the deep Arctic Ocean and less than 3 km in shelf seas. Currently it remains computationally expensive to use very high resolution (e.g., less than 10 km) globally in long-term simulations. However, with the variable resolution functionality in FESOM, we can improve the Arctic Ocean simulation in global setups by locally refining the Arctic and sub-Arctic region with horizontal resolution different from other regions.

In this chapter the Arctic Ocean simulated in two FESOM setups with different resolutions will be evaluated. The focus is on Arctic sea ice, freshwater budget and AW inflow.

4.2 Model setup

The unstructured-mesh model, The Finite Element Sea-ice Ocean Model (FESOM,*Danilov et al.* (2004, 2005); *Timmermann et al.* (2009); *Wang et al.* (2008, 2014)) is employed. Figure 4.2 depicts the mesh configurations in two experiments. We use nominal 1.0 ° horizontal resolution in most of the ocean area on both meshes. In the low resolution mesh configuration (LR) shown in Figure 4.2a, north of 50°N including the whole Arctic region, the horizontal resolution is increased to about 24 km. In the high resolution mesh configuration (HR) shown in Figure 4.2b, the Arctic region (including the interior Arctic, CAA, Baffin Bay and Barents Sea) is increased to about 9 km compared to mesh LR. The resolution in HR is comparable to the Arctic mean first Rossby radius, and it is largly an eddy-permitting configuration in terms of the Arctic Ocean.

The Redi diffusion (*Redi*, 1982) and the Gent and McWilliams parameterization (*Gent and Mcwilliams*, 1990) are applied with the critical neutral slope of 0.01. The skew diffusivity is the same as the isopycnal diffusivity, which is parameterized as $V\Delta$, where $V = 0.006$ ms^{-1}, and Δ is the square root of surface triangle area. The horizontal biharmonic viscosity is $B\Delta^3$,

where $B = 0.027$ ms^{-1}. We use the K-Profile Parameterization (KPP) by *Large et al.* (1994) for vertical mixing.

The ocean is initialized with steady velocity and the annual mean potential temperature and salinity climatology of the World Ocean Atlas (*Conkright et al.*, 2002). The sea ice is initialized with mean results from previous simulations. The drag and heat exchange coefficients used in the bulk formula are computed following the suggestion of *Large and Yeager* (2004). The SSS is relaxed toward the monthly climatology with a piston velocity of 50 m/300 day. The total surface restoring flux is normalized to 0 at every time step. The model is forced by the CORE interannual forcing (CORE-II, *Large and Yeager* (2009)) from 1958 to 2007. The first 20 years from 1958 to 1977 is considered as model spin-up and we use the period 1978-2007 for analysis.

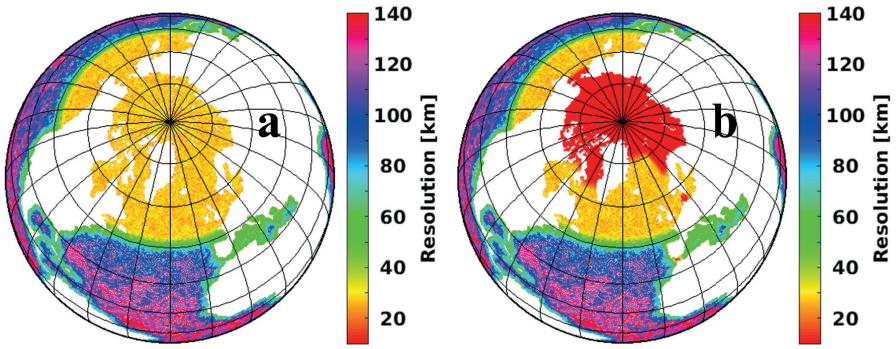

Figure 4.2: Horizontal resolution with local refinement in sub-Arcic and Arctic Ocean a) 24km, b) 9km.

4.3 Results

Based on results on the two meshes with locally different refinement in the Arctic region, the model performance is assessed in this part, focusing on how the resolution influences the simulation of the Arctic Ocean and North Atlantic Water inflow. Sea ice condition, freshwater budget, transport and fluxes through Arctic gateways and the Atlantic inflow are compared and evaluated.

4.3.1 Sea ice extent

Significant decline of Arctic sea ice since satellite observations of sea ice in the 1970s has been detected (*Kwok and Rothrock*, 2009; *Comiso*, 2006; *Comiso et al.*, 2008; *Comiso*, 2012; *Cavalieri and Parkinson*, 2012; *Stroeve et al.*, 2012; *Laxon et al.*, 2013). The decline was particularly dramatic during summer 2007 when Arctic sea ice extent reached a minimum record. As sea ice is one of the important components in the Arctic climate system, its adequate representation in model simulations is essential. The assessment of model performance in sea ice simulations is one of the first necessary steps to help modellers to understand the uncertainty and sea ice related physical processes in simulations and further to improve both model numerics and physics.

The modelled Northern Hemisphere (NH) sea ice extent for September and March during the period 1979-2007 is shown in Figure 4.3 together with the NSIDC observation (*Fetterer et al.*, 2002). In both September and March, the simulated NH sea ice extent from LR (24km) and HR (9km) FESOM runs are both overestimated, compared with the NSIDC observation. However, increasing resolution from 24 km to 9 km reduced the model bias slightly. For the period 1979-2007, the mean September and March NH sea ice extent for NSIDC observation are $6.74 \times 10^6\, km^2$ and $15.58 \times 10^6\, km^2$, respectively, while those for LR are $7.79 \times 10^6\, km^2$ and $16.51 \times 10^6\, km^2$, and for HR are $7.49 \times 10^6\, km^2$ and $16.18 \times 10^6\, km^2$. More statistics results for NH sea ice extent from observation and model simulations during the period 1979-2007 can be seen in Table 4.1. We also did same statistical analysis for the period 1979-2003, in order to compare our model results with those from the OGCMs participating in the CORE-II Arctic comparison project (*Wang et al.*, 2016a). The time series and statistics for the simulated NH sea ice extent in CORE-II models are shown in Figure A.1 and Table A.1 in the appendix A.[1]

The CORE-II intercomparison results together with observations serve

[1]The horizontal resolution in the Arctic Ocean among the 14 CORE-II models are different. GFDL-UNSW-MOM0.25 has about 12 km , Kiel-ORCA05 and AWI-FESOM have about 24 km, and the other models have about 48 km.

Table 4.1: Simulated Northern Hemisphere (NH) sea ice extent: mean, standard deviation (STD), linear trend, correlation with observation (Obs.), and the 2007 value for periods 1979-2007 and 1979-2003

	September			March		
	Obs.	Low-24km	high-9km	Obs.	Low-24km	High-9km
mean79-07	6.74	7.79	7.49	15.58	16.51	16.18
STD79-07	0.79	0.80	0.85	0.48	0.45	0.39
trend79-07	-7.2	-5.6	-6.1	-4.7	-4.1	-3.3
correlation79-07		0.78	0.78		0.76	0.82
mean79-03	6.95	7.95	7.67	15.72	16.64	16.29
STD79-03	0.58	0.70	0.76	0.34	0.31	0.28
trend79-03	-5.3	-4.1	-4.4	-3.4	-2.7	-2.2
correlation79-03		0.76	0.77		0.65	0.76
2007 ice extent	4.30	5.90	5.59	14.65	15.85	15.63

Sea ice extent is in 10^6 km^2, and the trend is in 10^4 km^2/year

as a reference for us to evaluate our simulations. For the period 1979-2003, the observed mean September NH sea ice extent is $6.95 \times 10^6\, km^2$, while the results range from $2.14 \times 10^6\, km^2$ (CMCC-ORCA1) to $8.18 \times 10^6\, km^2$ (AWI-FESOM) among the CORE-II models. The largest difference between models for September sea ice extent is larger than $6 \times 10^6\, km^2$, comparable with the observed mean value, indicating that summer sea ice simulation is still a challenge in some of the ocean climate models. The values for our LR and HR simulations are $7.95 \times 10^6\, km^2$ and $7.67 \times 10^6\, km^2$, respectively, overestimated like in some of the CORE-II models: AWI-FESOM ($8.18 \times 10^6\, km^2$), CERFACS-ORCA1 ($8.12 \times 10^6\, km^2$), Kiel-ORCA05 ($7.85 \times 10^6\, km^2$), NOC-ORCA1 ($7.76 \times 10^6\, km^2$) and MRI-F ($7.65 \times 10^6\, km^2$). Note that significant underestimations for mean September NH sea ice extent are found in some of the CORE-II models: CMCC-ORCA1 ($2.14 \times 10^6\, km^2$), NCAR-POP2 ($3.99 \times 10^6\, km^2$) and FSU-HYCOM($4.00 \times 10^6\, km^2$).

Mean March NH sea ice extent during 1979-2003 from NSIDC is $15.72 \times 10^6\, km^2$, while the CORE-II results vary from $14.43 \times 10^6\, km^2$ (MRI-A) to $16.60 \times 10^6\, km^2$ (FSU-HYCOM). The models spread for winter sea ice extent is less than $1 \times 10^6\, km^2$, much smaller than that for summer. The growth of NH sea ice extent in winter, reaching maximum in March, is almost confined by the continents around the Arctic Ocean. This can partly explain the smaller model spread in March than in September. Our LR run has about $16.64 \times 10^6\, km^2$ for March NH sea ice extent, while the HR result decreases to $16.29 \times 10^6\, km^2$, becoming slightly closer to the observation.

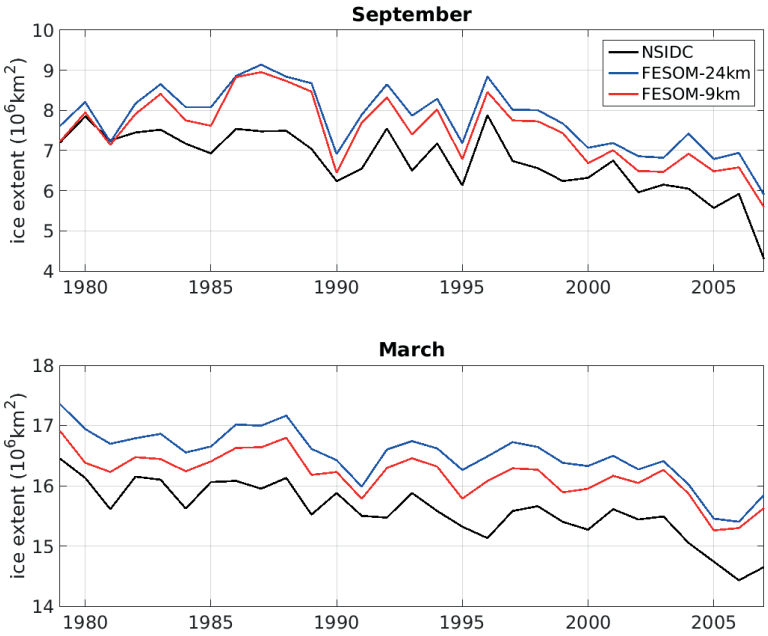

Figure 4.3: Simulated Northern Heimsphere sea ice extent vs that from the NSIDC data set.

Figure 4.3 shows that the simulated interannual variability and descending trend for NH sea ice extent in September and March is similar to the NSIDC observation for both the LR and HR runs. The correlation between the observed and modeled NH sea ice extent is moderately high for both September and March, larger than 0.65 (see Table 4.1). The NH sea ice extent has stronger variability (defined by STD) and descending trend in

September than in March, which is shown by both the observation and model simulations (Table 4.1).

In September, the HR run reduced the overestimation of mean sea ice state and underestimation of sea ice descending trend compared to the LR run. However, the overestimated interannual variability becomes slightly larger in HR. This is consistent with the conclusion from the CORE-II model intercomparison, that the models with lower sea ice extent in September tend to have stronger interannual variability. In March, the HR run improved the mean sea ice state, but not the sea ice interannual variability and descending trend. The interannual variability and descending trend of sea ice extent in March are underestimated in both LR and HR runs, which is a common model behavior as shown by 13 CORE-II models (*Wang et al.*, 2016a).

The modelled mean horizontal distribution of sea ice concentration (only larger than 15% is shown) in September and March is compared to the NSIDC observation in Figure 4.4. We did the average for the period 1988-2007 as the NSIDC satellite data has the same horizontal coverage in terms of the North Pole region since 1988. Generally, both the LR and HR runs can reproduce sea ice distribution pattern comparable with the observation. In September, both runs overestimate the ocean area with sea ice concentration larger than 15% (threshold for calculating sea ice extent), which explains the overestimation of FESOM for sea ice extent discussed above. The overestimation is mainly located in the marginal seas along the Eurasian continent shelves and in the southern CAA region. The HR run reduced the sea ice extent in Kara and Barents Seas compared to the LR run. We also notice that the simulated sea ice concentration toward the Siberian coast is lower than the observed. In March, the simulated sea ice concentration patterns in both runs show very good agreement with the NSIDC observation.

Arctic sea ice extent in September has declined over the course of the satellite measurement since 1979, with a pronounced sea ice extent minumum observed in September 2007 (*Stroeve et al.*, 2008). The spatial distribution of sea ice concentration in September 2007 for the NSIDC observation and FESOM simulations is shown in Figure 4.5. The observed sea ice retreated dramatically towards the North Pole from the Siberian side, and the marginal

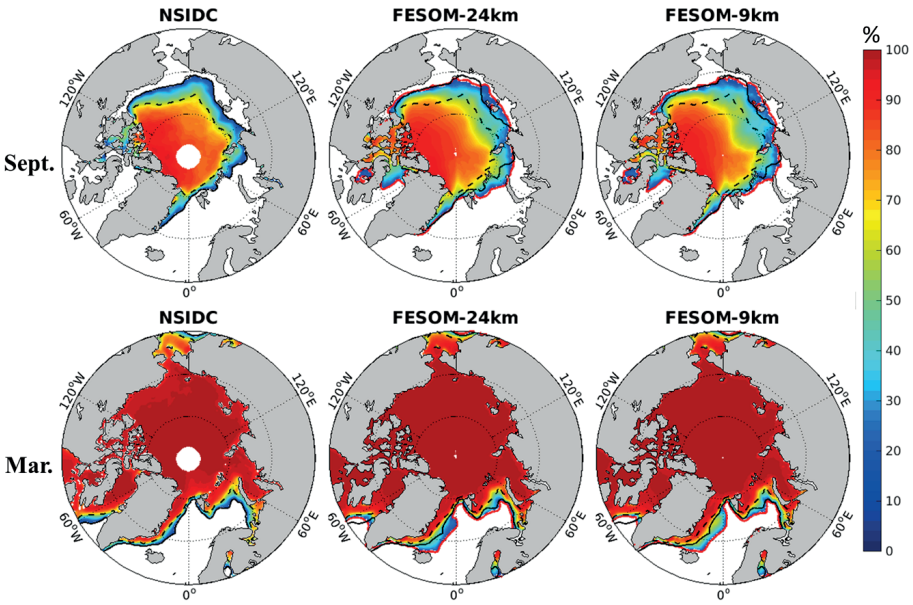

Figure 4.4: Observed and simulated mean sea ice concentration for September and March for period 1988-2007 (only ice concentration larger than 15% is plotted here). The black solid and dashed lines are for NSIDC 15% and 60% ice concentration contours respectively; the red solid line is for simulated 15% ice concentration contour.

seas and deep basin on the Siberian side in the Arctic Ocean are almost ice free. Both runs reproduced the observed sea ice pattern, but the decline of sea ice is weaker. The simulated sea ice concentration for September 2007 in the CORE-II models (*Wang et al.*, 2016a) differs largely from model to model (see Figure A.2 of the appendix A). NCAR-POP2, CNRM-ORCA1, CMCC-ORCA1, FSU-HYCOM and Bergen-MICOM largely underestimate sea ice extent in September 2007, and these five models have sea ice only along the northern boundary of the CAA, leaving the other part of the Arctic Ocean ice free. The other nine models reproduced the sea ice retreat towards the North Pole from the Siberian side, but similar to our runs, underestimated the dramatic sea ice decline. However, the simulated sea ice concentration patterns between these nine models are significant different. GFDL-UNSW-MOM0.25, NOC-ORCA1 and MRI-A simulated higher sea ice concentration for sea ice covered area compared to the observation, while

AWI-FESOM, GFDL-MOM, MRI-F and GFDL-GOLD simulated lower sea ice concentration in the eastern Eurasian Basin, as in our runs.

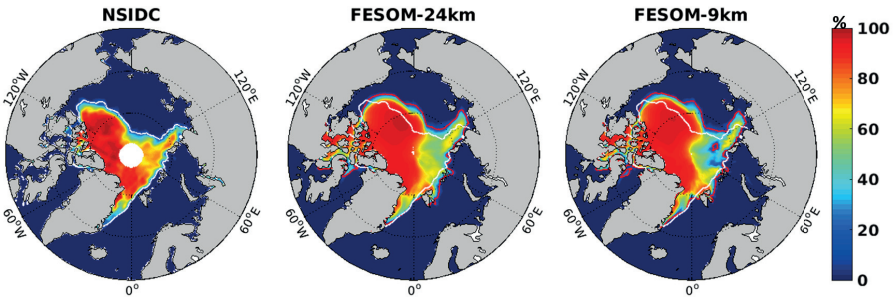

Figure 4.5: Observed and simulated sea ice concentration for September 2007. The NSIDC 15% ice concentration contour line is shown in white and the simulated 15% ice concentration contour line is shown in red.

4.3.2 Freshwater budget

The Arctic Ocean is an important reservoir and pathway for freshwater: 11% of the global continental runoff flows directly into the Arctic Ocean (*Fichot et al.*, 2013). Additional freshwater enters the Arctic Ocean from the Pacific through Bering Strait (*Woodgate and Aagaard*, 2005; *Woodgate et al.*, 2006, 2012), and from net precipation. The freshwater exists in the Arctic Ocean in two forms: the solid freshwater in form of sea ice and the liquid form stored in the upper ocean. The freshwater in the Arctic Ocean can be transformed between this two forms by melting and forming sea ice. The excessive freshwater is mainly exported from the Arctic Ocean through Fram and Davis Straits to the North Atlantic (*Kwok and Rothrock*, 1999; *Kwok et al.*, 2004; *Kwok*, 2009; *Rabe et al.*, 2009, 2013), where it has the potential to affect deep convection (*Häkkinen*, 2002; *Koenigk et al.*, 2007; *Rennermalm et al.*, 2007) and the large scale ocean circulation (*Häkkinen*, 1999; *Wadley and Bigg*, 2002; *Brauch and Gerdes*, 2005; *Jungclaus et al.*, 2005).

The total solid freshwater content (FWC) in the Arctic Ocean is determined by total sea ice volume. Many studies have shown that sea ice volume in the Arctic Ocean continues to decline together with the retreat of both

sea ice extent and thickness since satellite observation started (*Kwok and Rothrock*, 2009; *Cavalieri and Parkinson*, 2012; *Comiso*, 2012; *Stroeve et al.*, 2012; *Laxon et al.*, 2013). The simulated sea ice extent and concentration have been discussed above. The simulated sea ice thickness pattern together with that derived from ICESat measurements is shown in Figure 4.6. ICESat (Ice, Cloud, and land Elevation Satellite) is the benchmark Earth Observing System mission for measuring, among other earth surface parameters, sea ice surface elevation. The sea ice thickness field derived from ICESat measurements are limited in space and time and available for a few months in spring and fall each year starting from 2003 (*Kwok*, 2009). We will shown the comparison for the mean sea ice thickness for spring (Feb., Mar. and April) during 2004-2007 for our simulations.

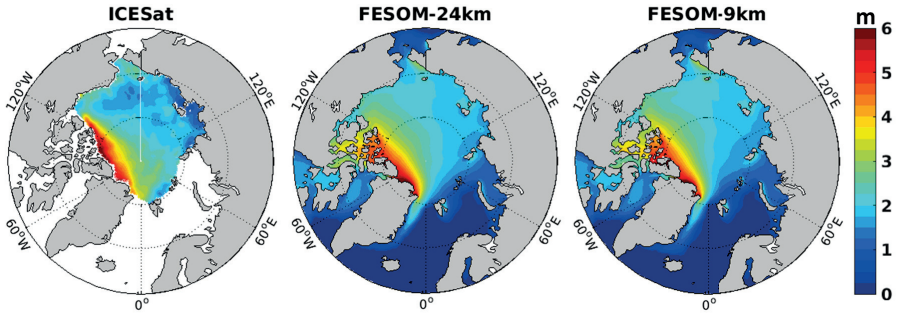

Figure 4.6: Observed and simulated spring sea ice thickness [m]. The observation is averaged over all available ICEsat sea ice thickness data in spring 2004-2007 (*Kwok and Rothrock*, 2009) and the model results are the mean value for spring (Feb., Mar. and April) 2004-2007.

The observed sea ice thickness increases from about 1 m at the Siberian coast to more than 5 m at the northern CAA. Both the FESOM-24km and FESOM-9km runs simulated this pattern very well, including the magnitude of the sea ice thickness. All models in the CORE-II intercomparison project (*Wang et al.*, 2016a) can reproduce the observed sptial distribution pattern (see Figure A.3 in the appendix A), but most of them failed in simulating the observed magnitude of the sea ice thickness except for AWI-FESOM and Kiel-ORCA1. The ICESat observation shows that the sea ice thickness at the Siberian coast is about 1 m, which is overestimated by both the FESOM-

24km and FESOM-9km setups. Sea ice concentration is overestimated in September towards the Siberian coast (Figure 4.4). Overestimated spring sea ice thickness could lead to too high sea ice concentration (extent) in summer as heat in the melting season may not be enough to melt too thick ice.

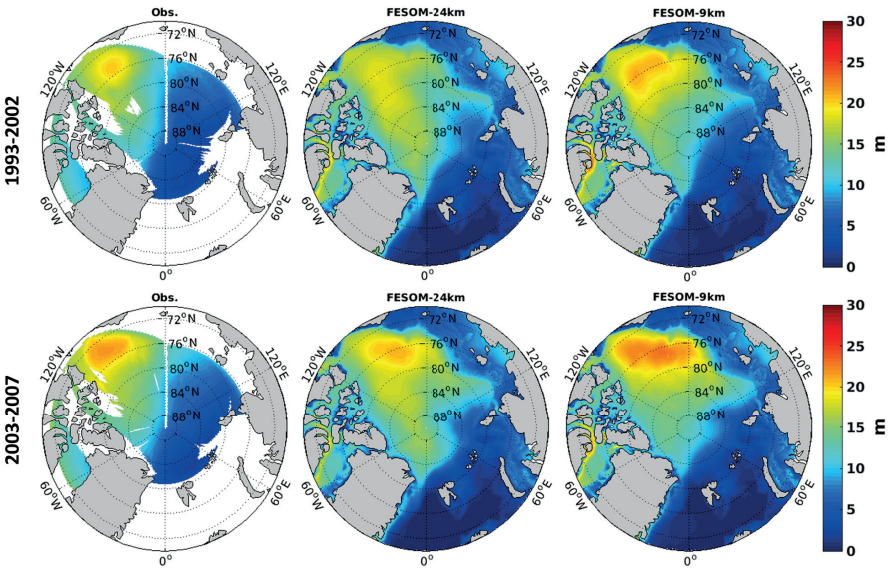

Figure 4.7: Freshwater content averaged for 1993-2002 (top) and 2003-2007 (bottom) from observation and FESOM simulations. The reference salinity is 34.8 and the integration in the vertical is taken until the reference salinity depth.

The liquid freshwater is stored in the upper Arctic Ocean. It forms a strong vertical stratification and isolates the surface layer from the salty, warm Atlantic Water (*Rudels et al.*, 2004), which limits the upward transfer of heat and thus influences the formation and melting of sea ice. Therefore it is an important component of the Arctic climate system. The liquid FWC simulated in our FESOM runs is evaluated here by comparison to observations. Figure 4.7 shows the 2D FWC distribution (in meter, vertically integrated at each horizontal grid as $\int_H^0 \frac{S_{ref}-S}{S_{ref}} dz$, where S is salinity, $S_{ref} = 34.8$ is the reference salinity, z is water depth, H is the ocean depth where S reaches S_{ref}) averaged for 1993-2002 and 2003-2007 from observa-

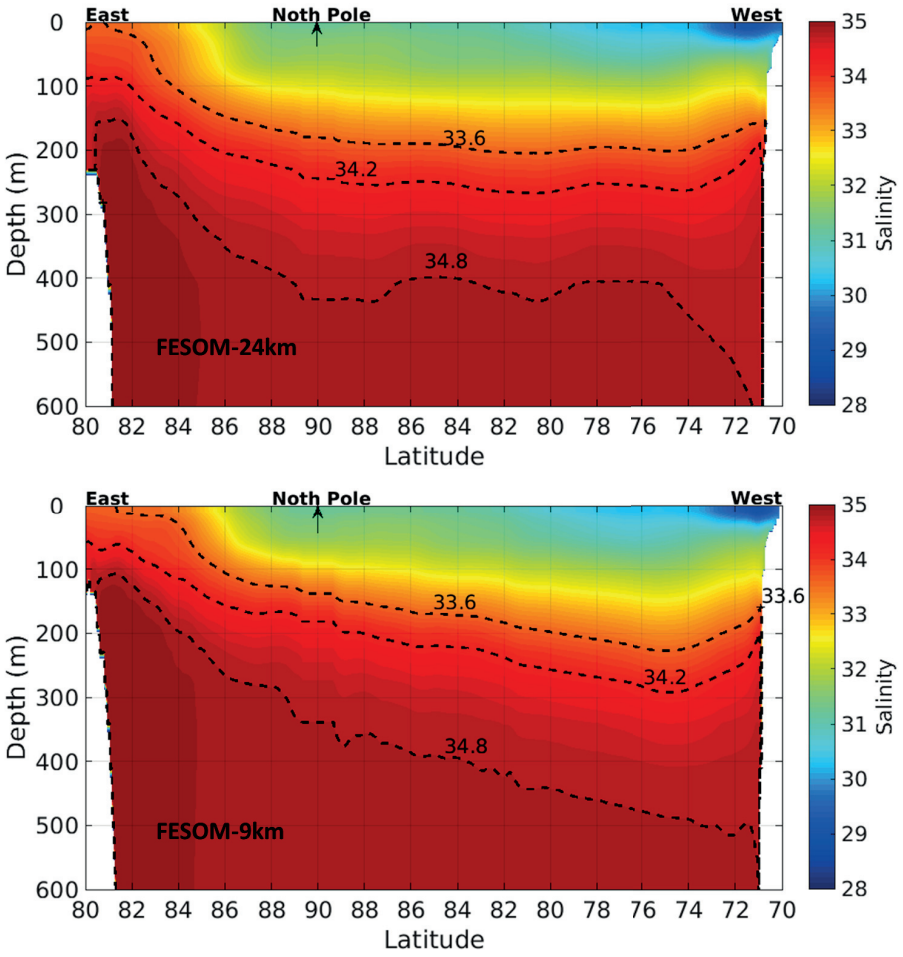

Figure 4.8: Vertical salinity section along the 30 °E and 150 °W longitude crossing the North Pole, averaged over the period of 1993–2007.

tion and model runs. The period 1993 to 2007 is chosen to evaluate the FWC motived by the availability of observations during this period (*Rabe et al.*, 2014). We did the average for two periods, as we want to compare directly with the CORE-II models (*Wang et al.*, 2016b).

The observation shows two distinct regions in the horizontal liquid FWC pattern: higher liquid FWC in the Canadian Basin and much lower in the Eurasian Basin. The highest liquid FWC is located in the Beaufort Gyre. Previous studies have shown that high liquid FWC in the Beaufort Gyre is the consequence of Ekman pumping associated with strong anticyclonic Beaufort High (*Proshutinsky et al.*, 2002, 2009; *Rabe et al.*, 2014). In the Canadian Basin, FESOM-24km underestimated the strength of liquid FWC in the central Beaufort Gyre, but overestimated the liquid FWC in other part of the Canadian Basin. FESOM-9m improved the simulation in the Canadian Basin by increasing the magnitude of the liquid FWC and reducing the overestimation tongue expanding towards the Lomonosov Ridge. In the Eurasian Basin, both FESOM-24km and FESOM-9km show overestimation of liquid FWC, however, FESOM-9km slightly decreased the bias in some part of Amundsen and Nansen Basins.

In the CORE-II models (see Figure A.4 in the appendix A), most of them tend to overestimate the liquid FWC in both the Canadian and Eurasian Basins (*Wang et al.*, 2016b). The CORE-II results also indicate that sea surface salinity restoring leads to overestimated liquid FWC. Our results show that the details of the simulated FWC can also be influenced by the mesh resolution. The Arctic liquid FWC has increased in recent years as shown by the observation. Both the FESOM-24km and FESOM-9km runs simulated increasing trend when we compare the two periods. The increase of liquid FWC in the Arctic Ocean is also captured by most of the CORE-II models (*Wang et al.*, 2016b).

To further understand the difference of simulated liquid FWC in the Arctic Ocean between the FESOM-24km and FESOM-9km runs, the mean vertical salinity structure along the longitude direction 30 °E and 150 °W crossing the North Pole from these two runs are shown in Figure 4.8. The freshwater is located shallower in the Eurasian Basin and deeper in the Canadian Basin,

which is consistent with the liquid FWC distribution. FESOM-9km simulated steeper east-west haline slope than FESOM-24km, which explains more realistic liquid FWC gradient from the Eurasian Basin towards the Canadian Basin in FESOM-9km. In the Canadian Basin, no obvious haline slope in FESOM-24km was captured, which leads to the uniform zonal distribution of liquid FWC in FESOM-24km shown in Figure 4.7. The Beaufort Gyre is maintained by high sea level pressure and the anticyclonic wind (*Proshutinsky et al.*, 2002). Due to oceanic Ekman convergence and subsequent downwelling associated with strong anticyclonic circulation, the freshwater can be stored at deeper depth, leading to highest FWC in the Beaufort Gyre. In the section shown in Figure 4.8, the haline of FESOM-9km shows a significant deepening between 73 °N and 75 °N, where the Beaufort Gyre is centred. This feature is not well simulated in FESOM-24km, which explains the too weak Beaufort Gyre FWC in this simulation.

4.3.3 Fluxes through Arctic gateways

The Arctic Ocean is connected to the global ocean by exchanging water mass, heat and freshwater with the Atlantic and Pacific Oceans through several main oceanic gateways. On the Atlantic Ocean side it has three gateways, Fram Strait, the Barents Sea Opening (BSO) and Davis Strait. On the Pacific Ocean side Bering Strait is the only ocean gateway. The fluxes through these Arctic gateways will be discussed in this section. Table 4.2 shows the mean state of total ocean volume, heat and liquid freshwater transports from the model simulations and observations. The model results are averaged in the same periods as those for observations. When we compare the model results with the observational estimates, we should keep in mind that there are uncertainties in observations because of the spatial sparseness of observation instruments.

The canonical states of ocean volume, freshwater and heat fluxes through the Arctic gateways are reproduced in both simulations. The Arctic Ocean receives oceanic inflow through BSO and Bering Strait, and releases the water mass to the North Atlantic through Fram and Davis Straits. It exports its

Table 4.2: Observed and simulated fluxes through the Arctic gateways. Values are positive for Arctic inflow. For each flux, the upper row shows model results (left for FESOM-24km and right for FESOM-9km) and the lower row shows the observation.

	Fram Strait		Barents Sea Opening		Davis Strait		Bering Strait	
Volume	-2.60	-2.46	2.59	2.84	-1.1/-0.8	-1.4/-1.1	0.87	0.94
Transport	-2.0 ± 2.7[1]		$2.0 \sim 2.6$[5,6,7]		-2.6 ± 1.0[8](1987-1990)		0.8 ± 0.2[10,11,12]	
(Sv)	(1997-2007)		(1997-2007)		-2.3 ± 0.7[9](2004-2005)		(1990-2007)	
Heat	21	25	72	77	11/15	12/18	9.7	10.2
Transport	36 ± 6[2,**]		50[5,6,*] ~ 70[5,**]		18 ± 17[8,*](1987-1990)		$10 \sim 20$[11,***]	
(TW)	(1997-2009)		(1997-2007)		20 ± 9[9,*](2004-2005)		(1998-2007)	
Freshwater	-74	-70	-2.0	-1.8	-70/-56	-82/-76	62	67
Transport	$-80 \sim -66$[3,4]		-5.7[5]		-92 ± 34[8,*](1987-1990)		80 ± 20[11]	
(mSv)	(1997-2008)		(1997-2007)		-116 ± 41[9,*](2004-2005)		(1999-2005)	

[1] *Schauer et al.* 2008, [2] *Schauer and Beszczynska-Möller* 2009, [3] *de Steur et al.* 2009, [4] *Rabe et al.* 2009, [5] *Smedsrud et al.* 2010, [6] *Skagseth et al.* 2008,[7] *Skagseth et al.* 2011, [8] *Cuny et al.* 2005, [9] *Curry et al.* 2011, [10] *Roach et al.* 1995, [11] *Woodgate et al.* 2010, [12] *Woodgate et al.* 2006.

*Heat flux calculated with reference temperature $-0.1°C$

**Heat flux for closed volume budget(reference temperature $0°C$)

***Heat flux reference to freezing temperature

excessive freshwater through the latter two straits. Because the Atlantic inflow through the BSO has higher salinity than the mean Arctic salinity, the BSO is also a sink of Arctic freshwater. Both the Pacific and Atlantic Oceans supply oceanic heat to the cold Arctic Ocean.

There are very large uncertainties for the observational estimate of net water volume export at Fram Strait. Fram Strait is a wide (about 450 km) channel, and the mooring array is relatively coarse and does not cover the whole strait (*Schauer et al.*, 2008; *Beszczynska-Möller et al.*, 2011). The net ocean volume exports at Fram Strait are 2.60 Sv in FESOM-24km and 2.46 Sv in FESOM-9km, reasonable compared with the mean value of about 2.7 Sv suggested by the observation. The freshwater fluxes in the two simulations are also in the range of observed values. Heat fluxes are underestimated in

the two runs, with FESOM-9km having a slightly higher value.

Ocean volume transport in Davis Strait is determined by the strength of transports through the CAA region. *Wekerle* (2013) showed that an increase in local resolution in CAA can enhance the export of volume and freshwater from the Arctic Ocean, which is consistent with our results: FESOM-9km produced stronger volume and freshwater export than FESOM-24km. The underestimation in FESOM-9km indicates that 9 km resolution in CAA is not enough to fully resolve the dynamics of the CAA throughflow. When the outflow through Davis Strait is increased in FESOM-9km, its outflow through Fram Strait is reduced.

At BSO the ocean volume transport is slightly overestimated in the simulations, while the heat flux is very close to the upper bound of the observational estimate. At Bering Strait both FESOM-24km and FESOM-9km have results within the uncertainty range of observations for ocean volume, heat and freshwater transports. Although FESOM-9km tends to simulate slightly stronger transports than FESOM-24km, the difference is less than the observation uncertainty.

4.3.4 Atlantic Water inflow

Atlantic Water(AW) plays a crucial role in the ocean climate of the Nordic Seas and the Arctic Ocean as it brings heat and salt from the low latitude to the high latitude (*Broecker et al.*, 1991). The pathways and variabilities of AW current in the Nordic Seas are mostly known and investigated via observation and numerical studies (e.g. *Orvik and Niiler* (2002); *Turrell et al.* (2003); *Orvik and Skagseth* (2005); *Holliday et al.* (2008); *Mork and Skagseth* (2010); *Glessmer et al.* (2014); *Chafik et al.* (2015); *Childers et al.* (2015)). After passing the Greenland-Scotland Ridge, most AW continues as Norwegian Atlantic Current(NwAC). The NwAC maintains a two-branch flow of AW through the Norwegian Sea towards the Arctic Ocean and is the major source of oceanic heat and salt to the Arctic Ocean. North of Norway, the eastern branch of the NwAC bifurcates into two streams, the North Cape Current (NCaC) into Barents Sea and the West Spitsbergen Current (WSC)

continuing northward toward the Fram Strait. The western branch flows northwards as a baroclinic, topographically steered jet and converges with the WSC at Fram Strait.

The fate of AW after entering the Arctic Ocean is still not fully understood because of limited hydrography observations. A new study in the framework of the CORE-II project , with focus on the simulations of hydrography in the Arctic Ocean, shows a large spread in simulated temperature and spatial structure of the AW (*Ilicak et al.*, in press). It indicates that current coarse resolution ocean models cannot adequately represent AW inflow and the mid-depth hydrography in the Arctic Ocean.

In this section we will compare the simulated AW at Fram Strait and BSO in the two FESOM setups. We will evaluate whether higher horizontal resolution can improve the model results.

Fram Strait Since the summer 1997 long-term monitoring of hydrography in Fram Strait have been carried out with an array of year-round moorings deployed at the section 78 °50′N by Alfred Wegener Institute (AWI), covering the strait from the shelf west of Svalbard through the deep part to the eastern Greenland shelf (*Beszczynska-Möller et al.*, 2012). The long-term mean temperature and velocity measured and modelled at the Fram Strait section 78 °50′N are presented in Figure 4.9. The North Atlantic Water flows through the strait along the eastern shelf slope as the West Spitsbergen Current(WSC) located over about 850 m depth (*Fahrbach et al.*, 2001; *Schauer et al.*, 2004).

FESOM-9km simulated a strong WSC core as suggested by observed temperature and velocity, while FESOM-24km modelled larger bias for the WSC core in terms of both its location and magnitude. The observed WSC has velocity exceeding $15\,cms^{-1}$ and mean temperature up to 4 °C. The magnitude of the WSC velocity in FESOM-9km is close to the observation, although the simulated vertical spread of the high velocity region is shallower. In FESOM-24km, the maximum WSC velocity is only about $5\,cms^{-1}$, and located too to the west. The temperature field shows that FESOM-24km simulated too strong vertical stretching of the AW layer at Fram Strait. As suggested in

previous studies (e.g., (*Ilicak et al.*, in press)), numerical mixing can explain the deeper penetration of the AW layer. The tendency of deeper penetration is reduced in FESOM-9km, because numerical mixing is reduced with increasing resolution. As the first Rossby radius is less than 4 km at this location, FESOM-9km also does not simulate meso-scale eddies, which play an important role in shedding the warm AW to the west. Therefore, compared to the observation, FESOM-9km did not simulate enough westward spreading of the AW layer.

The complicated topography at the Fram Strait causes the WSC to split into three branches (*Aagaard et al.*, 1987; *Quadfasel et al.*, 1987; *Bourke et al.*, 1988; *Gascard et al.*, 1995; *Schauer et al.*, 2004; *Marnela et al.*, 2013): a fraction directly enters the Arctic Ocean, the second branch follows the western rim of the Yermak Plateau, and the third one recirculates between 78 ° and 80 °N and then flows southward with the East Greenland Current(EGC) as the Return Atlantic Current (RAC). The warmer RAC layer under the cold polar water was investigated by many hydrography surveys, showing that the strength and location of RAC has strong temporal variation. Figure 4.9 shows large difference in the temperature of the RAC between the observation, FESOM-24 and FESOM-9km. As described by *Beszczynska-Möller et al.* (2012), the moorings deployed along the Greenland shelf are sparse and it is not clear how large the observational uncertainty is. Besides, one array of moorings in Fram Strait cannot provide enough information on where the return flow starts to recirculate to the south.

To illustrate the variation of the RAC from the model simulations, snapshots of zonal monthly mean temperature fields at the 200 m depth are shown for FESOM-24km (left) and FESOM-9km (right) in Figure 4.10. The location where the AW strarts to return southwards and the strength of the RAC have strong temporal variation in both simulations. The WSC is stronger in FESOM-9km, and the current reaches more north locations before part of it returns as the RAC. It is expected that further increasing resolution to eddy-resolving could incease the westward AW transport at Fram Strait and then change the location of recirculation to the south. Eddy-resolving simulations will be our future work.

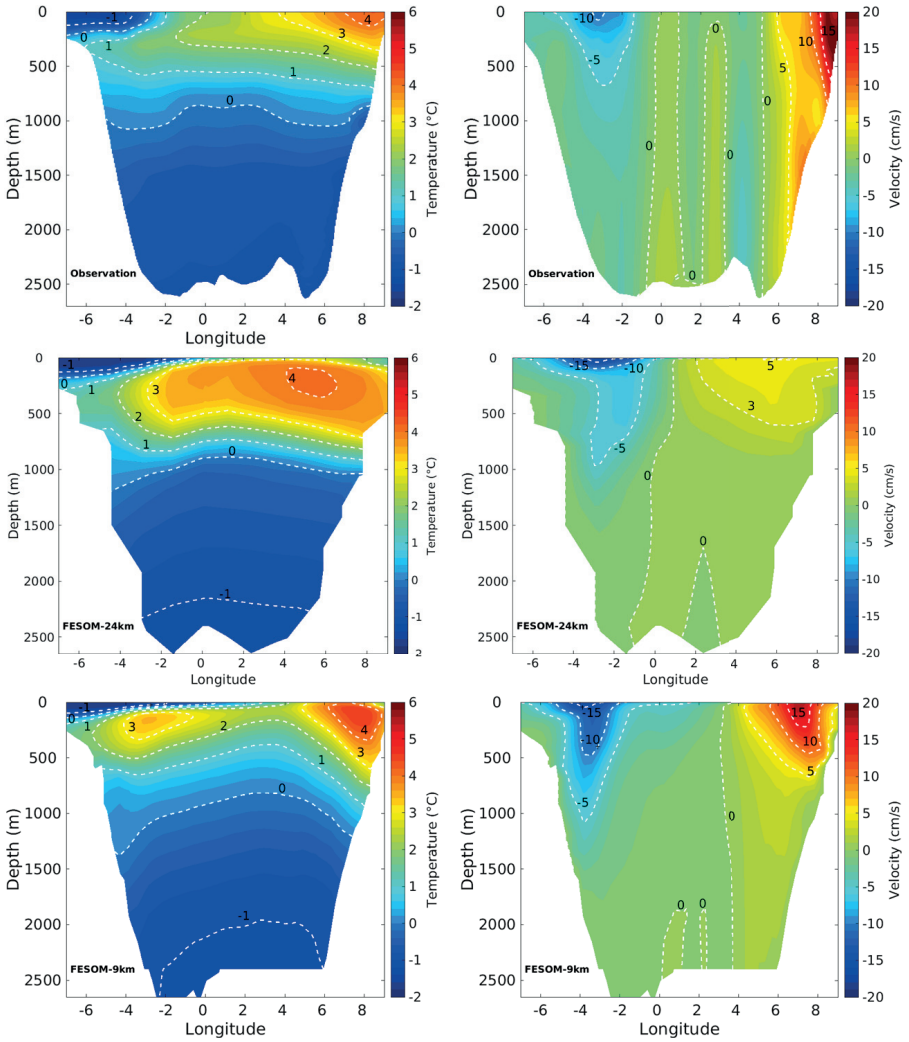

Figure 4.9: Observed and simulated temperature and velocity at the section 78 °50′N in Fram Strait, averaged over 1998–2007.

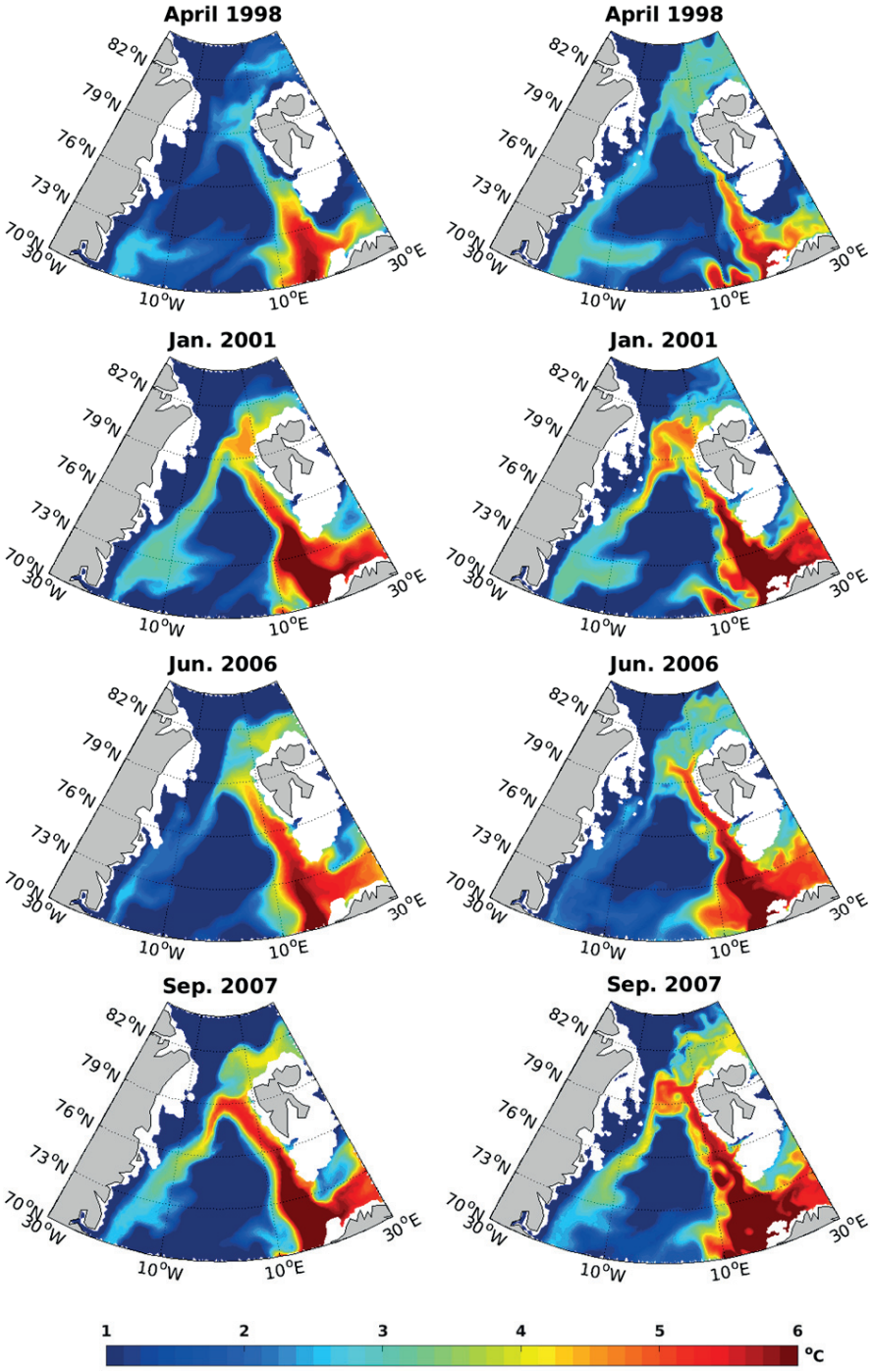

Figure 4.10: Simulated monthly mean temperature at 200 m depth for chosen years and months from FESOM-24km (left) and FESOM-9km (right).

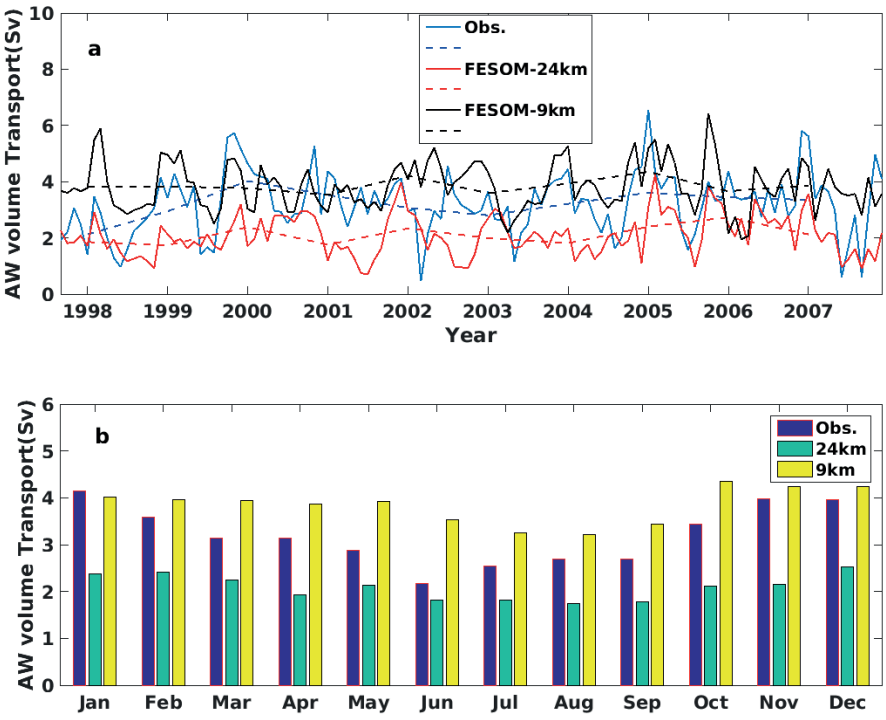

Figure 4.11: (a) Monthly (solid) and winter-centred annual mean (dotted) time series of northward Atlantic Water volume transport carried by the WSC. The volume transport is calculated for the northward current east of 5°E with temperature warmer than 2°C in Fram Strait. (b) The same as (a) but for the seasonal cycle.

The observed and simulated variability of northward volume transport of AW in Fram Strait is shown in Figure 4.11. The observed mean AW inflow transport is 3.2 Sv. The simulated mean AW inflow transports are 2.1 Sv in FESOM-24km and 3.8 Sv in FESOM-9km. Although the high resolution run has mean transport closer to the observation, the two simulations have similar monthly and interannual variability. No significant trend was found according to the annual mean volume transport, which is consistent with the finding by (*Skagseth et al.*, 2008) that no trend was found in the AW volume transport upstream in Norwegian Sea. We also compared the time series of AW transport with that upstream through the Iceland-Scotland Ridge for time period 1978–2007. The correlation coefficients of winter centred annual mean AW transports between these two sections are 0.54 in FESOM-24km and 0.61 in FESOM-9km. This indicates that part of the interannual variability of AW at Fram Strait originates from the upstream basin. The AW inflow has a strong seasonal variability (Figure 4.11a,b). Both the observation and model simulations show high AW volume transport in winter and low transport in summer. However, the magnitude of the mean seasonal cycle is underestimated in both simulations.

Barents Sea Opening The main inflow of AW to the Barents Sea is the east extension of the NwAC as the North Cape Current (NCaC), which carries high temperature and salinity AW. Along the Norwegian Coast, the Norwegian Coastal Current (NCC) brings relatively fresh and warm coastal water into the Barents Sea. Part of the AW in the NCaC can recirculate in Bear Island (BI) Trough. The heat flux associated with the outflow of this recirculation is not negligible and needs to be included in heat budgets analysis for the Barents Sea (*Skagseth*, 2008). The NCC originates mainly from the Baltic Sea, with contributions from the North Sea and runoff from the the Norwegian mainland (*Helland-Hansen and Nansen*, 1909; *Ikeda et al.*, 1989). The inflow of Coastal Water in the NCC has a large impact on the transformation of the AW in the Barents Sea (*Ingvaldsen et al.*, 2004). The density contrast between the low-density coastal and the high-density Atlantic waters determines the strengths of NCaC and NCC(*Helland-Hansen*

and Nansen, 1909; *Ikeda et al.*, 1989; *Ingvaldsen et al.*, 2004).

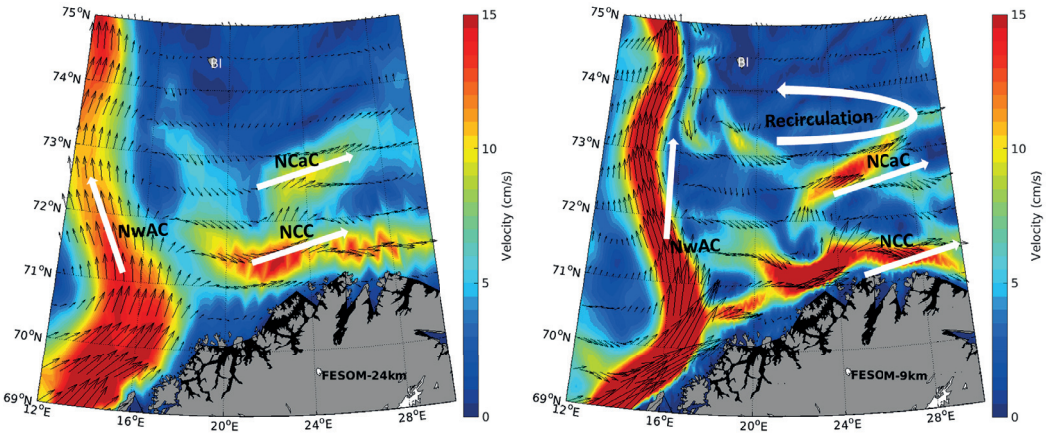

Figure 4.12: Simulated mean horizontal velocity at the 50 m depth in the southern Barents Sea region, averaged over 1997–2007.

Figure 4.12 shows the simulated horizontal velocity at the 50 m depth in the southern Barents Sea. The circulation patterns in both FESOM-24km and FESOM-9km show good agreement with observed general circulation. The NwAC, NCaC and NCC are all captured in the simulations well. Higher resolution tends to simulate stronger and narrower currents. FESOM-9km modelled the NCaC recirculation current in the BI Trough (between 73 °N and 74 °N), while it's weaker in FESOM-24km.

The temperature, salinity and velocity at the 24°E section are shown in Figure 4.13. Both the NCaC and NCC flow eastwards into the Barents Sea, carrying heat from the North Atlantic. The temperature structures simulated in the two runs are very similar as both NCaC and NCC carry similar temperature structure from the North Atlantic. However, the simulated salinity profiles are different in two different resolution runs. The gradient of salinity at the location of NCaC and NCC is sharper in FESOM-9km, associated with stronger and narrower currents.

The simulated interannul and seasonal variabilities of AW volume transport (include NCaC and NCC) in the BSO is shown in Figure 4.14. The two resolution runs show high agreement on both the variability and the magnitude of AW transport. The simulated mean AW volume transports are 2.92

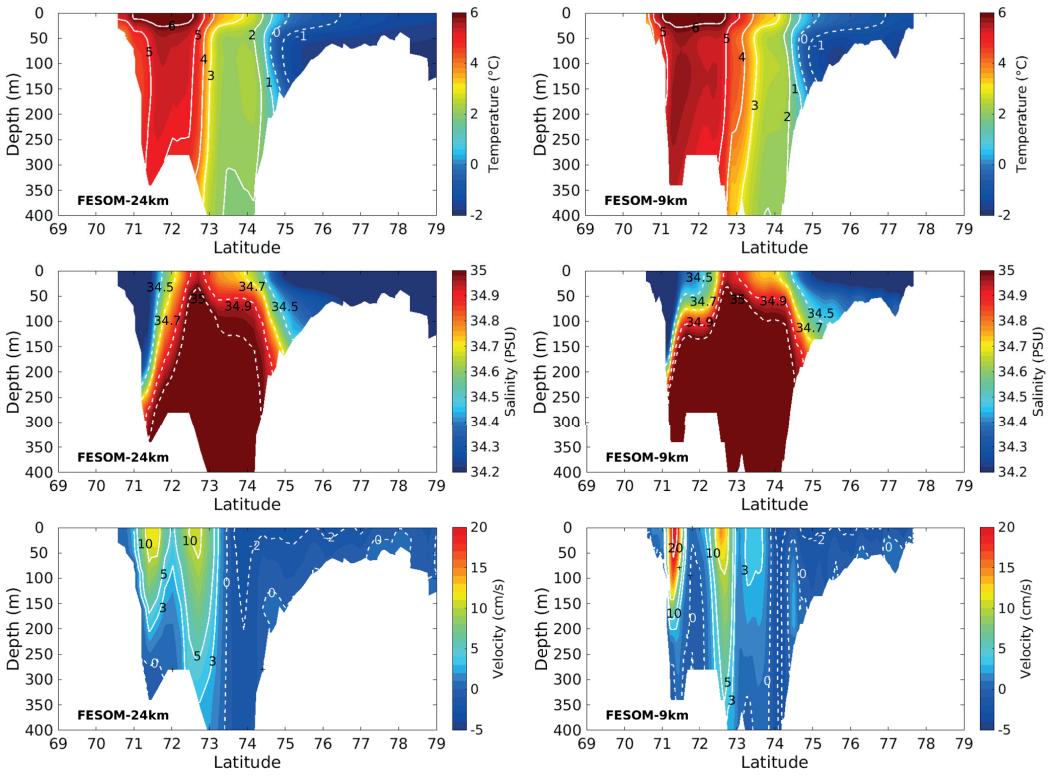

Figure 4.13: Simulated temperature, salinity and velocity at the 24°E section averaged over 1997–2007.

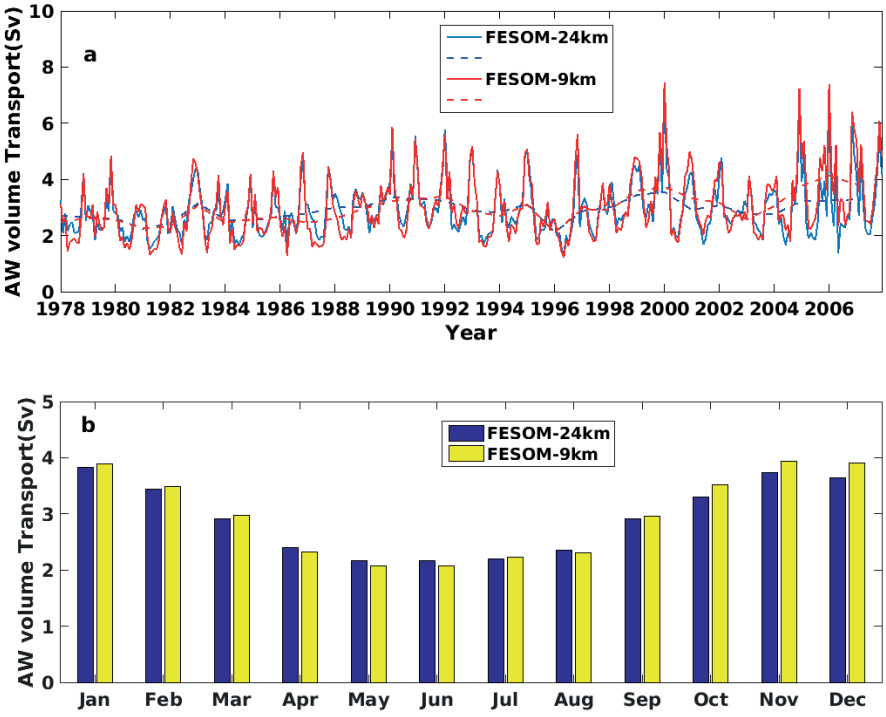

Figure 4.14: (a) Simulated monthly (solid) and winter-centred annual mean (dotted) time series of Atlantic Water volume transport in Barents Sea Opening. The volume transport is calculated for the eastward current at 20°E with temperature warmer than 3°C. (b) The same as (a) but for the seasonal cycle.

Sv in FESOM-24km and 2.97 Sv in FESOM-9km. The updated observation estimation of mean AW volume transport in the BSO is 2.6 Sv (*Skagseth et al.*, 2011). The two simulations slightly overestimated this volume transport. For time period 1978-2007, the correlation coefficients of winter centred annual mean AW transports at the BSO and the Iceland-Scotland Ridge are 0.58 in FESOM-24km and 0.73 in FESOM-9km (not shown). These correlation coefficients are larger than those at Fram Strait (see the last section), indicating that the interannual variability of the AW volume transport is gradually weakened on its way toward the Arctic Ocean. Similar to the AW volume transport in Fram Strait, there was also no significant trend in AW volume transport in BSO. Figure 4.14b shows almost the same seasonal variability and magnitude of AW volume transport in the two runs, strong in winter and weak in summer, which agrees with the findings from observation (*Ingvaldsen et al.*, 2004; *Skagseth et al.*, 2008; *Smedsrud et al.*, 2010).

4.4 Summary

In this chapter, we assessed the FESOM performance with two different local resolutions in the Arctic Ocean. Our focus was mainly on sea ice and freshwater in the Arctic Ocean, fluxes through the Arctic gateways, and the Atlantic Water inflow in Fram Strait and Barents Sea Opening.

Both the low and high resolution simulations can reproduce realistic sea ice extent, sea ice thickness and freshwater storage in the Arctic Ocean. The simulated oceanic fluxes through the Arctic gateways are also in a reasonable range compared to the obseravtions. The model results are compared to those of the CORE-II models (*Wang et al.*, 2016a,b), which are the ocean-ice components of different state-of-the-science climate models. For the quantities studied in this thesis, our results are largely within the model spread of the CORE-II models.

Increasing model resolution tends to improve the representation of fluxes through the Arctic gateways and the salinity (thus FWC) structure in the Arctic basin. The former is because some of the gateways are very narrow and high resolution is required to resolve the throughflows. The FWC is more

distinct between the Canadian and Eurasian Basins in the high resolution run, as expected from observations. This is consistent to the finding in *Wang et al.* (2016b) that high resolution tends to improve the spatial distribution of FWC.

However, the high resolution used in our simulations is still not fine enough to fully resolve some of the narrow gateways, for example, the Nares Strait (about 10 km at the narrowest location). Therefore, more pronounced improvement can be expected when we use finer resolution. It is also the case for the Atlantic Water inflow to the Arctic Ocean. The Rossby Radius at Fram Strait is less than 4 km. With 9 km resolution in our simulation, meso-scale eddies are not resolved, so the zonal eddy transport is missing and the simulated WSC is confined to the coast. Our study shows that the simulated ocean results are sensitive to resolution, and it also indicates that the resolution should be high enough to resolve meso-scale eddies or small geometric features in order to obtain results closer to observations.

Chapter 5

On the mechanism determing the sea ice interannual variability in the Barents Sea

5.1 Introduction

Barents Sea is a relatively shallow marginal sea of the Arctic Ocean, bordered by the shelf edge towards the Norwegian Sea to the west, the archipelagos of Svalbard to the northwest, Franz Josef Land to the northeast and Novaya Zemlya to the east (Figure 5.1). The average depth of Barents Sea is 230 m, and the maximum depth of about 500 m is found in the western part of the channel Bjørnøyrenna.

Located along one of the two pathways of Atlantic Water (AW) entering the Arctic, The Barents Sea communicates with both warm Atlantic Ocean and cold Arctic Ocean through water mass, heat and sea ice exchange. On the other hand, the warm northward flowing AW keeps the Barents Sea partly ice free even in the winter time, allowing for strong atmospheric cooling and modification on the AW. Because of its important location and the strong interactions among ocean, sea ice and atmosphere, the Barents Sea is a critical region in climate system and plays an important role in the Northern Hemisphere climate.

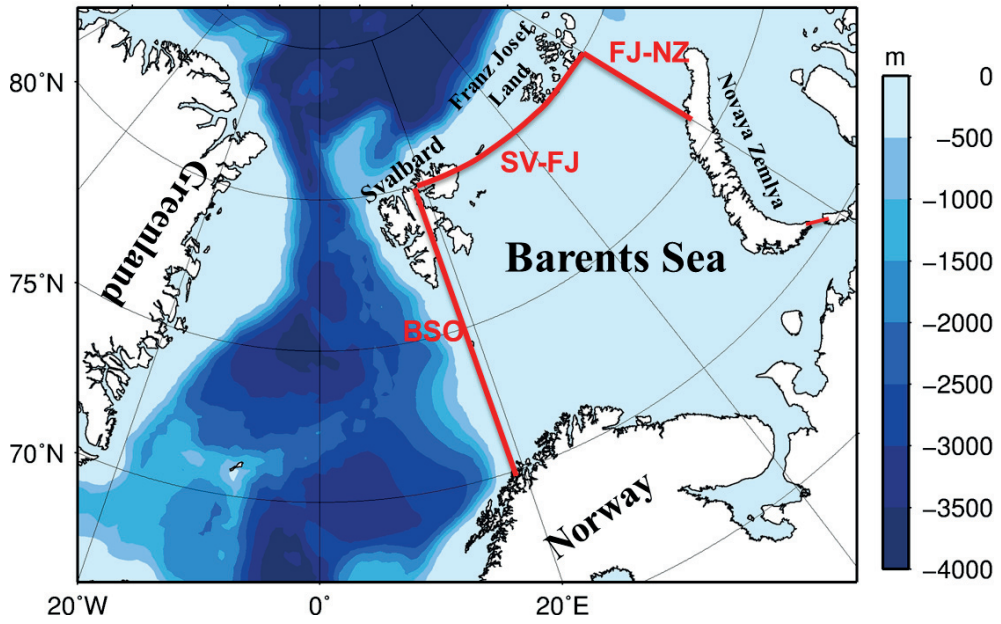

Figure 5.1: Bathymetry in the Barents Sea. Sections discussed in the text are shown with red lines.The Barents Sea domain in this chapter is defined with the red lines and the southern continent

Sea ice, as one of the most important components of the Arctic climate system, is a primary sensitive indicator of the state of climate in the Arctic, and its sensitivity incorporates and reflects the climate change and variability on global scales (*Stroeve et al.*, 2007; *Serreze et al.*, 2007; *Comiso et al.*, 2008; *Screen and Simmonds*, 2010). Sea ice in Barents Sea, as part of the Arctic sea ice component, its variability on different time scales are very important for the entire Arctic air-sea-ice system. Recent studies indicated that the Barents Sea ice condition has significant influences on the Eurasian climate system (*Petoukhov and Semenov*, 2010; *Inoue et al.*, 2012; *Outten and Esau*, 2012; *Yang and Christensen*, 2012).

5.1.1 Sea ice variability in the Barents Sea

Most of the sea ice in the Barents Sea is formed locally due to the atmospheric cooling during winter. Solar heating melts most of the sea ice during the melting season again (*Vinje and Kvambekk*, 1991; *Vinje*, 1998, 2001), so

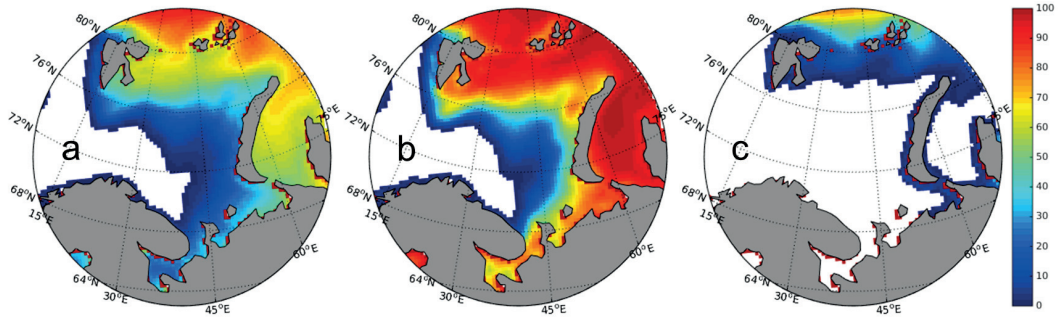

Figure 5.2: NSIDC observed sea ice concentration averaged over the period 1979–2007: (a) annual mean, (b) March mean, (c) September mean.

sea ice in this area has a large seasonal cycle. Satellite passive-microwave observations provide the best data yet available for observing the Arctic ice cover on a repetitive basis throughout the year. Figure 5.2 shows the Barents Sea sea ice concentration mapped on 25km*25km grids from the National Snow and Ice Data Center (NSIDC) (*Fetterer et al.*, 2009). In contrast to other marginal Arctic seas, a significant part of the Barents Sea (along the southwestern coast) is free of ice during the whole year, associated with the warm AW inflow through the Barents Sea Opening (BSO) . High sea ice concentration is located in the northern part of the Barents Sea.

The seasonal variability of sea ice in Barents Sea is large as shown by the NSIDC sea ice concentration (Figures 5.2b and 5.2c). In October/November the freezing process begins, and as a consequence of atmospheric cooling, ocean heat loss leads the surface ocean to the freezing point. Sea ice extent starts to increase and reaches its maximum in March or April. Later in May the ice extent begins to decrease and in August or September it reaches its minimum. Non-locally formed sea ice is also exported from adjacent basins to the Barents Sea: through the strait between Svalbard and Franz Josef Land (the SV-FJ section) from the Arctic to the Barents Sea and through the strait between Franz Josef Land and Novaya Zemlya (the FJ-NZ section) from the Kara Sea to the Barents Sea. *Kwok* (2009) used satellite measurements to estimate sea ice transport from the Arctic Ocean into the Barents Sea through the SV-FJ section and found that the sea ice flux has a significant seasonal cycle, with maximum in May and minimum in August. In the meanwhile,

sea ice is exported to the Nordic Seas through the BSO.

The sea ice in the Barents Sea is also characterized by a significant interannual variability. Many previous studies have already pointed out that a number of processes contribute to the Barents Sea ice interannual variability, including large-scale atmospheric circulation (*Maslanik et al.*, 2007; *Deser and Teng*, 2008; *Zhang et al.*, 2008; *Pavlova et al.*, 2014), cyclone activities (*Sorteberg and Kvingedal*, 2006; *Simmonds and Keay*, 2009), wind-induce sea ice transport from the Arctic basin (*Koenigk et al.*, 2009; *Kwok*, 2009) and oceanic heat input from the North Atlantic (*Ådlandsvik and Loeng*, 1991; *Årthun et al.*, 2012; *Pavlova et al.*, 2014). Different from the Arctic Basin, the entire Barents Sea is almost ice free during summer, so the interannual and longer time scale sea ice variability in the Barents Sea mainly reflects the changes in winter sea ice condition.

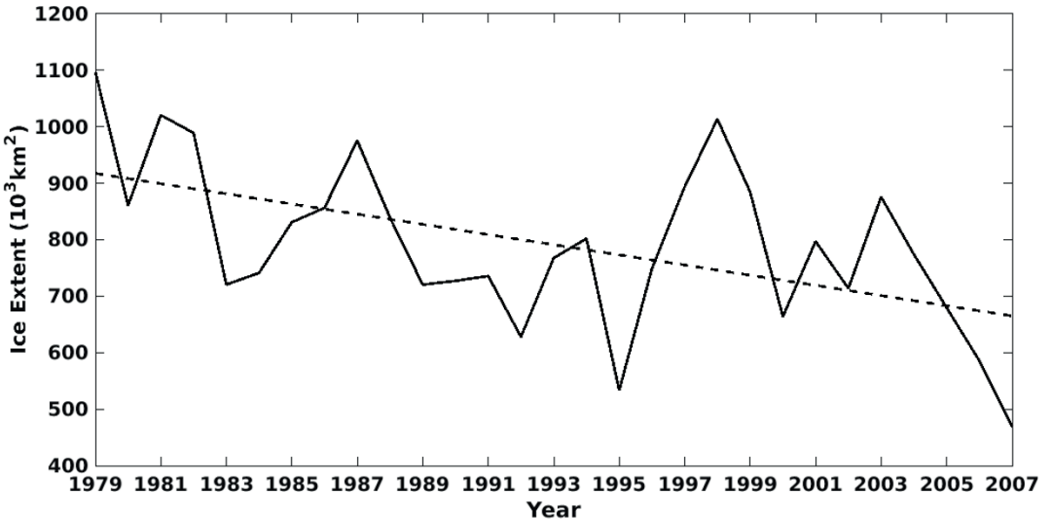

Figure 5.3: Barents Sea winter (Mar. and April) mean sea ice extent for the period 1979–2007 from the NSIDC satellite data. The dashed line shows the linear trend.

Figure 5.3 shows the time series of the observed winter sea ice extent (SIE, defined as the total area of grid cells with at least 15% sea ice concentration) in the Barents Sea for the period 1979–2007. The ice-covered area in the Barents Sea region has a large interannual variability, with a

significant descending trend over the last decades. The observed winter SIE has a mean value of $7.91 \times 10^5\, km^2$ and an interannual variability (defined as the standard deviation) of $1.47 \times 10^5\, km^2$. The total dramatic decline of winter SIE is $2.52 \times 10^5\, km^2$ during the last three decades, with a trend of about $-9.0 \times 10^3 \quad km^2/year$. On the interannual time scale the SIE in the Barents Sea and in the whole Arctic Ocean does not always covary (*Ikeda*, 1990; *Pavlova et al.*, 2014), indicating that the driving mechanisms for the interannual variability of the Barents Sea and Arctic Ocean SIE are different.

Possible driving mechanisms for the Barents Sea sea ice variability have been discussed in previous studies (*Koenigk et al.*, 2009; *Årthun et al.*, 2012; *Pavlova et al.*, 2014). Statistical methods (e.g. correlation and regression analysis) were used to understand the relationship between potential driving factors (Sea Level Pressure (SLP), Sea Surface Temperature (SST), oceanic heat transport, and sea ice transport) and sea ice variables (SIE, Sea Ice Volume (SIV), and Sea Ice Area (SIA)). Previous studies have focused on two direct contributions to the sea ice interannual variability: Oceanic heat transport from North Atlantic (the thermodynamic aspect) and sea ice import from the Arctic basin (the dynamic aspect). *Koenigk et al.* (2009) found that sea ice interannual variability in Barents Sea is mainly determined by variations in sea ice import from the Arctic Ocean, while the oceanic heat transport from North Atlantic plays an important role on longer time scales and is less importance for the interannual sea ice variations. In their study, SIV from a 465-year pre-industrial run in a global coupled model is chosen to represent the sea ice condition in the Barents Sea. Their annual mean SIV time series in the Barents region has a low correlation coefficient with the annual mean horizontal oceanic heat transport on the interannual time scale. However, the changing rate of annual mean SIV in Barents Sea ($km^3/year$) highly correlates with the net sea ice fluxes into the Barents Sea (r=0.7). They also pointed out that the sea ice import into the Barents Sea from the Arctic Ocean is mainly determined by the local wind stress.

Årthun et al. (2012) had an opposite view on the dominating mechanism for the Barents Sea ice interannual variability. They suggest that the oceanic heat flux carried by the Atlantic inflow is the main driver for the Barents Sea

ice interannual variability and the longer-term trend. Both observations (sea ice date from NSIDC, hydrographic data from moorings and wind reanalysis data from NCEP) and a regional ice-ocean model were used in their study. Winter-centered (July-June) annual mean SIA was used as an indicator for sea ice condition. Although the correlation between wind and SIA is high in their results, by referring to the lagged response of SIA to wind they claimed that the wind influences the Barents Sea ice mainly through its effect on ocean circulation rather than through the direct influence on sea ice import. As another evidence to support their idea, they illustrated that the BSO heat transport and ocean temperature have the same outstanding trend as the Barents Sea ice descending trend, while the local wind trend is more modest. No direct analysis on the relationship between the sea ice transport to the Barents Sea and the Barents Sea SIA was carried out in their work.

Later on *Pavlova et al.* (2014) studied the correlations between Barents Sea SIE (monthly mean data from NSIDC) and both SST (monthly mean data from NSIDC) and SLP (monthly mean data from NCAR). They concluded that the SST and wind contribute almost equally to the variability of SIE in the Barents Sea in winte, while in summer both SST and wind have weaker correlation with the SIE in the Barents Sea. In their paper they indicated that SST reflects the strength of warm Atlantic inflow and the SLP pattern determines the sea ice transport from the Arctic Ocean into the Barents Sea.

As reviewed above, there is no agreement on the dominating mechanism on the Barents Sea sea ice interannual variability. Among previous studies, there exist even opposite opinions on which is the dominant driving force, either dynamic (sea ice import) or thermodynamic (oceanic heat input) forcing. In this study we add effort to improve the understanding of the sea ice interannual variability in the Barents Sea. We use numerical simulations to reveal the driving mechanism by quantifying the sea ice variation.

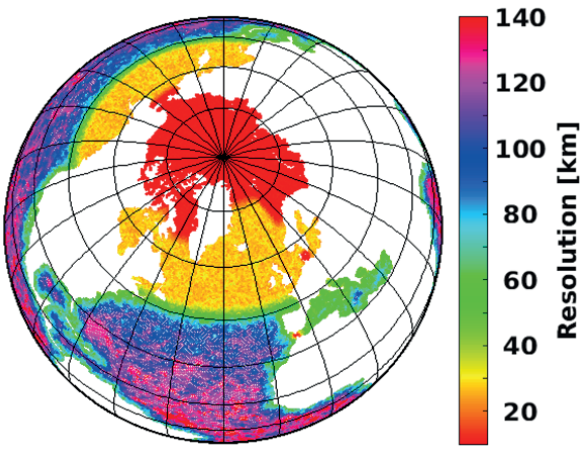

Figure 5.4: Model resolution.

5.2 Model setups

The high resolution simulation with 9 km resolution in the Arctic Ocean described in the last chapter (Figure 5.4) is used here as the control run. The model is run from 1958 to 2007. A sensitivity run was carried out starting from the 1977 control run result. This sensitivity run is named as 'import closure run': the sea ice velocities in two sections, one between Svalbard and Franz Josef Land(80 °N, referred as SV-FJ), the other between Franz Josef Land and Novaya Zemlya(60 °E, referred as FJ-NZ), were enforced to zero. In this case there is no sea ice exchange between the Arctic basin and Barents Sea. The location of the two sections is shown in Figure 5.1.

5.3 Simulated variability

The model performance on modelling the sea ice condition in the Barents Sea region is evaluated here for the control run. Figure 5.5 shows the 2D distribution of sea ice concentration in March for the Barents Sea region and the NSIDC observation averaged over the period 1979–2007. The model can reproduce the spatial pattern of sea ice concentration, with the southwestern Barents Sea ice free. The simulated SIE time series is shown in Figure 5.6

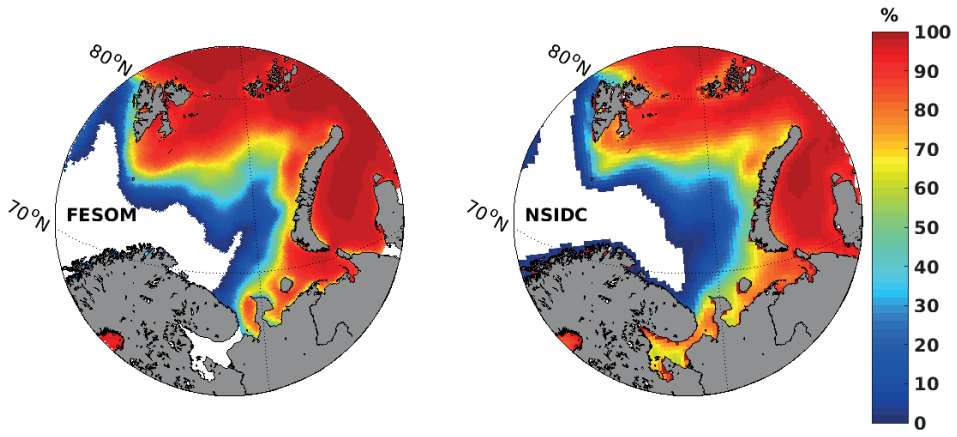

Figure 5.5: March sea ice concentration in Barents Sea for (left) the FESOM simulation and (right) NSIDC satellite observation averaged over the period 1979 – 2007

together with the NSIDC observation. The modelled monthly mean sea ice extent reveals a strong seasonal cycle with peaks in March or April and minimum in September, very consistent with the observation. The winter sea ice extent is slightly overestimated by the model. For the period 1979–2007, the mean winter sea ice extent in Barents Sea is $8.22 \times 10^5\, km^2$ and $7.91 \times 10^5\, km^2$ for the model and observation, respectively. Both the modelled and observed summer SIE in Barents Sea is close to zero, indicating a nearly ice free condition.

The model well reproduced the interannual variability and negative trend for the SIE in the Barents Sea. The modelled (observed) winter SIE has a standard deviation of $1.39 \times 10^5\, km^2$ ($1.47 \times 10^5\, km^2$) and a trend of $-8.2 \times 10^3\, km^2/year$ ($-9.0 \times 10^3\, km^2/year$). The correlation between the simulated and observed winter SIE is significant (r=0.92 for winter mean and r=0.90 for annual mean). The winter mean and annual mean SIEs are different in their magnitude but have very similar variability and trend, confirming that our analysis can be just focused on the winter sea ice condition.

The simulated SIE and SIV in the Barents Sea are shown in Figure 5.7. The SIE and SIV covary on both the seasonal and interannual time scales, so

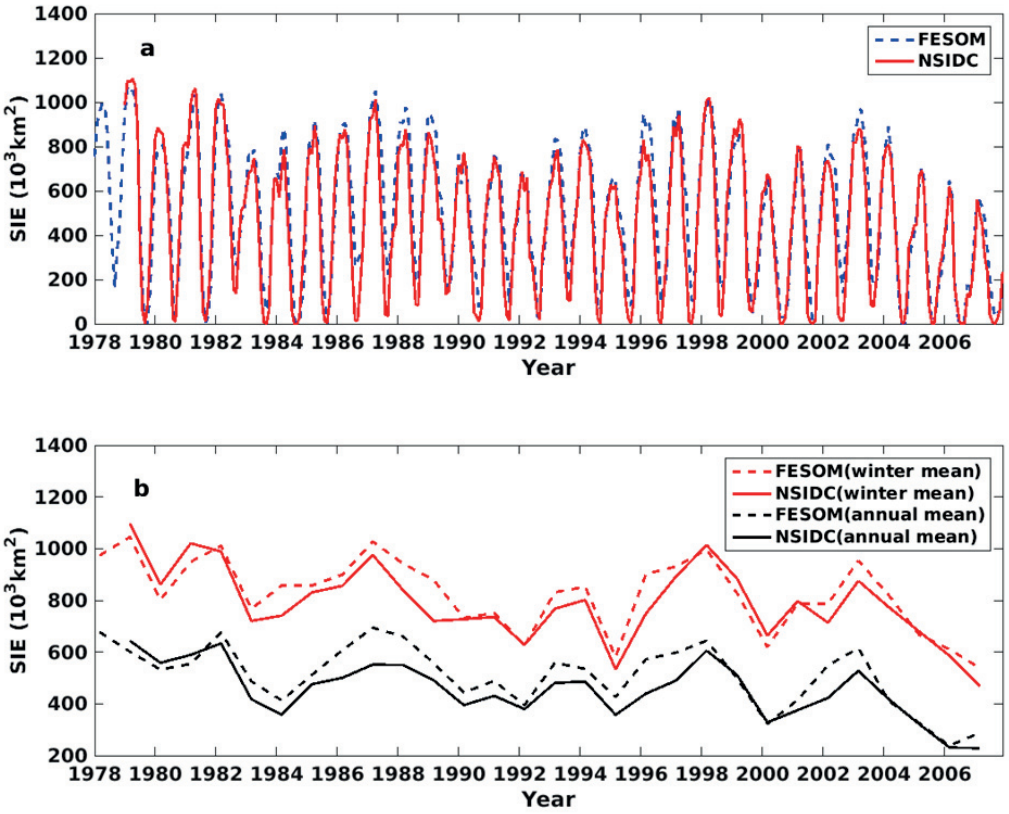

Figure 5.6: (a) Monthly mean sea ice extent from the FESOM simulation and NSIDC observation. (b) The same as (a) but for the winter (March and April) mean and annual mean.

the variability of sea ice in the Barents Sea can be quantified with either SIE or SIV. That is, we can just choose one of them that is practically more convenient, to study the variability of sea ice in the Barents Sea. Although SIE (or SIA) can be directly validated using satellite data, it is not a conserving variable (area fluxes into a domain are not necessarily equal to the changes of the ice area inside the domain). On the contrary, SIV is a conserving variable whose changes can be compared to the source terms quantitatively. In this work we will use SIV to explore the sea ice variability in the Barents Sea.

The annual change rate of Barents Sea SIV is determined by the net

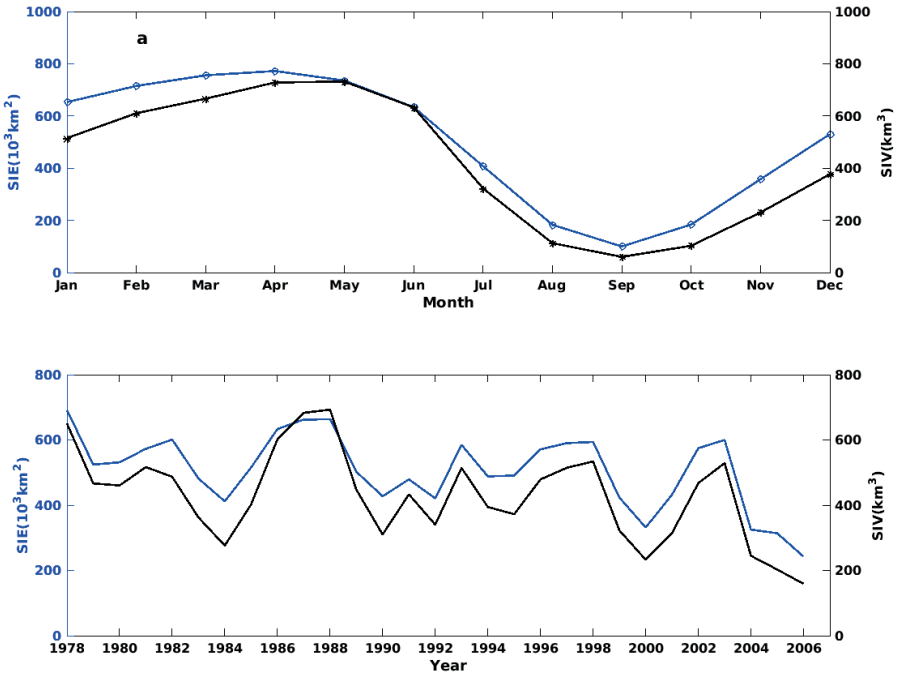

Figure 5.7: Sea ice extent and volume in Barents Sea: (upper) seasonal cycle, (bottom) annual mean.

annual mean sea ice transport across the boundaries and the net annual mean thermodynamic growth rate (sum of the freezing and melting rates) within the Barents Sea. The time series of sea ice transport across the Barents Sea boundaries are shown in Figure 5.8. For the period 1978–2007, the mean transport of SIV from the Arctic Ocean across the SV-FJ section is $423\,km^3/year$, from the Kara Sea across the FJ-NZ section is $272\,km^3/year$, and across the BSO is $-346\,km^3/year$. Thus the net mean SIV transport into the Barents Sea is about $349\,km^3/year$. The SIV transports at the FJ-NZ section and BSO tend to be in a opposite phase. Therefore the net SIV transport into the Barents Sea is governed by the import from the Arctic Ocean across the SV-FJ section(r=0.89).

Kwok (2009) estimated the annual mean SIV transport across the SV-FJ section to be about $37(39)\,km^3/year$ using the 29-yr (1979-2007) satellite

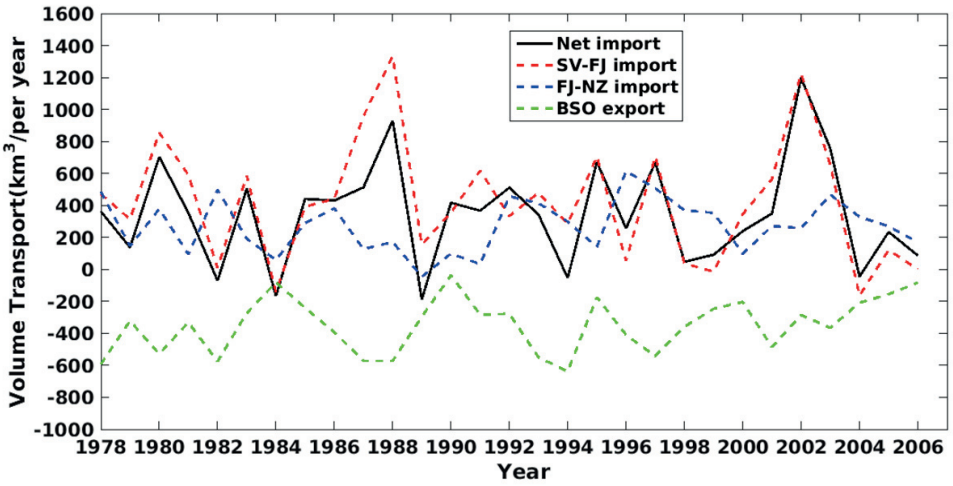

Figure 5.8: Annual mean (April to March) net SIV transport into the Barents Sea and SIV transport across the boundaries. Positive value is for sea ice inflow to the Barents Sea.

record. This estimate is one order of magnitude lower than our simulated result, although the simulated variability matches the observation by *Kwok* (2009) well. The ocean-sea ice model simulation by *Köberle and Gerdes* (2003) shows that the SIV transport into Barents Sea east of Svalbard is on the same order as our simulation. In the coupled model simulation by *Koenigk et al.* (2009), the mean SIV transport into Barents Sea amounts to $870 km^3/year$. The CORE-II multi-model mean sea ice transport into the Barents and Kara Seas through the northern boundary of Barents and kara Seas is about $317\, km^3/year$ (*Wang et al.*, 2016a).

5.4 What drives the interannual variability

Årthun et al. (2012) suggest that the variability of Atlantic heat inflow through the BSO drives the sea ice interannual variability in the Barents Sea. The simulated mean oceanic heat flux through the BSO is 76 TW, consistent with the observational estimation ∼70 TW (*Smedsrud et al.*, 2010; *Skagseth et al.*, 2011). Figure 5.9a shows that both the SIE and the SIV in the Barents Sea are highly correlated with the BSO heat flux at one year lag (r= -0.72 for

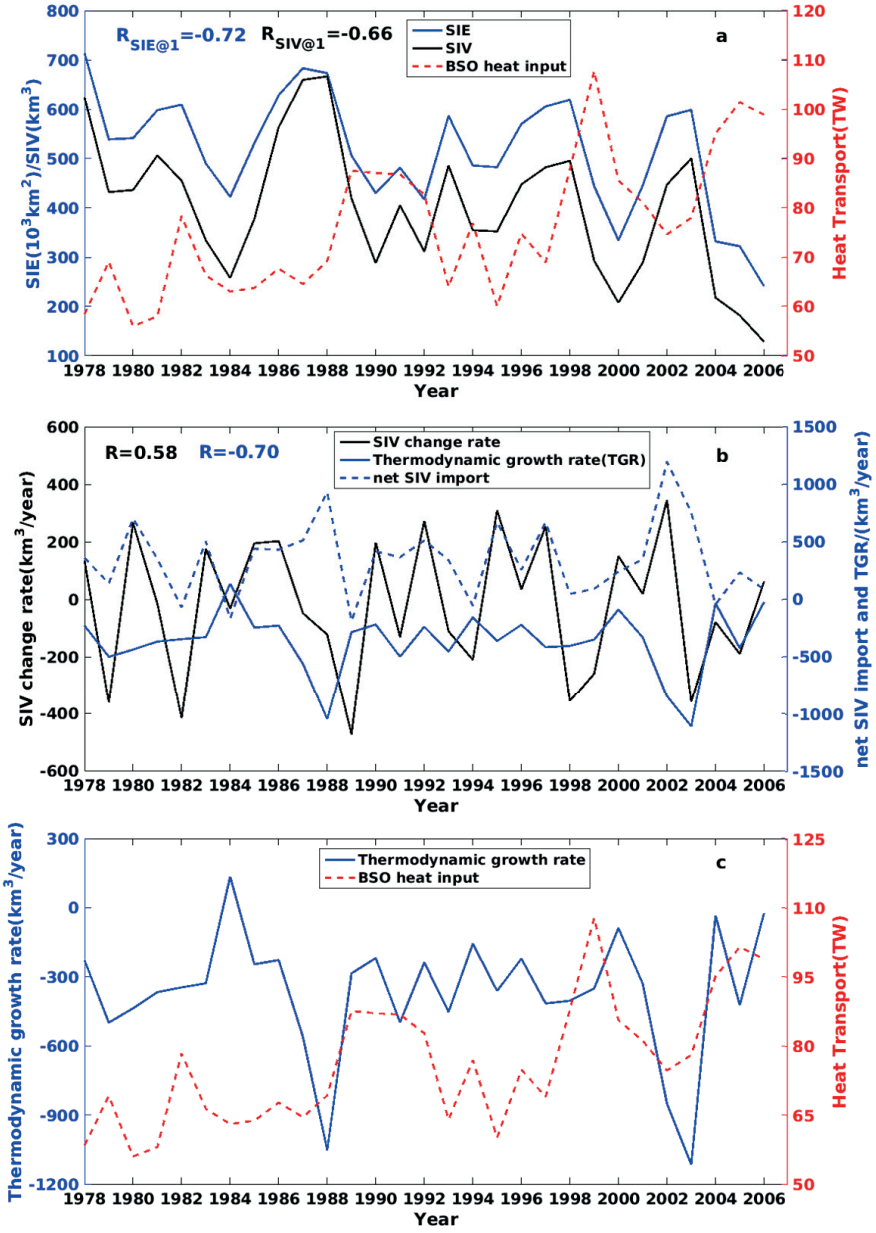

Figure 5.9: For control run, (a) Barents Sea sea ice volume and extent vs. BSO heat input ("R" in blue for the correlation coefficient between SIE and BSO heat input, "R" in black for the correlation coefficient between SIV and BSO heat input). (b) The Barents Sea sea ice volume chage rate, thermodynamic growth rate, and the net sea ice volume flux through the Barents Sea boundaries ("R" in black for the correlation coefficient between SIV change rate and net SIV import, "R" in blue for the correlation coefficient between TGR and net SIV import). (c) The sea ice thermodynamic growth rate vs. the BSO heat input.

SIE and r= -0.66 for SIV). Based on this correlation relationship one might conclude that the BSO heat flux drives the interannual variability of sea ice in the Barents Sea, as suggested by *Årthun et al.* (2012). However, the thermodynamic growth rate of sea ice in the Barents Sea is anti-correlated with the net SIV flux (r= -0.70, shown in Figure 5.9b), indicating that the change of SIV within the Barents Sea is not thermodynamically driven. Indeed, the variability of thermodynamic growth rate cannot be explained by the BSO heat flux (Figure 5.9c). Actually, when the BSO heat flux is low, the sea ice thermodynamic growth rate is also low. Therefore, although the correlation between the SIV and BSO heat flux shown in Figure 5.9a is statistically significant, it cannot be used as an argument to determine what is the driving force for the SIV interannual variability in the Barents Sea.

Figure 5.9b shows that the variability of SIV change rate can be explained by that of the net SIV import flux (r=0.58). The sea ice thermodynamic growth rate covaries with the net SIV import flux. When the sea ice import increases, the Barents Sea SIV increases, but some of the entering sea ice will melt, independent on whether the BSO heat flux increases or not (Figure 5.9c). Therefore, the sea ice thermodynamic growth rate reacts to the sea ice fluxes through the Barents Sea boundaries passively, and the wind driven sea ice transport through the Barents Sea boundaries (the dynamic forcing) drives the interannual variability of SIV in the Barents Sea.

In the sensitivity experiment, the ice drift velocity at the SV-FJ and FJ-NZ sections is enforced to zero, and there is no sea ice import from the Arctic Ocean and Kara Sea into the Barents Sea. The sea ice in the Barents Sea can only be exported through the BSO. The simulated SIE and SIV in the control and sensitive runs are shown in figure 5.10a. Without sea ice import through the SV-FJ and FJ-NZ sections, both the SIE and SIV declined significantly. The variability of both the SIE and SIV also becomes weaker than the control run. Especially, during the high SIV import years (during 1984–1990 and 2000–2004), the dramatically high Barents Sea SIV simulated in the control run is not obtained in the sensitivity run. The significant weakening of the SIV interannual variability also indicates the leading role of sea ice transport in driving the variability. After removing

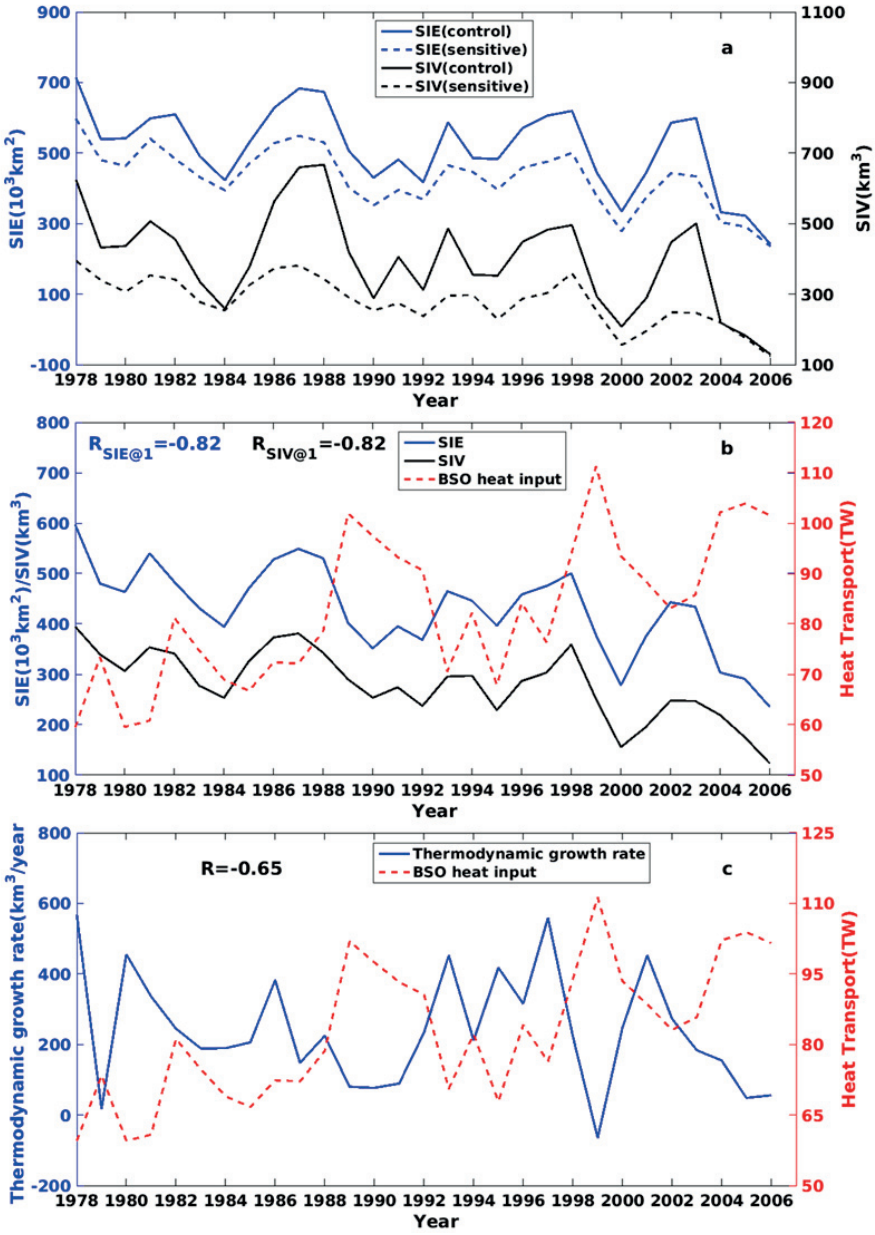

Figure 5.10: For sensitivity run, (a) Barents Sea sea ice volume and extent in control run vs. those in sensitivity run. (b) Barents Sea sea ice volume and extent vs. BSO heat input ("R" in blue for the correlation coefficient between SIE and BSO heat input, "R" in black for the correlation coefficient between SIV and BSO heat input). (c) The sea ice thermodynamic growth rate vs. the BSO heat input.

the variability induced by sea ice import, the correlation between SIE/SIV and heat flux becomes slightly higher(in Figure 5.10b). The most significant change in the sensitivity run is that the thermodynamic growth rate become positive (in Figure 5.10c), while it is negative in the control run, although the oceanic heat fluxes through BSO are almost the same in both runs. In the sensitivity run, due to the sea ice export from the BSO, the net sea ice transport into Barents Sea is negative, resulting in the positive sea ice thermodynamic growth rate to generate more ice to compensate the loss of sea ice. However, the strong anti-correlation between the thermodynamic growth rate and BSO heat transport indicates that the variability of the thermodynamic growth rate is also significantly controlled by the BSO heat flux. It is interesting to see that the descending trend of SIV is almost the same in the two simulations, indicating that the trend is not associated with the sea ice import flux, but rather caused by the trend of BSO heat flux as suggested by *Koenigk et al.* (2009).

5.5 Conclusion

In this chapter, we evaluated the performance of the global sea ice-ocean model FESOM on sea ice simulation in the Barents Sea. The simulated sea ice mean state and variability in the Barents Sea show very good agreement with observations.

The sea ice import from the Arctic Ocean into the Barents Sea drives the interannual variability of Barents Sea SIV, while the sea ice thermodynamic growth rate just reacts to the sea ice flux, independent on the variability of BSO heat flux. The determining role of the sea ice flux into the Barents Sea is due to its relatively large magnitude. In the control run, large net sea ice import leads to strong sea ice melting in Barents Sea, while in the sensitivity experiment, the sea ice import from adjacent basins is blocked, and the sea ice flux become negative (only export through BSO), this leads to the positive thermodynamic growth rate. The oceanic heat flux in both experiments are almost the same, but the thermodynamic growth rate changed its sign. This illustrate the controlling role of the SIV transport on the Barents Sea SIV

variability, although the BSO oceanic heat flux has a significant impact on the thermodynamic growth rate in the sensitivity run because of the reduced magnitude of SIV transport.

Chapter 6

Summary and Outlook

In this PhD project, the performance of FESOM in long-term simulations was evaluated with focus on the North Atlantic and the Arctic Ocean. A case study about the impact of Greenland Ice Sheeting (GrIS) melting was also conducted. The advantage of unstructured-mesh functionality was used in global simulations with variable resolution. We carried out hindcast simulations with different resolutions (24km and 9km) locally in the Arctic and surrounding regions in order to explore model sensitivity to resolution. In this work the particular attention was paid to the Barents Sea sea ice variability. Besides the control run a sensitivity experiment was conducted to reveal the dominant mechanism on sea ice interannual variability in the Barents Sea.

The key findings of this work can be summarized as follows:

- The long term simulation of FESOM with CORE interannual forcing shows that FESOM can reproduce the past ocean variability successfully. The modelled AMOC strength and structure agree with observational estimates and previous model simulations (*Lumpkin and Speer*, 2003; *Lumpkin et al.*, 2008; *Griffies et al.*, 2009). The summer and winter sea ice concentration in the Arctic Ocean is also well represented in the FESOM long-term integration. The simulated variability of liquid freshwater content is controlled mainly by freshwater exchange through the Arctic gateways, which is similar to that shown in previous studies (*Häkkinen and Proshutinsky*, 2004; *Köberle and Gerdes*, 2007; *Lique*

et al., 2009).

The water-hosing experiment with an additional 0.1Sv freshwater release along the Greenland coast was carried out to study the direct ocean response. The anomalous freshwater input into the ocean not only leads to the reduction in AMOC strength, but also in the strength of its decadal variability. The released freshwater from Greenland can penetrate to the Arctic Ocean, especially in the Eurasian Basin, resulting in the freshening of the Arctic Ocean and weakening of water mass exchange through the Arctic gateways.

- The assessment of FESOM simulations with two mesh refinements of 24km and 9km in the Arctic and surrounding regions shows that both low (FESOM-24km) and high (FESOM-9km) resolutions are capable to realistically simulate the mean state and variability of sea ice condition, freshwater content in the Arctic Ocean, as well as the volume and fluxes transport through the Arctic gateways. The high resolution run tends to improve the representation of fluxes through the Arctic gateways and the salinity (thus the freshwater content) structure in the Arctic basin.

  The high resolution (9km) simulation tends to reduce the unrealistic numerical mixing in the low resolution (24km) simulation, thus better simulates the vertical depth of the AW layer. However, the first Rossby radius is less than 4km at Fram Strait, FESOM-9km can't capture the meso-scale eddies, which play an important role in shedding the warm AW westward to the central and western Fram Strait.

- The good representation of sea ice variability in Barents Sea in FESOM allows us to implement sensitivity runs to study the dominate mechanism driving the interannual variability of sea ice in the Barents Sea. we found that sea ice import from the Arctic Ocean to the Barents Sea is the dominating mechanism determing the sea ice interannual variability in the Barents Sea. Large sea ice import will lead to stronger sea ice melting in the Barents Sea. The oceanic heat input from BSO

doesn't explain the interannual variability of sea ice thermodynamic growth rate, while it determines the trend of the Barents Sea sea ice volume.

Outlook The new study of comparing the Arctic hydrography in the framework of the CORE-II project (*Ilicak et al.*, in press) shows a large spread in the simulated temperature and spatial structure of the Atlantic Water (AW) in the Arctic Ocean. Most models participating in the CORE-II project simulated a progressive thickening of the AW layer, similar to the finding of the Arctic Ocean Model Intercomparison Project (AOMIP) study (*Holloway et al.*, 2007; *Karcher et al.*, 2007). Our simulations at both 24km and 9km resolution still suffers from the deepening of the AW layer in the Arctic Ocean. In order to improve the simulated dynamical processes of the AW, we need to further improve the numerical representation of the model, mainly the advection scheme, which is a common task faced by the international model development community.

In order to simulate the meso-scale eddies in the Arctic Ocean, further increase of local resolution in the Arctic region is necessary in our future work.

Barents Sea is a key transition zone between the warm Atlantic and cold Arctic. The AW passing through the BSO is strongly modified as it crosses the Barents Sea. The modified AW in the Barents Sea enters the Arctic Ocean through St. Anna Trough (SAT), where it interacts with the Fram Strait AW branch (*Dmitrenko et al.*, 2015). The interactions between the two branches and the Arctic shelf-basin water-mass exchange processes need to be further investigated in our future work.

Appendix A

Supplementary

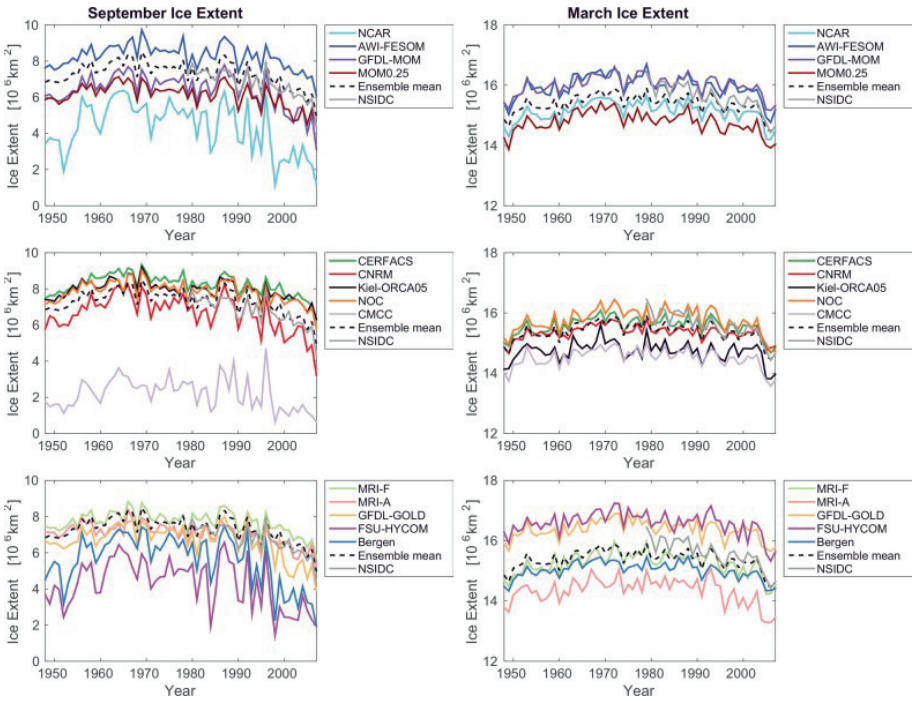

Figure A.1: Northern Hemisphere (left) September and (right) March sea ice extent from models participated in CORE-II-Arctic comparison project,figure 2 in *Wang et al.* (2016a).

Table A.1: Northern Hemisphere sea ice extent: mean, standard deviation (STD), correlation with observation, linear trend and the 2007 value for models participated in CORE-II-Arctic comparison project, from table 2 in (*Wang et al.*, 2016a). Sea ice extent is in 10^6 km^2, and the trend is in 10^4 km^2/year.

	Obs.	NCAR	AWI	MOM	MOM0.25	CERFACS	CNRM	Kiel	NOC	CMCC	MRI-F	MRI-A	GOLD	FSU	Bergen	mean	spread
September																	
mean	6.95	3.99	8.18	6.30	5.96	8.12	6.46	7.85	7.76	2.14	7.65	6.84	6.52	4.00	5.27	6.17	1.87
STD	0.58	1.44	0.61	0.89	0.66	0.42	0.86	0.43	0.49	1.04	0.57	0.61	0.98	1.54	1.47	0.88	0.40
correlation		0.71	0.76	0.63	0.73	0.67	0.67	0.74	0.64	0.68	0.79	0.80	0.62	0.72	0.60	0.69	0.06
Trend 79-03	-5.3	-11	-2.7	-6.4	-4.4	-2.5	-5.9	-2.1	-2.6	-5.2	-3.5	-4.2	-7.5	-10.9	-12.8	-6.0	3.6
Trend 79-07	-7.2	-11.3	-4.9	-8.9	-5.5	-4.3	-8.5	-3.9	-4.5	-6.0	-5.4	-4.9	-9.0	-10.4	-13.6	-7.2	3.0
2007	4.30	1.21	6.09	3.12	4.31	6.34	3.23	6.31	5.80	0.64	5.69	5.26	3.89	1.93	1.98	3.89	2.04
March																	
mean	15.72	15.20	15.98	16.06	14.78	15.66	15.38	14.78	15.87	14.57	15.33	14.43	16.40	16.60	15.06	15.51	0.64
STD	0.34	0.22	0.25	0.22	0.24	0.21	0.15	0.24	0.28	0.20	0.29	0.38	0.24	0.29	0.21	0.24	0.04
correlation		0.65	0.66	0.60	0.76	0.59	0.76	0.65	0.46	0.80	0.45	0.37	0.68	0.21	0.67	0.61	0.16
Trend 79-03	-3.4	-1.4	-1.3	-1.1	-1.6	-1.3	-0.7	-0.9	-1.8	-1.2	-2.1	-3.3	-0.9	-1.3	-1.7	-1.3	0.4
Trend 79-07	-4.7	-2.7	-3.1	-2.5	-2.8	-2.7	-1.7	-2.3	-3.5	-2.7	-3.5	-4.8	-2.2	-3.1	-2.6	-2.9	0.7
2007	14.65	14.50	15.19	15.32	14.04	14.85	14.90	13.97	14.74	13.77	14.52	13.45	15.77	15.63	14.42	14.74	0.62

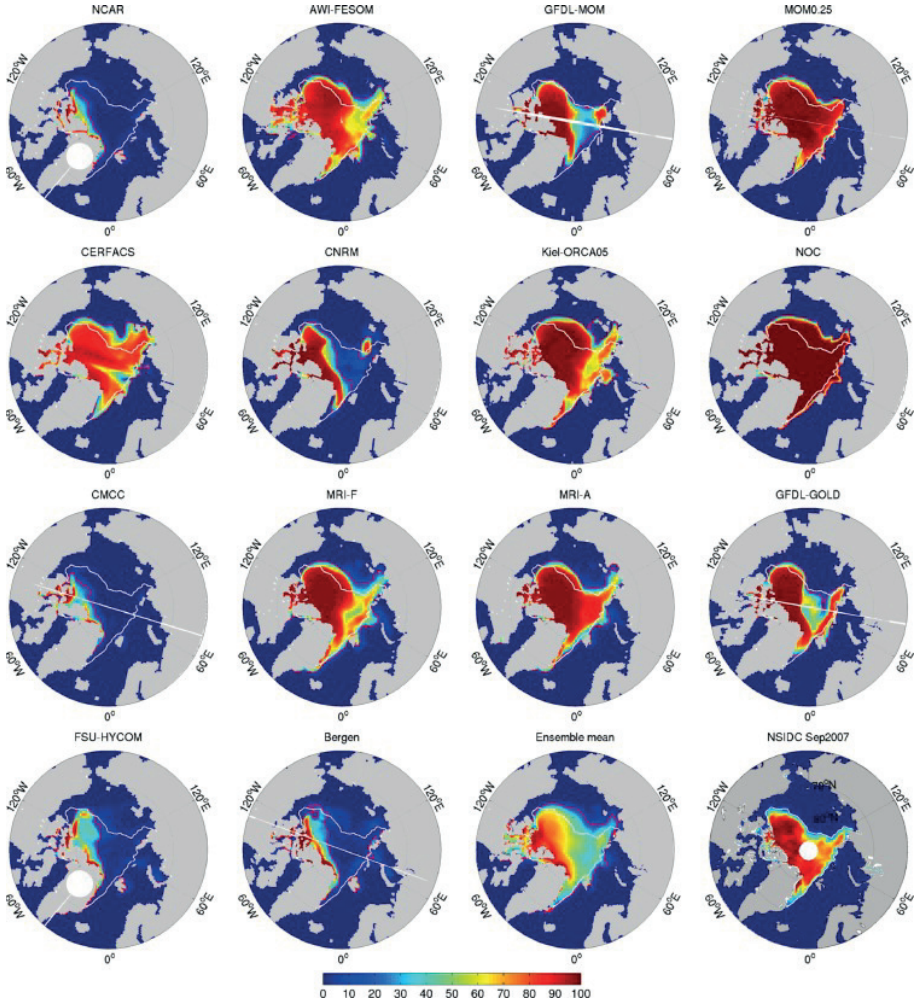

Figure A.2: NSIDC observed and simulated sea ice concentration [%] for September 2007 from models participated in CORE-II-Arctic comparison project, figure 4 in *Wang et al.* (2016a).

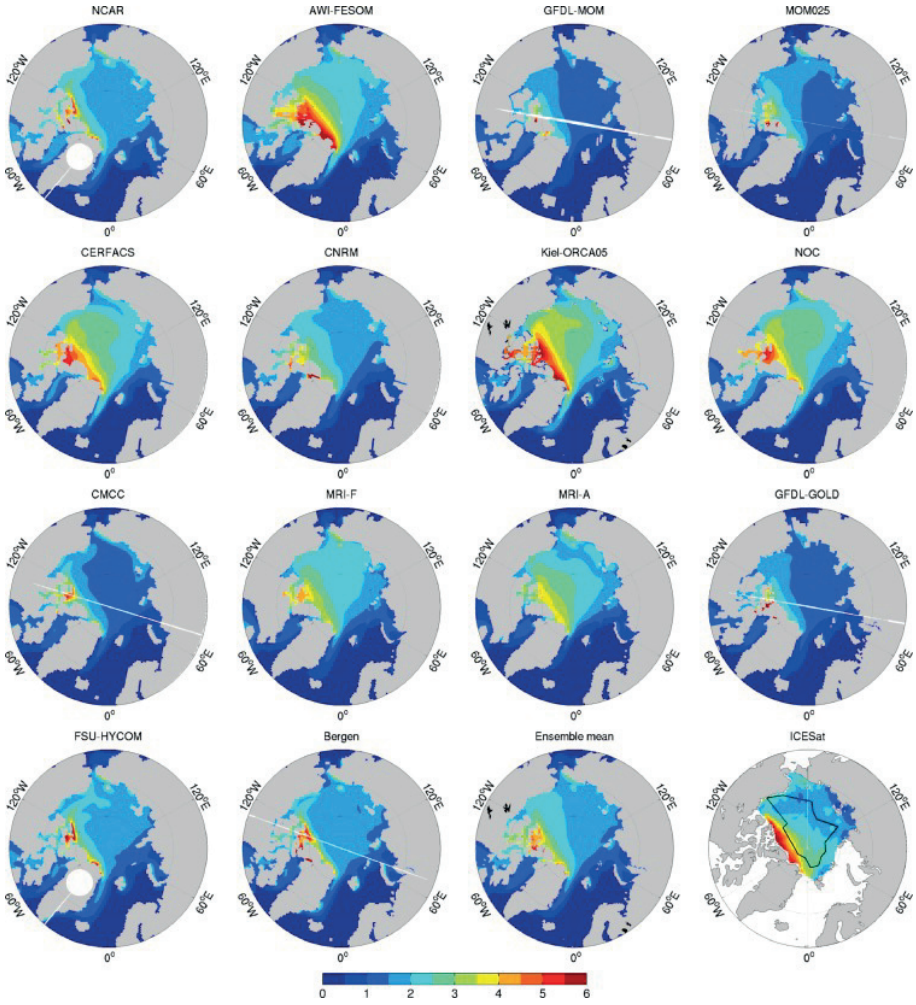

Figure A.3: ICESat observed and simulated mean sea ice thickness $[m]$ for Spring 2004-2007 from models participated in CORE-II-Arctic comparison project, figure 8 in *Wang et al.* (2016a).

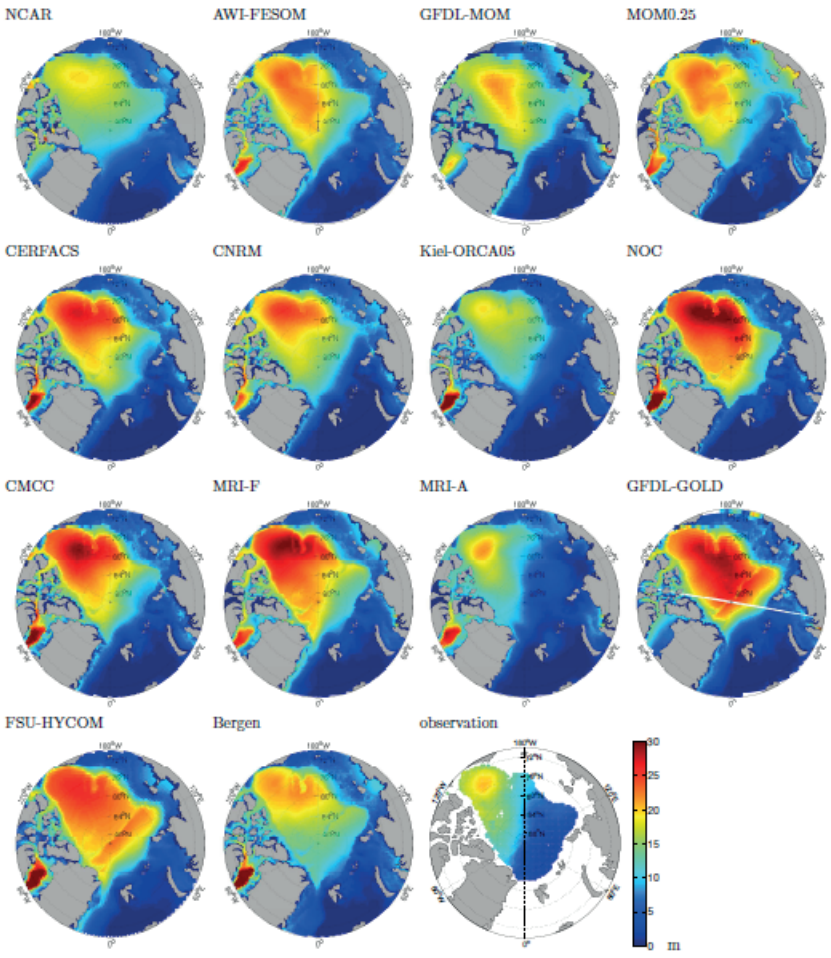

Figure A.4: Liquid freshwater content $[m]$ averaged for 1993-2002 from models participated in CORE-II-Arctic comparison project and from observational data (*Rabe et al.*, 2014), figure 3 in *Wang et al.* (2016b).

Appendix B

Abbreviations

AABW	Antarctic Bottom Water
AMOC	Atlantic Meridional Overturning Circulation
AW	Atlantic Water
AWI	Alfred Wegener Institute for Polar and Marine Research
BI	Bear Island
BSO	Barents Sea Opening
CAA	Canadian Arctic Archipelago
CORE	Coordinated Ocean-Ice Reference Experiment
CLIVAR	Climate Variability and Predictability
DSL	dynamical sea level
DWBC	deep western boundary current
EGC	East Greenland Current
FE	finite element
FEOM	Finite Element Ocean Model
FESOM	Finite Element Sea ice Ocean Model
FJ-NZ	Franz Josef Land-Novaya Zemly section
FW	fresh water
FWC	freshwater content
GFDL	Geophysical Fluid Dynamics Laboratory
GIN	Greenland-Iceland-Norwegian
GrIS	Greenland Ice Sheet

GSL	global sea level
HR	high resolution
ICESat	Ice, Cloud, and land Elevation Satellite
KPP	K-Profile Parameterization
LFWC	liquid freshwater content
LR	low resolution
LSL	local sea level
LSW	Labrador Sea Water
MLD	mixed layer depth
MOC	Meridional Overturning Circulation
NA	North Atlantic
NADW	North Atlantic Deep Water
NCaC	North Cape Current
NCAR	National Center for Atmospheric Research
NCC	Norwegian Coastal Current
NH	Northern Hemisphere
NSIDC	The National Snow and Ice Data Center
NwAC	Norwegian Atlantic Current
Obs.	observation
OGCMs	Ocean General Circulation Models
RAC	Return Atlantic Current
SE	static equilibrium
SIA	sea ice area
SIE	sea ice extent
SIV	sea ice volume
SLP	sea level pressure
SSH	sea surface height
SSS	sea surface salinity
SST	sea surface temperature
STD	standard deviation
SV-FJ	Svalbard-Franz Josef Land section
WGOMD	Working Group on Ocean Model Development
WSC	West Spitzbergen Current

Bibliography

Aagaard, K., J. Swift, and E. Carmack (1985), Thermohaline circulation in the arctic mediterranean seas, *Journal of Geophysical Research: Oceans (1978–2012)*, *90*(C3), 4833–4846.

Aagaard, K., A. Foldvik, and S. Hillman (1987), The west spitsbergen current: disposition and water mass transformation, *Journal of Geophysical Research: Oceans (1978–2012)*, *92*(C4), 3778–3784.

Adcroft, A., C. Hill, and J. Marshall (1997), Representation of topography by shaved cells in a height coordinate ocean model, *Monthly Weather Review*, *125*(9), 2293–2315.

Ådlandsvik, B., and H. Loeng (1991), A study of the climatic system in the barents sea, *Polar Research*, *10*(1), 45–50.

Årthun, M., T. Eldevik, L. H. Smedsrud, Ø. Skagseth, and R. Ingvaldsen (2012), Quantifying the influence of atlantic heat on barents sea ice variability and retreat*, *Journal of Climate*, *25*(13), 4736–4743.

Bentsen, M., H. Drange, T. Furevik, and T. Zhou (2004), Simulated variability of the atlantic meridional overturning circulation, *Climate Dynamics*, *22*(6-7), 701–720.

Beszczynska-Möller, A., R. A. Woodgate, C. Lee, H. Melling, and M. Karcher (2011), A synthesis of exchanges through the main oceanic gateways to the arctic ocean, *in: The Changing Arctic Ocean: Special Issue on the International Polar Year (20072009), Oceanography, 24 (3) 99.*, *82*.

Beszczynska-Möller, A., E. Fahrbach, U. Schauer, and E. Hansen (2012), Variability in atlantic water temperature and transport at the entrance to the arctic ocean, 1997–2010, *ICES Journal of Marine Science: Journal du Conseil*, p. fss056.

Bhatt, U. S., D. A. Walker, J. E. Walsh, E. C. Carmack, K. E. Frey, W. N. Meier, S. E. Moore, F.-J. W. Parmentier, E. Post, V. E. Romanovsky, et al. (2014), Implications of arctic sea ice decline for the earth system, *Annual Review of Environment and Resources*, *39*, 57–89.

Böning, C. W., M. Scheinert, J. Dengg, A. Biastoch, and A. Funk (2006), Decadal variability of subpolar gyre transport and its reverberation in the north atlantic overturning, *Geophysical Research Letters*, *33*(21).

Bourke, R., A. Weigel, and R. Paquette (1988), The westward turning branch of the west spitsbergen current, *Journal of Geophysical Research: Oceans (1978–2012)*, *93*(C11), 14,065–14,077.

Bower, A. S., M. S. Lozier, S. F. Gary, and C. W. Böning (2009), Interior pathways of the north atlantic meridional overturning circulation, *Nature*, *459*(7244), 243–247.

Brauch, J. P., and R. Gerdes (2005), Response of the northern north atlantic and arctic oceans to a sudden change of the north atlantic oscillation, *Journal of Geophysical Research: Oceans (1978–2012)*, *110*(C11).

Broecker, W. S. (1987), *The biggest chill.*

Broecker, W. S., et al. (1991), The great ocean conveyor, *Oceanography*, *4*(2), 79–89.

Cavalieri, D., and C. Parkinson (2012), Arctic sea ice variability and trends, 1979–2010, *Cryosphere*, *6*(4), 881–889.

Cavalieri, D., C. Parkinson, P. Gloersen, and H. Zwally (1996), Sea ice concentrations from nimbus-7 smmr and dmsp ssm/i-ssmis passive microwave data, years 1990–2011, nasa daac at the natl, *Snow and Ice Data Cent., Boulder, Colo.[Updated yearly.]*.

Chafik, L., J. Nilsson, Ø. Skagseth, and P. Lundberg (2015), On the flow of atlantic water and temperature anomalies in the nordic seas toward the arctic ocean, *Journal of Geophysical Research: Oceans*.

Childers, K. H., C. N. Flagg, T. Rossby, and C. Schrum (2015), Directly measured currents and estimated transport pathways of atlantic water between 59.5°n and the iceland-faroes-scotland ridge, *Tellus A*, *67*.

Comiso, J. C. (2006), Abrupt decline in the arctic winter sea ice cover, *Geophysical Research Letters*, *33*(18).

Comiso, J. C. (2012), Large decadal decline of the arctic multiyear ice cover, *Journal of Climate*, *25*(4), 1176–1193.

Comiso, J. C., C. L. Parkinson, R. Gersten, and L. Stock (2008), Accelerated decline in the arctic sea ice cover, *Geophysical Research Letters*, *35*(1).

Conkright, M., S. Levitus, J. Antonov, O. Baranova, T. Boyer, H. Garcia, R. Gelfeld, D. Johnson, R. Locarnini, T. O'Brien, et al. (2002), World ocean database 2001 and world ocean atlas 2001, in *AGU Fall Meeting Abstracts*, vol. 1, p. 0220.

Cunningham, S., M. Baringer, B. Johns, J. Toole, S. Osterhaus, J. Fischer, A. Piola, E. McDonagah, S. Lozier, U. Send, et al. (2010), The present and future system for measuring the atlantic meridional overturning circulation and heat transport.

Cuny, J., P. B. Rhines, and R. Kwok (2005), Davis strait volume, freshwater and heat fluxes, *Deep Sea Research Part I: Oceanographic Research Papers*, *52*(3), 519–542.

Curry, B., C. Lee, and B. Petrie (2011), Volume, freshwater, and heat fluxes through davis strait, 2004-05*, *Journal of Physical Oceanography*, *41*(3), 429–436.

Dai, A., T. Qian, K. E. Trenberth, and J. D. Milliman (2009), Changes in continental freshwater discharge from 1948 to 2004, *Journal of Climate*, *22*(10), 2773–2792.

Danabasoglu, G., S. G. Yeager, D. Bailey, E. Behrens, M. Bentsen, D. Bi, A. Biastoch, C. Böning, A. Bozec, V. M. Canuto, et al. (2014), North atlantic simulations in coordinated ocean-ice reference experiments phase ii (core-ii). part i: mean states, *Ocean Modelling*, *73*, 76–107.

Danabasoglu, G., S. G. Yeager, W. M. Kim, E. Behrens, M. Bentsen, D. Bi, A. Biastoch, R. Bleck, C. Böning, A. Bozec, et al. (2016), North atlantic simulations in coordinated ocean-ice reference experiments phase ii (core-ii). part ii: Inter-annual to decadal variability, *Ocean Modelling*, *97*, 65–90.

Danilov, S., G. Kivman, and J. Schröter (2004), A finite-element ocean model: principles and evaluation, *Ocean Modelling*, *6*(2), 125–150.

Danilov, S., G. Kivman, and J. Schröter (2005), Evaluation of an eddy-permitting finite-element ocean model in the north atlantic, *Ocean modelling*, *10*(1), 35–49.

Danilov, S., Q. Wang, R. Timmermann, N. Iakovlev, D. Sidorenko, M. Kimmritz, T. Jung, and J. Schröter (2015), Finite-element sea ice model (fesim), version 2, *Geoscientific Model Development*, *8*(6), 1747–1761.

de Steur, L., E. Hansen, R. Gerdes, M. Karcher, E. Fahrbach, and J. Holfort (2009), Freshwater fluxes in the east greenland current: A decade of observations, *Geophysical Research Letters*, *36*(23).

Delworth, T., S. Manabe, and R. Stouffer (1993), Interdecadal variations of the thermohaline circulation in a coupled ocean-atmosphere model, *Journal of Climate*, *6*(11), 1993–2011.

Deser, C., and H. Teng (2008), Evolution of arctic sea ice concentration trends and the role of atmospheric circulation forcing, 1979–2007, *Geophysical Research Letters*, *35*(2).

Dickson, R., B. Rudels, S. Dye, M. Karcher, J. Meincke, and I. Yashayaev (2007), Current estimates of freshwater flux through arctic and subarctic seas, *Progress in Oceanography*, *73*(3), 210–230.

Dmitrenko, I. A., B. Rudels, S. A. Kirillov, Y. O. Aksenov, V. S. Lien, V. V. Ivanov, U. Schauer, I. V. Polyakov, A. Coward, and D. G. Barber (2015), Atlantic water flow into the arctic ocean through the st. anna trough in the northern kara sea, *Journal of Geophysical Research: Oceans*, *120*(7), 5158–5178.

Dong, S., S. Garzoli, M. Baringer, C. Meinen, and G. Goni (2009), Interannual variations in the atlantic meridional overturning circulation and its relationship with the net northward heat transport in the south atlantic, *Geophysical Research Letters*, *36*(20).

Eden, C., and R. J. Greatbatch (2003), A damped decadal oscillation in the north atlantic climate system, *Journal of climate*, *16*(24), 4043–4060.

Fahrbach, E., J. Meincke, S. Østerhus, G. Rohardt, U. Schauer, V. Tverberg, and J. Verduin (2001), Direct measurements of volume transports through fram strait, *Polar Research*, *20*(2), 217–224.

Fetterer, F., K. Knowles, W. Meier, and M. Savoie (2002), Sea ice index. national snow and ice data center, boulder, co, digital media.

Fetterer, F., K. Knowles, W. Meier, and M. Savoie (2009), Sea ice index. national snow and ice data center, boulder, co, usa, *Digital Media, updated*.

Fichefet, T., C. Poncin, H. Goosse, P. Huybrechts, I. Janssens, and H. Le Treut (2003), Implications of changes in freshwater flux from the greenland ice sheet for the climate of the 21st century, *Geophysical Research Letters*, *30*(17).

Fichot, C. G., K. Kaiser, S. B. Hooker, R. M. Amon, M. Babin, S. Bélanger, S. A. Walker, and R. Benner (2013), Pan-arctic distributions of continental runoff in the arctic ocean, *Scientific reports*, *3*.

Fischer, H. (1995), Vergleichende untersuchungen eines optimierten dynamisch-thermodynamischen meereismodells mit beobachtungen im weddellmeer= comparison of an optimized dynamic-thermodynamic sea ice

model with observations in the weddell sea, *Berichte zur Polarforschung (Reports on Polar Research)*, *166*.

Gascard, J.-C., C. Richez, and C. Rouault (1995), New insights on large-scale oceanography in fram strait: The west spitsbergen current, *Arctic Oceanography: Marginal Ice Zones and Continental Shelves*, pp. 131–182.

Gent, P. R., and J. C. Mcwilliams (1990), Isopycnal mixing in ocean circulation models, *Journal of Physical Oceanography*, *20*(1), 150–155.

Gerdes, R., W. Hurlin, and S. M. Griffies (2006), Sensitivity of a global ocean model to increased run-off from greenland, *Ocean Modelling*, *12*(3), 416–435.

Glessmer, M. S., T. Eldevik, K. Våge, J. E. Ø. Nilsen, and E. Behrens (2014), Atlantic origin of observed and modelled freshwater anomalies in the nordic seas, *Nature Geoscience*.

Goosse, H., T. Fichefet, and J.-M. Campin (1997), The effects of the water flow through the canadian archipelago in a global ice-ocean model, *Geophysical Research Letters*, *24*(12), 1507–1510.

Gower, J. (2010), Comment on "response of the global ocean to greenland and antarctic ice melting" by d. stammer, *Journal of Geophysical Research: Oceans (1978–2012)*, *115*(C10).

Greatbatch, R. J. (1994), A note on the representation of steric sea level in models that conserve volume rather than mass, *Journal of Geophysical Research: Oceans (1978–2012)*, *99*(C6), 12,767–12,771.

Griffies, S. M., and R. J. Greatbatch (2012), Physical processes that impact the evolution of global mean sea level in ocean climate models, *Ocean Modelling*, *51*, 37–72.

Griffies, S. M., A. Biastoch, C. Böning, F. Bryan, G. Danabasoglu, E. P. Chassignet, M. H. England, R. Gerdes, H. Haak, R. W. Hallberg, et al. (2009), Coordinated ocean-ice reference experiments (cores), *Ocean Modelling*, *26*(1), 1–46.

Haine, T. W., B. Curry, R. Gerdes, E. Hansen, M. Karcher, C. Lee, B. Rudels, G. Spreen, L. de Steur, K. D. Stewart, et al. (2015), Arctic freshwater export: Status, mechanisms, and prospects, *Global and Planetary Change*, *125*, 13–35.

Häkkinen, S. (1999), A simulation of thermohaline effects of a great salinity anomaly, *Journal of Climate*, *12*(6), 1781–1795.

Häkkinen, S. (2002), Freshening of the labrador sea surface waters in the 1990s: Another great salinity anomaly?, *Geophysical Research Letters*, *29*(24), 85–1.

Häkkinen, S., and A. Proshutinsky (2004), Freshwater content variability in the arctic ocean, *Journal of Geophysical Research: Oceans (1978–2012)*, *109*(C3).

Hansen, J., M. Sato, and R. Ruedy (1997), Radiative forcing and climate response, *Journal of Geophysical Research: Atmospheres*, *102*(D6), 6831–6864.

Helland-Hansen, B., and F. Nansen (1909), The norwegian sea, *Report on Norwegian fishery and marine investigations*, *2*(2), 1–390.

Hibler III, W. (1979), A dynamic thermodynamic sea ice model, *Journal of Physical Oceanography*, *9*(4), 815–846.

Holland, M. M., and C. M. Bitz (2003), Polar amplification of climate change in coupled models, *Climate Dynamics*, *21*(3-4), 221–232.

Holliday, N. P., S. Hughes, S. Bacon, A. Beszczynska-Möller, B. Hansen, A. Lavin, H. Loeng, K. Mork, S. Østerhus, T. Sherwin, et al. (2008), Reversal of the 1960s to 1990s freshening trend in the northeast north atlantic and nordic seas, *Geophysical Research Letters*, *35*(3).

Holloway, G., F. Dupont, E. Golubeva, S. Häkkinen, E. Hunke, M. Jin, M. Karcher, F. Kauker, M. Maltrud, M. Maqueda, et al. (2007), Water properties and circulation in arctic ocean models, *Journal of Geophysical Research: Oceans*, *112*(C4).

Houghton, J. T., L. Meira Filho, B. Callender, N. Harris, A. Kattenberg, and K. Maskell (1996), Climate change 1995: the science of climate change. contribution of working group i to the second assessment of the intergovernmental panel on climate change.

Houssais, M.-N., and C. Herbaut (2011), Atmospheric forcing on the canadian arctic archipelago freshwater outflow and implications for the labrador sea variability, *Journal of Geophysical Research: Oceans (1978–2012)*, *116*(C8).

Hu, A., G. A. Meehl, W. M. Washington, and A. Dai (2004), Response of the atlantic thermohaline circulation to increased atmospheric co2 in a coupled model, *Journal of Climate*, *17*(21), 4267–4279.

Hu, A., G. A. Meehl, W. Han, and J. Yin (2009), Transient response of the moc and climate to potential melting of the greenland ice sheet in the 21st century, *Geophysical Research Letters*, *36*(10).

Hu, A., G. A. Meehl, W. Han, and J. Yin (2011), Effect of the potential melting of the greenland ice sheet on the meridional overturning circulation and global climate in the future, *Deep Sea Research Part II: Topical Studies in Oceanography*, *58*(17), 1914–1926.

Hunke, E., and J. Dukowicz (1997), An elastic-viscous-plastic model for sea ice dynamics, *Journal of Physical Oceanography*, *27*(9), 1849–1867.

Hunke, E. C., and J. K. Dukowicz (2002), The elastic-viscous-plastic sea ice dynamics model in general orthogonal curvilinear coordinates on a sphere-incorporation of metric terms, *Monthly Weather Review*, *130*(7), 1848–1865.

Ikeda, M. (1990), Decadal oscillations of the air-ice-ocean system in the northern hemisphere, *Atmosphere-Ocean*, *28*(1), 106–139.

Ikeda, M., J. Johannessen, K. Lygre, and S. Sandven (1989), A process study of mesoscale meanders and eddies in the norwegian coastal current, *Journal of Physical Oceanography*, *19*(1), 20–35.

Ilicak, M., Q. Wang, R. Gerdes, H. Drange, Y. Aksenov, D. A. Bailey, M. Bentsen, A. Biastoch, A. Bozec, C. Böning, et al. (in press), An assessment of the arctic ocean in a suite of interannual core-ii simulations. part iii: Hydrohraphy and fluxes, *Ocean Modelling*.

Ingvaldsen, R. B., L. Asplin, and H. Loeng (2004), The seasonal cycle in the atlantic transport to the barents sea during the years 1997–2001, *Continental Shelf Research*, *24*(9), 1015–1032.

Inoue, J., M. E. Hori, and K. Takaya (2012), The role of barents sea ice in the wintertime cyclone track and emergence of a warm-arctic cold-siberian anomaly, *Journal of Climate*, *25*(7), 2561–2568.

Ivanov, V. V., V. A. Alexeev, I. Repina, N. V. Koldunov, and A. Smirnov (2012), Tracing atlantic water signature in the arctic sea ice cover east of svalbard, *Advances in Meteorology*, *2012*.

Jayne, S. R., and J. Marotzke (2001), The dynamics of ocean heat transport variability, *Reviews of Geophysics*, *39*(3), 385–411.

Jungclaus, J. H., H. Haak, M. Latif, and U. Mikolajewicz (2005), Arctic-north atlantic interactions and multidecadal variability of the meridional overturning circulation, *Journal of climate*, *18*(19), 4013–4031.

Jungclaus, J. H., H. Haak, M. Esch, E. Roeckner, and J. Marotzke (2006), Will greenland melting halt the thermohaline circulation?, *Geophysical Research Letters*, *33*(17).

Karcher, M., F. Kauker, R. Gerdes, E. Hunke, and J. Zhang (2007), On the dynamics of atlantic water circulation in the arctic ocean, *Journal of Geophysical Research: Oceans*, *112*(C4).

Köberle, C., and R. Gerdes (2003), Mechanisms determining the variability of arctic sea ice conditions and export, *Journal of Climate*, *16*(17), 2843–2858.

Köberle, C., and R. Gerdes (2007), Simulated variability of the arctic ocean freshwater balance 1948-2001, *Journal of physical oceanography*, *37*(6), 1628–1644.

Koenigk, T., U. Mikolajewicz, H. Haak, and J. Jungclaus (2007), Arctic freshwater export in the 20th and 21st centuries, *Journal of Geophysical Research: Biogeosciences (2005–2012)*, *112*(G4).

Koenigk, T., U. Mikolajewicz, J. H. Jungclaus, and A. Kroll (2009), Sea ice in the barents sea: seasonal to interannual variability and climate feedbacks in a global coupled model, *Climate dynamics*, *32*(7-8), 1119–1138.

Kopp, R. E., J. X. Mitrovica, S. M. Griffies, J. Yin, C. C. Hay, and R. J. Stouffer (2010), The impact of greenland melt on local sea levels: a partially coupled analysis of dynamic and static equilibrium effects in idealized water-hosing experiments, *Climatic Change*, *103*(3-4), 619–625.

Kuhlbrodt, T., A. Griesel, M. Montoya, A. Levermann, M. Hofmann, and S. Rahmstorf (2007), On the driving processes of the atlantic meridional overturning circulation, *Reviews of Geophysics*, *45*(2).

Kwok, R. (2009), Outflow of arctic ocean sea ice into the greenland and barents seas: 1979-2007, *Journal of Climate*, *22*(9), 2438–2457.

Kwok, R., and D. Rothrock (1999), Variability of fram strait ice flux and north atlantic oscillation, *Journal of Geophysical Research*, *104*(C3), 5177–5189.

Kwok, R., and D. Rothrock (2009), Decline in arctic sea ice thickness from submarine and icesat records: 1958–2008, *Geophysical Research Letters*, *36*(15).

Kwok, R., G. Cunningham, and S. Pang (2004), Fram strait sea ice outflow, *Journal of Geophysical Research: Oceans (1978–2012)*, *109*(C1).

Large, W., and S. Yeager (2009), The global climatology of an interannually varying air–sea flux data set, *Climate Dynamics*, *33*(2-3), 341–364.

Large, W. G., and S. G. Yeager (2004), *Diurnal to decadal global forcing for ocean and sea-ice models: the data sets and flux climatologies*, Citeseer.

Large, W. G., J. C. McWilliams, S. C. Doney, et al. (1994), Oceanic vertical mixing: A review and a model with a nonlocal boundary layer parameterization, *Reviews of Geophysics*, *32*(4), 363–404.

Latif, M., C. Böning, J. Willebrand, A. Biastoch, J. Dengg, N. Keenlyside, U. Schweckendiek, and G. Madec (2006), Is the thermohaline circulation changing?, *Journal of Climate*, *19*(18), 4631–4637.

Laxon, S. W., K. A. Giles, A. L. Ridout, D. J. Wingham, R. Willatt, R. Cullen, R. Kwok, A. Schweiger, J. Zhang, C. Haas, et al. (2013), Cryosat-2 estimates of arctic sea ice thickness and volume, *Geophysical Research Letters*, *40*(4), 732–737.

Lien, V. S., F. B. Vikebø, and Ø. Skagseth (2013), One mechanism contributing to co-variability of the atlantic inflow branches to the arctic, *Nature communications*, *4*, 1488.

Lique, C. (2015), Ocean science: Arctic sea ice heated from below, *Nature Geoscience*, *8*(3), 172–173.

Lique, C., A. M. Treguier, M. Scheinert, and T. Penduff (2009), A model-based study of ice and freshwater transport variability along both sides of greenland, *Climate Dynamics*, *33*(5), 685–705.

Lorbacher, K., S. Marsland, J. Church, S. Griffies, and D. Stammer (2012), Rapid barotropic sea level rise from ice sheet melting, *Journal of Geophysical Research: Oceans (1978–2012)*, *117*(C6).

Lumpkin, R., and K. Speer (2003), Large-scale vertical and horizontal circulation in the north atlantic ocean, *Journal of Physical Oceanography*, *33*(9), 1902–1920.

Lumpkin, R., K. G. Speer, and K. P. Koltermann (2008), Transport across 48 n in the atlantic ocean, *Journal of Physical Oceanography*, *38*(4), 733–752.

Macdonald, A. M., C. Wunsch, et al. (1996), An estimate of global ocean circulation and heat fluxes, *Nature*, *382*(6590), 436–439.

Marnela, M., B. Rudels, M.-N. Houssais, A. Beszczynska-Möller, and P. Eriksson (2013), Recirculation in the fram strait and transports of water in and north of the fram strait derived from ctd data, *Ocean Science*, *9*(3), 499–519.

Marsh, R., D. Desbruyeres, J. Bamber, B. De Cuevas, A. Coward, and Y. Aksenov (2010), Short-term impacts of enhanced greenland freshwater fluxes in an eddy-permitting ocean model, *Ocean Science*, *6*(3), 749–760.

Maslanik, J., S. Drobot, C. Fowler, W. Emery, and R. Barry (2007), On the arctic climate paradox and the continuing role of atmospheric circulation in affecting sea ice conditions, *Geophysical Research Letters*, *34*(3).

Matti, L. (1983), A growth model for black ice, snow ice and snow thickness in subarctic basins, *Nordic Hydrology*, *14*(2), 59–70.

Mignot, J., and C. Frankignoul (2005), The variability of the atlantic meridional overturning circulation, the north atlantic oscillation, and the el ninõ-southern oscillation in the bergen climate model, *Journal of climate*, *18*(13), 2361–2375.

Mork, K. A., and Ø. Skagseth (2010), A quantitative description of the norwegian atlantic current by combining altimetry and hydrography.

Nurser, A., and S. Bacon (2014), The rossby radius in the arctic ocean, *Ocean Science*, *10*(6), 967–975.

Orvik, K. A., and P. Niiler (2002), Major pathways of atlantic water in the northern north atlantic and nordic seas toward arctic, *Geophysical Research Letters*, *29*(19), 2–1.

Orvik, K. A., and Ø. Skagseth (2005), Heat flux variations in the eastern norwegian atlantic current toward the arctic from moored instruments, 1995–2005, *Geophysical Research Letters*, *32*(14).

Outten, S., and I. Esau (2012), A link between arctic sea ice and recent cooling trends over eurasia, *Climatic change*, *110*(3-4), 1069–1075.

Owens, W. B., and P. Lemke (1990), Sensitivity studies with a sea ice-mixed layer-pycnocline model in the weddell sea, *Journal of Geophysical Research: Oceans (1978–2012)*, *95*(C6), 9527–9538.

Pacanowski, R., and S. Philander (1981), Parameterization of vertical mixing in numerical models of tropical oceans, *Journal of Physical Oceanography*, *11*(11), 1443–1451.

Palter, J. B., M. S. Lozier, and K. L. Lavender (2008), How does labrador sea water enter the deep western boundary current?, *Journal of Physical Oceanography*, *38*(5), 968–983.

Parkinson, C. L., and W. M. Washington (1979), A large-scale numerical model of sea ice, *Journal of Geophysical Research: Oceans (1978–2012)*, *84*(C1), 311–337.

Pavlova, O., V. Pavlov, and S. Gerland (2014), The impact of winds and sea surface temperatures on the barents sea ice extent, a statistical approach, *Journal of Marine Systems*, *130*, 248–255.

Petoukhov, V., and V. A. Semenov (2010), A link between reduced barents-kara sea ice and cold winter extremes over northern continents, *Journal of Geophysical Research: Atmospheres (1984–2012)*, *115*(D21).

Polyakov, I. V., L. A. Timokhov, V. A. Alexeev, S. Bacon, I. A. Dmitrenko, L. Fortier, I. E. Frolov, J.-C. Gascard, E. Hansen, V. V. Ivanov, et al. (2010), Arctic ocean warming contributes to reduced polar ice cap, *Journal of Physical Oceanography*, *40*(12), 2743–2756.

Proshutinsky, A., R. Bourke, and F. McLaughlin (2002), The role of the beaufort gyre in arctic climate variability: Seasonal to decadal climate scales, *Geophysical Research Letters*, *29*(23), 15–1.

Proshutinsky, A., R. Krishfield, M.-L. Timmermans, J. Toole, E. Carmack, F. McLaughlin, W. J. Williams, S. Zimmermann, M. Itoh, and K. Shimada (2009), Beaufort gyre freshwater reservoir: State and variability from observations, *Journal of Geophysical Research: Oceans (1978–2012)*, *114*(C1).

Proshutinsky, A., Y. Aksenov, J. C. Kinney, R. Gerdes, E. Golubeva, D. Holland, G. Holloway, A. Jahn, M. Johnson, E. Popova, et al. (2011), Recent advances in arctic ocean studies employing models from the arctic ocean model intercomparison project.

Quadfasel, D., J.-C. Gascard, and K.-P. Koltermann (1987), Large-scale oceanography in fram strait during the 1984 marginal ice zone experiment, *Journal of Geophysical Research: Oceans (1978–2012)*, *92*(C7), 6719–6728.

Rabe, B., U. Schauer, A. Mackensen, M. Karcher, E. Hansen, and A. Beszczynska-Möller (2009), Freshwater components and transports in the fram strait–recent observations and changes since the late 1990s, *Ocean Science*, *5*(3), 219–233.

Rabe, B., P. Dodd, E. Hansen, E. Falck, U. Schauer, A. Mackensen, A. Beszczynska-Möller, G. Kattner, E. Rohling, and K. Cox (2013), Liquid export of arctic freshwater components through the fram strait 1998–2011, *Ocean Science*, *9*(1), 91–109.

Rabe, B., M. Karcher, F. Kauker, U. Schauer, J. M. Toole, R. A. Krishfield, S. Pisarev, T. Kikuchi, and J. Su (2014), Arctic ocean basin liquid freshwater storage trend 1992–2012, *Geophysical Research Letters*, *41*(3), 961–968.

Rackow, T. (2015), An unstructured multi-resolution global climate model: Coupling, mean state and climate variability, Ph.D. thesis, Universität Bremen, Alfred-Wegener-Institut.

Redi, M. H. (1982), Oceanic isopycnal mixing by coordinate rotation, *Journal of Physical Oceanography*, *12*(10), 1154–1158.

Rennermalm, A. K., E. F. Wood, A. J. Weaver, M. Eby, and S. J. Déry (2007), Relative sensitivity of the atlantic meridional overturning circulation to river discharge into hudson bay and the arctic ocean, *Journal of Geophysical Research: Biogeosciences (2005–2012)*, *112*(G4).

Roach, A., K. Aagaard, C. Pease, S. Salo, T. Weingartner, V. Pavlov, and M. Kulakov (1995), Direct measurements of transport and water properties through the bering strait, *Journal of Geophysical Research: Oceans (1978–2012)*, *100*(C9), 18,443–18,457.

Rudels, B., E. P. Jones, U. Schauer, and P. Eriksson (2004), Atlantic sources of the arctic ocean surface and halocline waters, *Polar Res*, *23*(2), 181–208.

Schauer, U., and A. Beszczynska-Möller (2009), Problems with estimation and interpretation of oceanic heat transport–conceptual remarks for the case of fram strait in the arctic ocean, *Ocean Science*, *5*(4), 487–494.

Schauer, U., E. Fahrbach, S. Osterhus, and G. Rohardt (2004), Arctic warming through the fram strait: Oceanic heat transport from 3 years of measurements, *Journal of Geophysical Research: Oceans (1978–2012)*, *109*(C6).

Schauer, U., A. Beszczynska-Möller, W. Walczowski, E. Fahrbach, J. Piechura, and E. Hansen (2008), Variation of measured heat flow through the fram strait between 1997 and 2006, in *Arctic–Subarctic Ocean Fluxes*, pp. 65–85, Springer.

Screen, J. A., and I. Simmonds (2010), The central role of diminishing sea ice in recent arctic temperature amplification, *Nature*, *464*(7293), 1334–1337.

Semtner Jr, A. J. (1976), A model for the thermodynamic growth of sea ice in numerical investigations of climate, *Journal of Physical Oceanography*, *6*(3), 379–389.

Serreze, M., A. Barrett, J. Stroeve, D. Kindig, and M. Holland (2009), The emergence of surface-based arctic amplification, *The Cryosphere*, *3*(1), 11–19.

Serreze, M. C., and J. A. Francis (2006), The arctic amplification debate, *Climatic Change*, *76*(3-4), 241–264.

Serreze, M. C., M. M. Holland, and J. Stroeve (2007), Perspectives on the arctic's shrinking sea-ice cover, *science*, *315*(5818), 1533–1536.

Shaffrey, L., and R. Sutton (2004), The interannual variability of energy transports within and over the atlantic ocean in a coupled climate model, *Journal of climate*, *17*(7), 1433–1448.

Sidorenko, D., Q. Wang, S. Danilov, and J. Schröter (2011), Fesom under coordinated ocean-ice reference experiment forcing, *Ocean Dynamics*, *61*(7), 881–890.

Sidorenko, D., T. Rackow, T. Jung, T. Semmler, D. Barbi, S. Danilov, K. Dethloff, W. Dorn, K. Fieg, H. F. Gößling, et al. (2014), Towards multi-resolution global climate modeling with echam6–fesom. part i: model formulation and mean climate, *Climate Dynamics*, *44*(3-4), 757–780.

Sidorenko, D., T. Rackow, T. Jung, T. Semmler, D. Barbi, S. Danilov, K. Dethloff, W. Dorn, K. Fieg, H. F. Gößling, et al. (2015), Towards multi-resolution global climate modeling with echam6–fesom. part i: model formulation and mean climate, *Climate Dynamics*, *44*(3-4), 757–780.

Simmonds, I., and K. Keay (2009), Extraordinary september arctic sea ice reductions and their relationships with storm behavior over 1979–2008, *Geophysical Research Letters*, *36*(19).

Skagseth, Ø. (2008), Recirculation of atlantic water in the western barents sea, *Geophysical Research Letters*, *35*(11).

Skagseth, Ø., T. Furevik, R. Ingvaldsen, H. Loeng, K. A. Mork, K. A. Orvik, and V. Ozhigin (2008), Volume and heat transports to the arctic ocean via the norwegian and barents seas, in *Arctic–Subarctic Ocean Fluxes*, pp. 45–64, Springer.

Skagseth, Ø., K. F. Drinkwater, and E. Terrile (2011), Wind-and buoyancy-induced transport of the norwegian coastal current in the barents sea, *Journal of Geophysical Research: Oceans (1978–2012)*, *116*(C8).

Slangen, A., C. Katsman, R. Van de Wal, L. Vermeersen, and R. Riva (2012), Towards regional projections of twenty-first century sea-level change based on ipcc sres scenarios, *Climate dynamics*, *38*(5-6), 1191–1209.

Smedsrud, L. H., R. Ingvaldsen, J. E. Ø. Nilsen, and Ø. Skagseth (2010), Heat in the barents sea: Transport, storage, and surface fluxes.

Sorteberg, A., and B. Kvingedal (2006), Atmospheric forcing on the barents sea winter ice extent, *Journal of Climate*, *19*(19), 4772–4784.

Stammer, D. (2008), Response of the global ocean to greenland and antarctic ice melting, *Journal of Geophysical Research: Oceans (1978–2012)*, *113*(C6).

Stammer, D., N. Agarwal, P. Herrmann, A. Köhl, and C. Mechoso (2011), Response of a coupled ocean–atmosphere model to greenland ice melting, *Surveys in geophysics*, *32*(4-5), 621–642.

Steele, M., R. Morley, and W. Ermold (2001), Phc: A global ocean hydrography with a high-quality arctic ocean, *Journal of Climate*, *14*(9), 2079–2087.

Stouffer, R. J., J. Yin, J. Gregory, K. Dixon, M. Spelman, W. Hurlin, A. Weaver, M. Eby, G. Flato, H. Hasumi, et al. (2006), Investigating the causes of the response of the thermohaline circulation to past and future climate changes, *Journal of Climate*, *19*(8), 1365–1387.

Stroeve, J., M. M. Holland, W. Meier, T. Scambos, and M. Serreze (2007), Arctic sea ice decline: Faster than forecast, *Geophysical research letters*, *34*(9).

Stroeve, J., M. Serreze, S. Drobot, S. Gearheard, M. Holland, J. Maslanik, W. Meier, and T. Scambos (2008), Arctic sea ice extent plummets in 2007, *Eos, Transactions American Geophysical Union*, *89*(2), 13–14.

Stroeve, J. C., V. Kattsov, A. Barrett, M. Serreze, T. Pavlova, M. Holland, and W. N. Meier (2012), Trends in arctic sea ice extent from cmip5, cmip3 and observations, *Geophysical Research Letters*, *39*(16).

Swingedouw, D., P. Braconnot, and O. Marti (2006), Sensitivity of the atlantic meridional overturning circulation to the melting from northern glaciers in climate change experiments, *Geophysical research letters*, *33*(7).

Swingedouw, D., P. Braconnot, P. Delécluse, E. Guilyardi, and O. Marti (2007), Quantifying the amoc feedbacks during a 2× co2 stabilization experiment with land-ice melting, *Climate dynamics*, *29*(5), 521–534.

Timmermann, R., H. Hellmer, and A. Beckmann (2002), Simulations of ice-ocean dynamics in the weddell sea 2. interannual variability 1985–1993, *Journal of Geophysical Research: Oceans (1978–2012)*, *107*(C3), 11–1.

Timmermann, R., S. Danilov, J. Schröter, C. Böning, D. Sidorenko, and K. Rollenhagen (2009), Ocean circulation and sea ice distribution in a finite element global sea ice–ocean model, *Ocean Modelling*, *27*(3), 114–129.

Turrell, W. R., B. Hansen, S. Hughes, and S. Østerhus (2003), Hydrographic variability during the decade of the 1990s in the northeast atlantic and southern norwegian sea, in *ICES Marine Science Symposia*, vol. 219, pp. 111–120.

Vinje, T. (1998), On the variation during the past 400 years of the barents sea ice edge position and northern hemisphere temperatures, *WORLD METEOROLOGICAL ORGANIZATION-PUBLICATIONS-WMO TD*, pp. 271–273.

Vinje, T. (2001), Anomalies and trends of sea-ice extent and atmospheric circulation in the nordic seas during the period 1864-1998, *Journal of Climate*, *14*(3), 255–267.

Vinje, T., and Å. S. Kvambekk (1991), Barents sea drift ice characteristics*, *Polar Research*, *10*(1), 59–68.

Wadley, M. R., and G. R. Bigg (2002), Impact of flow through the canadian archipelago and bering strait on the north atlantic and arctic circulation: An ocean modelling study, *Quarterly Journal of the Royal Meteorological Society*, *128*(585), 2187–2203.

Wang, Q., S. Danilov, and J. Schröter (2008), Finite element ocean circulation model based on triangular prismatic elements, with application in studying the effect of topography representation, *Journal of Geophysical Research: Oceans (1978–2012)*, *113*(C5).

Wang, Q., S. Danilov, D. Sidorenko, R. Timmermann, C. Wekerle, X. Wang, T. Jung, and J. Schröter (2014), The finite element sea ice-ocean model (fesom) v. 1.4: formulation of an ocean general circulation model, *Geosci. Model Dev*, *7*, 663–693.

Wang, Q., M. Ilicak, R. Gerdes, H. Drange, Y. Aksenov, D. A. Bailey, M. Bentsen, A. Biastoch, A. Bozec, C. Böning, et al. (2016a), An assessment of the arctic ocean in a suite of interannual core-ii simulations. part i: Sea ice and solid freshwater, *Ocean Modelling*.

Wang, Q., M. Ilicak, R. Gerdes, H. Drange, Y. Aksenov, D. A. Bailey, M. Bentsen, A. Biastoch, A. Bozec, C. Böning, et al. (2016b), An assessment of the arctic ocean in a suite of interannual core-ii simulations. part ii: Liquid freshwater, *Ocean Modelling*.

Wekerle, C. (2013), Dynamics of the canadian arctic archipelago throughflow: A numerical study with a finite element sea ice and ocean model, Ph.D. thesis, Universitaet Bremen, Alfred-Wegener-Institut.

Woodgate, R. A., and K. Aagaard (2005), Revising the bering strait freshwater flux into the arctic ocean, *Geophysical Research Letters*, *32*(2).

Woodgate, R. A., K. Aagaard, and T. J. Weingartner (2006), Interannual changes in the bering strait fluxes of volume, heat and freshwater between 1991 and 2004, *Geophysical Research Letters*, *33*(15).

Woodgate, R. A., T. Weingartner, and R. Lindsay (2010), The 2007 bering strait oceanic heat flux and anomalous arctic sea-ice retreat, *Geophysical Research Letters*, *37*(1).

Woodgate, R. A., T. J. Weingartner, and R. Lindsay (2012), Observed increases in bering strait oceanic fluxes from the pacific to the arctic from 2001 to 2011 and their impacts on the arctic ocean water column, *Geophysical Research Letters*, *39*(24).

Yang, S., and J. H. Christensen (2012), Arctic sea ice reduction and european cold winters in cmip5 climate change experiments, *Geophysical Research Letters*, *39*(20).

Yin, J., M. E. Schlesinger, and R. J. Stouffer (2009), Model projections of rapid sea-level rise on the northeast coast of the united states, *Nature Geoscience*, *2*(4), 262–266.

Zhang, X., A. Sorteberg, J. Zhang, R. Gerdes, and J. C. Comiso (2008), Recent radical shifts of atmospheric circulations and rapid changes in arctic climate system, *Geophysical Research Letters*, *35*(22).

Acknowledgment

First of all, I would like to express my sincere thanks to my supervisor Prof. Dr. Thomas Jung, who accepted me as his PhD student and provided me the opportunity to performance my PhD project in his group. I am very appreciate for his continuous support and helpful expert advice, although I was really in a mess at times. I also would like to thank Prof. Dr. Torsten Kanzow for taking time to review my PhD thesis.

Great thanks to my mentor Dr. Qiang Wang, who provided me invaluable help and guidance throughout my PhD study. He had busy and hard job himself, but he was always patient and attentive, gave me constructive and pertinent advice on my PhD work. His experienced knowledge on numerical modelling and convincing logic on ocean dynamics helped me efficiently precede my PhD study.

I gratefully acknowledge Dr. Sergey Danilov, Dr. Dmitry Sidorenko, Dr. Jens Schroeter and Dr. Martin Losch for their great support and encouragement, they offered me many constructive advice for improving my work.

I am great thankful to Dr. Claudia Wekerle for her inspiring suggestion and fruitful discussion. I would like to thank Marta Anna Kasper, Dr. Tido Semmler, Dr. Vibe Schourup-Kristensen, Dr. Verena Haid, Dr. Svetlana Losa, Dr. Madlen Kimmritz, and other colleagues from the Climate Dynamics group for their kind support to both my work and life in Germany. I also want to express my gratitude to Andrea Bleyer and Stefanie Klebe for their excellent administrative work that helped me a lot for my stay at AWI.

A special thank goes to my master project supervisor Prof. Dr. Peiliang Li, who introduced me to the oceanography and climate research.

I would also like to thank all the Chinese friends in Bremerhaven for their

great accompany, we shared a lot of nice moments together.

I am infinitely grateful to my parents, who always support me most for my whole life. Their long-term unconditional love and support gave me the strength to move forward.

I acknowledge the graduate school POLMAR at AWI for offering useful courses and China Scholarship Council (CSC) for the financial support for my PhD study from Oct. 2010 to Sep. 2014.